

**Development of high-resolution 3D geological subsurface models
based on airborne electromagnetic data:
Case studies from the Cuxhaven tunnel valley and
the Lutter anticline, northern Germany**

Von der Naturwissenschaftlichen Fakultät der
Gottfried Wilhelm Leibniz Universität Hannover

zur Erlangung des Grades
Doktor der Naturwissenschaften (Dr. rer. nat.)

genehmigte Dissertation

von

Dominik Steinmetz, Dipl.-Geow.

2019

Referentin: Prof. Dr. Jutta Winsemann
Korreferent: Prof. Dr. Gerald Gabriel

Tag der Promotion: 16.07.2019

Table of contents

Abstract	7
Zusammenfassung	9
1. Introduction	11
<i>Case study 1: The Cuxhaven tunnel valley</i>	12
<i>Case study 2: The Lutter anticline</i>	13
2. Geological setting of the study areas	15
2.1 The Central European Basin System	15
2.2 Geological setting of the Cuxhaven tunnel valley	17
2.2.1 The Glückstadt Graben.....	17
2.2.2 Palaeogene and Neogene marginal-marine deposits	18
2.2.3 The Pleistocene Glaciations	20
2.3 Geological setting of the Lutter anticline	21
3. Database and Methods	24
3.1 Airborne electromagnetics - acquisition and processing	24
3.1.1 Frequency-domain helicopter-borne electromagnetics	24
3.1.2 Time-domain helicopter-borne electromagnetics.....	28
3.2 Geological depth maps and borehole data	29
3.3 Acquisition and processing of p-wave seismic data	30
3.4 GOCAD models	30
3.4.1 Construction of an initial 3D geological subsurface model based on the interpretation of borehole and seismic data.....	32
<i>Study area of the Cuxhaven tunnel valley</i>	32
<i>Study area of the Lutter anticline</i>	33
3.4.2 Construction of 3D resistivity grids based on AEM data.....	34
<i>Uncertainties of 3D resistivity grid modelling</i>	36
3.4.3 The relationship between lithology and resistivity.....	38
<i>Study area of the Cuxhaven tunnel valley</i>	39
<i>Study area of the Lutter anticline</i>	40

Table of contents

3.4.4	Integration of the 3D resistivity grids into the 3D geological subsurface model	40
	<i>Study area of the Cuxhaven tunnel valley</i>	40
	<i>Study area of the Lutter anticline</i>	41
3.4.5	Adjustment of the 3D geological subsurface model	42
3.4.6	Verification of the 3D geological subsurface models by means of HFEM forward modelling	42
3.4.7	Fracture analysis in the study area of the Lutter anticline	43
	<i>Field data of fracture orientation</i>	43
	<i>Fracture detection by curvature application</i>	44
4.	Results	46
4.1	Case study 1: The Cuxhaven tunnel valley	46
4.1.1	Depositional architecture of the Cuxhaven tunnel valley and its Neogene host sediments, as defined by seismic and borehole data analysis	46
	<i>Neogene marine and marginal marine deposits</i>	46
	<i>Pleistocene and Holocene deposits</i>	49
4.1.2	Integration of the resistivity grid model and the geological subsurface model	53
	<i>Comparison of borehole resistivity logs with model resistivity data</i>	53
4.1.3	Relationship between borehole lithology logs and AEM model resistivities	58
4.1.4	Correlation of the HFEM resistivity model with the geological model	59
	<i>Neogene marine and marginal marine deposits</i>	59
	<i>Pleistocene deposits</i>	60
4.1.5	Correlation of the HTEM resistivity model with the geological model	61
	<i>Neogene marginal-marine deposits</i>	61
	<i>Pleistocene deposits</i>	62
4.1.6	Verification of apparent resistivity values extracted from the 3D subsurface models ...	64
4.2	Case study 2: The Lutter anticline	67
4.2.1	The 3D geological subsurface model	67
4.2.2	Outcrop data and interpretation	71
4.2.3	Directional geometry analysis of the subtle resistivity signature - correlation with outcrop data	76
4.2.4	Geological interpretation	77

Table of contents

5. Discussion	82
<i>Study area of the Cuxhaven tunnel valley</i>	84
<i>Study area of the Lutter anticline</i>	85
6. Conclusions	87
7. References	90
Acknowledgements	114
Curriculum vitae	115
List of publications	117

Abstract

Airborne electromagnetics (AEM) is an efficient technique for geophysical investigations of the shallow subsurface and has successfully been applied in various geological settings to analyse the depositional architecture for groundwater and environmental purposes. However, interpretation of AEM data is often restricted to 1D inversion results imaged on 2D resistivity maps and vertical resistivity sections. The integration of geophysical data based on AEM surveys, with geological data is often missing and consequently this deficiency leads to uncertainties in the interpretation process.

The aim of this thesis is to provide an improved methodology for the geological interpretation of AEM data and the construction of more realistic 3D subsurface models. This is achieved by the development of integrated workflows and 3D modelling approaches in the Paradigm[®] GOCAD software, based on the combination of different geophysical and geological datasets (airborne electromagnetic data (AEM), depth maps from the digital Geotectonic Atlas of Northwestern Germany and the German North Sea, 2D reflection seismic sections and well logs). The results of 1D AEM inversion were geostatistical analysed and interpolated in a 3D resistivity gridding procedure to create continuous 3D resistivity grids of the subsurface. Subsequently, geological interpretations have been performed by combining with, and validating against geological depth maps, borehole and reflection seismic data and high-quality topographic maps.

For the research, two test sites with different geological settings were chosen.

The primary aim of the first study area near Cuxhaven, northwest Germany, was to test the 3D resistivity gridding procedure for unconsolidated rock, where Neogene sediments are incised by a Pleistocene tunnel valley. The 3D resistivity grids clearly allow to distinguish between different lithologies and enabling the detection of major bounding surfaces and architectural elements. The Neogene succession is subdivided by four unconformities and consists of fine-grained shelf to marginal marine deposits. At the end of the Miocene, an incised valley was formed and filled with Pliocene delta deposits, probably indicating a paleo-course of the River Weser. The Middle Pleistocene (Elsterian) tunnel valley is up to 350 m deep, 0.8-2 km wide, and incised into the Neogene succession. The unconsolidated fill of the Late Miocene to Pliocene incised valley probably formed a preferred pathway for the Pleistocene meltwater flows, thus favouring the incision. Based on the 3D AEM resistivity

Abstract

models the tunnel valley fill could be imaged in high detail. It consists of a complex sedimentary succession with alternating fine- and coarse-grained Elsterian meltwater deposits, overlain by glaciolacustrine (Lauenburg Clay Complex) and marine Holsteinian interglacial deposits. The applied approaches and results show a reliable methodology, especially for future investigations of similar geological settings.

The aim of the second case study was to test a method for the predictive mapping of rock types and fracture orientations in sedimentary rocks using a trend analysis of 3D resistivity pattern based on airborne electromagnetic high-resolution data. For areas with limited exposure, the airborne geophysical data approach is an important method for both, regional-scale geological mapping and local structural analysis. The method was tested in the area of the Lutter anticline structure in the northwestern Harz foreland, Germany. The developed 3D resistivity grid of this salt-cored anticline was used to map resistivity trends that are related to lateral and vertical changes in lithology, water content, anticline geometry, and the location of fractures. The 3D resistivity grid clearly allows to distinguish between rocks of Palaeozoic and Mesozoic rocks. Lineation patterns obtained from a curvature trend analysis based on the 3D resistivity grid reflect the orientation of the local fault and fracture systems. The comparison of the resistivity pattern and the trend of fractures and faults, derived from outcrop analyses, shows promising results, which imply that AEM data can allow the detection and visualization of near-surface, brittle, structural elements developed in sedimentary rocks. This opens the door to use AEM as an efficient tool for regional structural mapping.

Keywords: airborne electromagnetics, 3D subsurface modelling, 3D resistivity grid model

Zusammenfassung

Die Aeroelektromagnetik (AEM) ist eine effiziente Methode für geophysikalische Untersuchungen im Bereich des oberflächennahen Untergrundes und wurde erfolgreich in verschiedenen geologischen Räumen getestet, um u. a. die Ablagerungsarchitektur des Untergrundes hinsichtlich grundwasserwirtschaftlicher Fragestellungen zu untersuchen. Jedoch ist die Interpretation der AEM-Daten oftmals auf 1D Inversionsergebnisse begrenzt, die anhand von 2D Widerstandskarten und Profilschnitten dargestellt werden. Die Integration der durch die Aeroelektromagnetik gewonnenen geophysikalischen Daten mit geologischen Daten fehlt oftmals und führt zu Unsicherheiten in der Interpretation.

Das Ziel der vorliegenden Arbeit ist es eine verbesserte Methode für die geologische Interpretation von AEM Daten zur Erstellung von möglichst wirklichkeitsgetreuen 3D Untergrundmodellen bereitzustellen. Die Methodik basiert auf der Entwicklung integrierter Arbeitsabläufe und 3D Modellierungsansätzen mit Hilfe der Modellierungssoftware GOCAD® von Paradigm und beruht auf der Kombination verschiedener geophysikalischer und geologischer Datensätze (Aeroelektromagnetik, Karten des Geotektonischen Atlas 3D, 2D reflektionsseismische Profile und Bohrdaten). Anhand der geostatistischen Analyse und Interpolation bestehender aeroelektromagnetischer 1D Inversionsergebnisse wurden 3D Widerstandsmodelle des Untergrundes erstellt. Diese wurden anschließend durch Integration geologischer Kartenwerke, Bohrdaten, seismischer Profile und hochauflösender topographischer Karten geologisch interpretiert.

Für die Untersuchungen wurden zwei Testgebiete mit unterschiedlichem geologischem Untergrund gewählt.

Das Ziel des ersten Untersuchungsgebietes im Nordwesten Deutschlands, in der Nähe von Cuxhaven, lag darin die Methodik zur Entwicklung der aus Gitterzellen aufgebauten 3D Widerstandsmodelle an Lockersedimenten im Bereich einer in neogene Ablagerungen eingeschnittenen pleistozänen subglazialen Rinne zu testen. Die 3D Widerstandsmodelle ermöglichen eine genaue Unterscheidung der verschiedenen Lithologien und ermöglichen die Abgrenzung sedimentärer Architekturelemente. Die neogene Abfolge besteht aus feinkörnigen marinen Schelf- und Küstenablagerungen und gliedert sich durch vier Diskordanzen. Hinweise auf den früheren Verlauf der Weser gibt es im oberen Miozän in Form einer erosiven Rinnenstruktur, die im Pliozän mit deltaisichen Sedimenten gefüllt wurde. Die im Mittelpleistozän gebildete subglaziale Rinne (Elster-Eiszeit) schneidet sich bis zu

350 m tief in die neogenen Sedimente ein und ist zwischen 0,8 bis 2 km breit. Die mit Lockersedimenten gefüllte spätmiozäne Rinnenstruktur stellte wahrscheinlich einen bevorzugten Fließweg für die pleistozänen subglazialen Schmelzwässer dar und begünstigte das erosive Einschneiden. Mit Hilfe der 3D Widerstandsmodelle konnte die Rinnenfüllung detailliert dargestellt werden. Sie besteht aus einer komplex aufgebauten sedimentären Abfolge alternierender fein- bis grobkörniger elsterzeitlicher Sedimente, die von glazilakustrinen Sedimenten des Lauenburger Ton Komplexes und marinen Sedimenten des Holstein-Interglazials überlagert werden. Die durchgeführten Untersuchungen und Ergebnisse zeigen eine zuverlässige Methode, die für zukünftige Untersuchungen ähnlicher geologischer Räume angewendet werden kann.

Im zweiten Untersuchungsraum ging es um die Erprobung einer Methode zur Bestimmung vorherrschender Gesteinstypen, Störungs- und Kluftsysteme unter Anwendung von Trendanalysen dreidimensionaler Widerstandsmuster, die auf hochauflösenden aeroelektromagnetischen Befliegungsdaten basieren. In Gebieten mit begrenzter Aufschlussanzahl liefern aerogeophysikalische Messungen entscheidende gesteinspezifische Daten zur Interpretation der regionalen und lokalen geologischen Untergrundverhältnisse. Die Methode wurde anhand eines Gebietes in Deutschland im Bereich des Harzvorlandes, dem Lutter Sattel, getestet. Anhand des erstellten dreidimensionalen Widerstandsmodells dieser auf Salztektunik zurückzuführenden Sattelstruktur konnten laterale und vertikale Änderungen in den lithologischen Einheiten, im Wassergehalt und in der Geometrie der Sattelstruktur sowie Störungszonen identifiziert und kartiert werden. Das erstellte dreidimensionale Widerstandsmodell der Sattelstruktur ermöglicht eine Unterscheidung der aufgestellten paläozoischen und mesozoischen Gesteine. Am elektrischen Widerstandsmodell angewendete Kurvenanalysen zeigen Trendmuster, die mit aus Aufschlüssen bekannten Störungs- und Kluftsystemen übereinstimmen. Der Vergleich zwischen Trendmustern des Widerstandsmodells mit den lokalen, in Aufschlüssen gemessenen Störungs- und Kluftsystemen zeigt vielversprechende Ergebnisse, die darauf hinweisen, dass aeroelektromagnetische Daten zur Identifizierung von Störungssystemen oberflächennah anstehender Sedimentgesteine geeignet sind. Demnach bieten aeroelektromagnetische Daten das Potential für eine direkte strukturanalytische Anwendung.

Schlagworte: Aeroelektromagnetik, 3D Untergrundmodellierung, 3D Widerstandsgittermodell

1. Introduction

Airborne electromagnetics (AEM) is an effective technique to investigate the shallow subsurface. It has successfully been applied in various geological settings to analyse the depositional architecture (e.g. Jordan & Siemon, 2002; Huuse et al., 2003; Sandersen & Jørgensen, 2003; Paine & Minty, 2005; Jørgensen & Sandersen, 2006, 2009; Bosch et al., 2009; Steuer et al., 2009; Pryet et al., 2011; Burschil et al., 2012a, b; Klimke et al., 2013; Christensen et al., 2017). AEM data obtained using novel methods of data acquisition and processing are attractive because the resulting electrical resistivity models of the subsurface can be obtained at a lateral resolution unmet by geological data, while covering areas of hundreds of square kilometres. AEM enables a fast geological overview mapping of subsurface structures and allows different lithologies and porewater conditions to be distinguished (Siemon, 2005; de Louw et al., 2011; Burschil et al., 2012a; Persson & Erlström, 2015; Christensen et al., 2017; Paine & Collins, 2017; Delsman et al., 2018; King et al., 2018). Inversion procedures are carried out to create resistivity-depth models (e.g. Siemon et al., 2009a, b; Vignoli et al., 2017; King et al., 2018), which are the basis for resistivity depth sections and maps. Although this technique is a well-established method to improve geological interpretations of the subsurface architectures, there is a substantial need for an efficient and reliable methodology to image the results in 3D (Ullmann et al., 2016).

Progress in imaging the results in 3D was made by converting 1D inversion models into 3D gridded data models (e.g. Lane et al., 2000; Jørgensen et al., 2005; Bosch et al., 2009; Palamara et al., 2010; Jørgensen et al., 2013; Delsman et al., 2018; Ullmann et al., 2016; King et al., 2018). However, this integration gave limited consideration to uncertainties related to the interpolation procedure (e.g. Pryet et al., 2011). To minimise these uncertainties, different approaches were developed: These include an integrated geophysical and geological interpretation, based on AEM surveys, reflection seismic sections, borehole data and logs, which provide the most reliable results and leads to a minimization of interpretational uncertainties (e.g. Gabriel et al., 2003; Jørgensen et al., 2003a; BurVal Working Group, 2009; Jørgensen & Sandersen, 2009; Høyer et al., 2011; Jørgensen et al., 2013; Oldenborger et al., 2016; Christensen et al., 2017; King et al., 2018). However, there is a substantial need to develop methodologies for an integrated interpretation using different geological and geophysical datasets for the shallow subsurface.

1. Introduction

The thesis is based on the AIDA project, which is a part of the joint research program of GEOTECHNOLOGIEN. The project was financed by the German Federal Ministry of Education and Research (BMBF) grant 03G0735. The AIDA project collaborates with the State Authority for Mining, Energy and Geology (LBEG) and the Federal Institute for Geosciences and Natural Resources (BGR), which provide the data and give support. The aim of this thesis is to provide an improved methodology for the interpretation of AEM data and the construction of 3D subsurface models with reduced interpretation uncertainties by integrating AEM with other geophysical and geological datasets. This is achieved by the development of an integrated workflow and 3D modelling approaches in the GOCAD software (Paradigm[®], 2011), based on the integration of the different geophysical and geological datasets (airborne electromagnetic data, depth maps from the Geotectonic Atlas of Northwestern Germany and the German North Sea, 2D reflection seismic sections and well logs). 1D AEM inversion models and 3D resistivity gridding procedure based on geostatistical analyses and interpolation techniques were used to create continuous 3D resistivity grids of the subsurface. Subsequently, geological interpretations have been performed by combining with, and validating using geological depth maps, wells, and reflection seismic data. The two test sites in this thesis have different geological settings and are considered to be representative for different geological systems. The first study area is characterised by Pleistocene tunnel-valley fills incised into Neogene host sediments. Similar geological settings can be found in Europe or North America, where they are of major importance for local and regional drinking-water supply. The second study area of the Lutter anticline structure is characterized by a complex fracture system of faulted Mesozoic rocks. The characterization of fracture systems is an important step in the reservoir analysis for both hydrocarbon plays and geothermal energy systems, because the tectonic fabrics in bedrock form the most important migration pathways for groundwater, oil, and gas.

Case study 1: The Cuxhaven tunnel valley

The aim of the first case study is to provide a methodology to construct a 3D subsurface model with reduced interpretation uncertainties by integrating AEM, borehole and seismic data. The method was applied and tested with datasets 6 km south of Cuxhaven, northwest Germany (Figure 1). The study area is characterised by Neogene sediments that are incised by an Elsterian tunnel valley. Previous studies focused on overview mapping of Neogene and

1. Introduction

Palaeogene marker horizons and Pleistocene tunnel valleys from 2D reflection seismic sections and borehole logs (Gabriel et al., 2003; BurVal Working Group, 2009; Rumpel et al., 2009). Larger conductive structures within the valley fill were identified from inversion results of 1D frequency-domain helicopter-borne electromagnetics (HFEM) and time-domain helicopter-borne electromagnetics (HTEM) (Rumpel et al., 2009; Steuer et al., 2009). Using the previous results and interpretations as well as the new datasets, a detailed analysis of the seismic facies and sedimentary systems was provided in a 3D geological subsurface model that resolves architectural elements in much greater detail. The generated 3D resistivity grids are based on the geostatistical analysis and interpolation of 1D AEM inversion results. The 3D resistivity grids combine the advantage of volumetric computations with the visualisation of wide resistivity ranges and allow the direct comparison and implementation of additional datasets, such as borehole and seismic data, to improve the geological interpretation of the shallow subsurface.

Contents of this chapter have been published with slight, largely editorial adaptation of a peer-reviewed research paper in Netherlands Journal of Geosciences: “Towards an improved geological interpretation of airborne electromagnetic data: a case study from the Cuxhaven tunnel valley and its Neogene host sediments (northwest Germany)” by Steinmetz, D., Winsemann, J., Brandes, C., Siemon, B., Ullmann, A., Wiederhold, H., Meyer, U., published in Netherlands Journal of Geosciences (2015).

Case study 2: The Lutter anticline

The aim of the second case study is to provide a methodology for the predictive mapping of lithology and fracture orientation. In areas with limited outcrop conditions, airborne geophysical datasets are important, both in regional-scale geological mapping and in assessing local geology. The understanding of the tectonic evolution and orientation of natural fault and fracture systems is important, because they have a strong impact on the hydrogeological properties, as they form discontinuities in the rock mass that can affect the vertical and lateral fluid flow (Allwardt et al., 2007; Beaudoin et al., 2011). Therefore, the knowledge about their orientation is most important for the characterization of groundwater and geothermal aquifers (Zhao & Brown, 1992; Hayashi et al., 1999; Beaudoin et al., 2011), hydrocarbon reservoirs (Gohram et al., 1979; Narr, 1991; Hennings et al., 2000; Zahm & Hennings, 2009) and CO₂ sequestration (Lewicki et al. 2006; Lucier et al., 2006).

1. Introduction

Standard geophysical methods, such as reflection seismics, are often not able to detect fracture sets because they are below the seismic resolution and locally restricted. There is a strong demand for methods that can predict (numerical models) or measure (geophysics) the orientation of tectonic fabrics. Tectonic fabrics are systematically related to the orientation of the paleostress field (Engelder & Geiser, 1980; Fischer & Wilkerson, 2000) and provide valuable data about the tectonic evolution of deformed sedimentary basins (Kleinspehn et al., 1989; Delvaux et al., 1997; Saintot & Angelier, 2002).

In the second case study, the 3D resistivity grid approach was tested for mapping of the prevalent rock types and fracture orientations in bedrock of the Lutter anticline in the Harz foreland, Germany. The resistivity model with prevalent information was used to construct a 3D structural model of the Lutter anticline in the shallow subsurface and to study the relationship between airborne electromagnetic normalized derivatives and systematic patterns of fracture trends. Therefore a method for mapping the electromagnetic resistivity texture based on geometry analysis was already tested for seismic interpretation to predict the structural pattern representing local fracturing. The trend in the resistivity pattern matches the orientation fracture sets measured in outcrop. Systematic trends for shallow, near-surface geological features were detected that could be related to fractures. These signatures in airborne electromagnetic data are commonly weak, small-resistivity anomalies. To improve the qualitative interpretation of subtle anomalies, directional trend analysis by curvature application of 3D resistivity data was used. The results were correlated with geological field observations, and an association between both was probably detected. This method seems to be effective to predict or measure the orientation of tectonic fabrics if incorporated with structural geological modelling.

2. Geological setting of the study areas

2.1 The Central European Basin System

The study areas are both located in the Central European Basin System (CEBS; Figure 1). The CEBS is a rift basin that evolved on top of the Variscan foreland basin in the Late Permian (Betz et al., 1987; van Wees et al., 2000).

The initial rift phase in the early Permian times produced a wide continental rift system that is characterized by north-south trending graben structures (Gast & Gundlach, 2006). During the Late Permian, repeated marine transgressions flooded the sub-basins and thick evaporite successions formed (Pharaoh et al., 2010).

Ongoing extensional tectonics during the Middle to Late Triassic led to the formation of NNE-SSW trending graben structures, which follow the orientation of major basement faults. The main extensional phase in the Late Triassic was accompanied by salt tectonics and rim-syncline development (Kockel, 2002, 2003; Grassmann et al., 2005; Maystrenko et al., 2005a). During the Late Cretaceous to Early Palaeogene, the area was tectonically reactivated in an inversion phase, which is related to the Africa-Iberia-Europe convergence (Maystrenko et al., 2005a; Kley & Voigt, 2008) and was accompanied by local uplift subsidence and salt tectonics (Baldschuhn et al., 1996, 2001; Kockel, 2002; Grassmann et al., 2005; Maystrenko et al., 2005a; Rasmussen et al., 2010). Pre-existing normal faults were commonly reactivated as reverse faults during the basin inversion (Betz et al., 1987; Lohr et al., 2008).

The CEBS is strongly influenced by movement of Upper Permian salt. During the Late Permian 1500-2500 m thick evaporites of the Zechstein Group were deposited (Ziegler, 1990; Stollhofen et al., 2008; Maystrenko et al., 2013). Salt movement in the CEBS was initially triggered by extensional faulting during the Early Triassic. Subsequently rifting pulses during the Late Triassic initiated the second phase of salt movement. A third phase of salt movement was later caused by the Late Cretaceous to Palaeogene compressional inversion phase (Mohr et al., 2005; Kley et al., 2008; Stollhofen et al., 2008; Brandes et al., 2013; Maystrenko et al., 2013). These salt movements further complicated the structural style of the CEBS by decoupling the rocks of the Palaeozoic from the Mesozoic to Cenozoic cover (Lohr et al., 2008; Maystrenko et al., 2013).

2. Geological setting

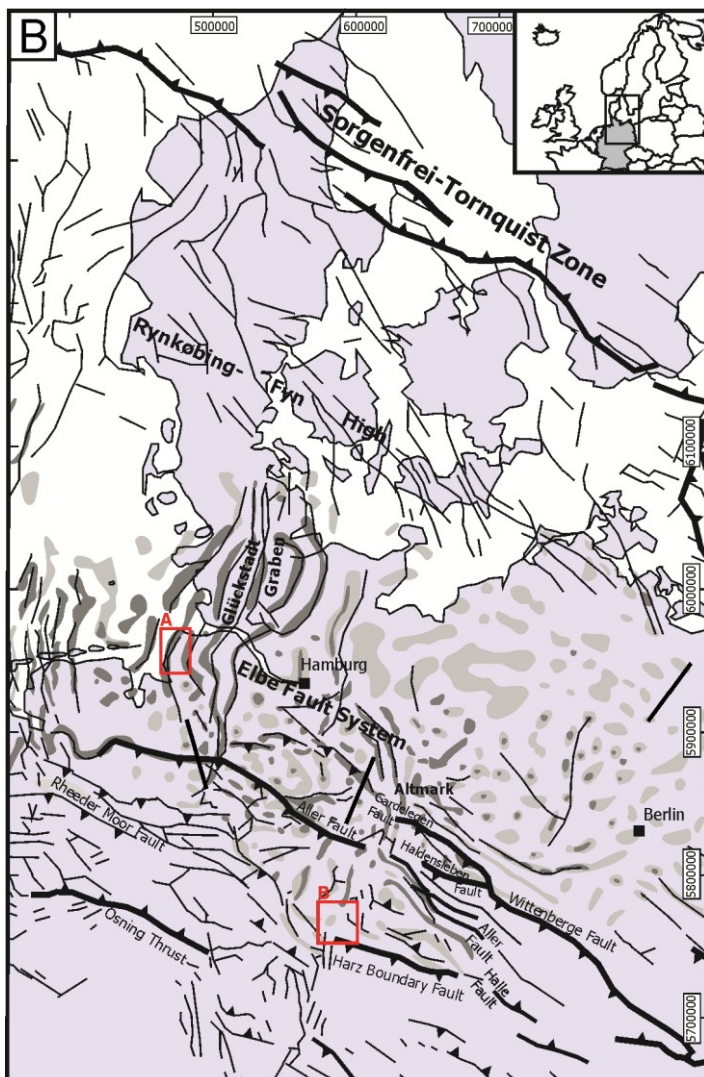
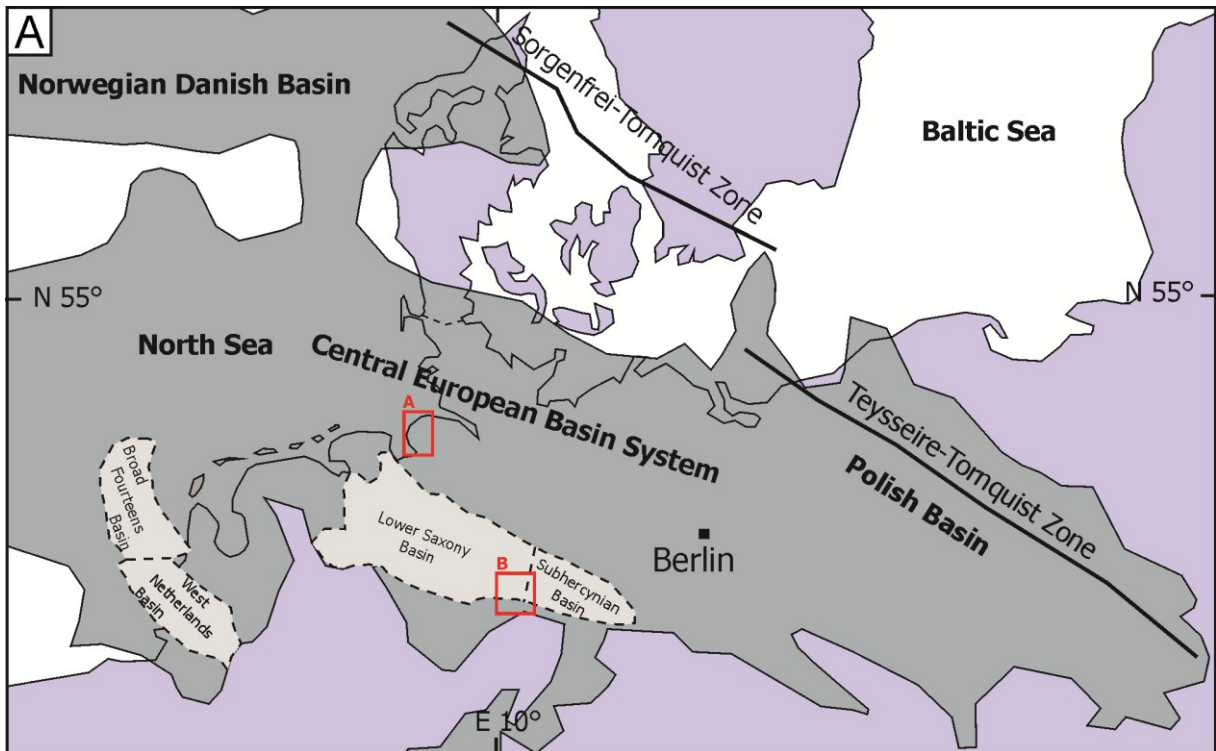


Figure 1: Location map and geological setting. (A) Location of the study areas (A = study area of the Cuxhaven tunnel valley, B = study area of the Lutter anticline) in the Central European Basin System (CEBS) shown in grey (modified after Scheck-Wenderoth & Lamarche, 2005 and Brandes et al., 2013). (B) Faults and salt structures of northern Central Europe. Bold lines are major Late Cretaceous reverse faults. Map based on Baldschuhn (2001), Kley & Voigt (2008) and Brandes et al. (2015).

2. Geological setting

The Cenozoic evolution of the CEBS is characterized by major subsidence and the passive rise of salt diapirs (Lohr et al., 2008). In the North German Basin, the Cenozoic axis is formed by the northwest-southeast trending Central European Subsidence Zone (Stackebrandt, 2009). The orientation of the major horizontal stress in the CEBS is northwest-southeast since the Neogene (Kley et al., 2008; Brandes et al., 2013; Maystrenko et al., 2013).

At the southern margin of the CEBS, faults were reactivated due to stress field changes caused by the decay of the Weichselian ice sheet in the late Pleistocene (Brandes et al., 2012). These stress field changes are probably responsible for ongoing interpolate seismicity in the CEBS (Brandes et al., 2015).

2.2 Geological setting of the Cuxhaven tunnel valley

The study area has the dimensions of 7.5 km by 7.5 km and is located in northwest Germany, between Cuxhaven in the north and Bremerhaven in the south (Figure 2A and B). The study area is located at the southwestern Margin of the Glückstadt Graben, which belongs to the CEBS (Figure 1).

2.2.1 The Glückstadt Graben

The Glückstadt Graben is located (Figure 1B) between the North Sea and the Baltic Sea, and between the Rynkøbing-Fyn High in the north and Elbe Fault System in the south (Maystrenko et al., 2005a). The Glückstadt Graben has a width of 140 to 190 km and formed as a result of Permian to late Middle-Late Triassic (Keuper) extension (Best et al., 1983; Brink et al., 1992; Kockel, 2002). The sedimentary succession of the Glückstadt Graben reflects the major stages in the tectonic development of the CEBS. Coevally with other parts of the CEBS in the Northern German Basin, the Glückstadt Graben was affected by the Late Carboniferous-Early Permian rifting, which is indicated by the presence of volcanics and conglomerate series at the base of the Lower Permian (Gast, 1988; Ziegler, 1990; Benek et al., 1996; Bachmann & Hoffmann, 1997; Bayer et al., 1999). During the Late Permian, repeated marine transgressions flooded the sub-basins and thick evaporite successions formed, which provided the source for the later salt diapirism.

2. Geological setting

Extensional tectonics during the Middle to Late Triassic led to the formation of a broad and deep NNE-SSW trending graben structure, which follows the direction of major older basement faults (Maystrenko et al., 2005a). The Jurassic deposits are characterized by thick marine-organic rich rocks, which form the most prominent oil source rocks in Northern Germany (Grassmann et al., 2005). The deposition of these sediments was mainly concentrated within the salt rim synclines formed by ongoing salt diapirism (Jaritz, 1987). The Jurassic sequence is bounded by an unconformity caused by thermal uplift during Middle Jurassic to Early Cretaceous times (Jaritz, 1980). This unconformity is overlain by marine Lower Cretaceous and Upper Cretaceous sedimentary rocks (Grassmann et al., 2005). During the Late Cretaceous to Early Palaeogene, the area was affected by inversion (Maystrenko et al., 2005a), and led to the reactivation of pre-existing normal faults as reverse faults in the Glückstadt Graben accompanied by rapid subsidence along the northwestern and southeastern margins and ongoing salt movements (Baldschuhn et al., 1996, 2001; Kuster, 2005; Maystrenko et al., 2005a; Grassmann et al., 2005; Rasmussen et al., 2010).

2.2.2 Palaeogene and Neogene marginal-marine deposits

Since Late Oligocene times, sedimentation in the North Sea Basin has been dominated by a large delta system, fed by the large Baltic River System (Huuse & Clausen, 2001; Overeem et al., 2001; Huuse, 2002; Kuster, 2005; Møller et al., 2009; Knox et al., 2010; Anell et al., 2012; Rasmussen & Dybkjær, 2013; Thöle et al., 2014). Initially, the prograding Baltic River System, which drained the Fennoscandian Shield and the Baltic Platform, developed from the northeast, and then rotated clockwise so that the sediment transport direction was from the east and southeast (Sørensen et al., 1997; Michelsen et al., 1998; Huuse et al., 2001; Thöle et al., 2014).

Early Miocene deposits in the study area consist of fine-grained, glauconite-rich, marine, outer shelf deposits bounded at the base by an unconformity (Gramann & Daniels, 1988; Gramann, 1989; Overeem et al., 2001; Kuster, 2005). K-Ar apparent ages of these sediments range from 24.8-22.6 Ma (Odin & Kreuzer, 1988) indicating that the basal unconformity correlates with the marked climatic deterioration and eustatic sea-level fall at the Palaeogene-Neogene transition (Huuse & Clausen, 2001; Zachos et al., 2001; Miller et al., 2005; Rasmussen et al., 2008, 2010; Anell et al., 2012; Thöle et al., 2014).

2. Geological setting

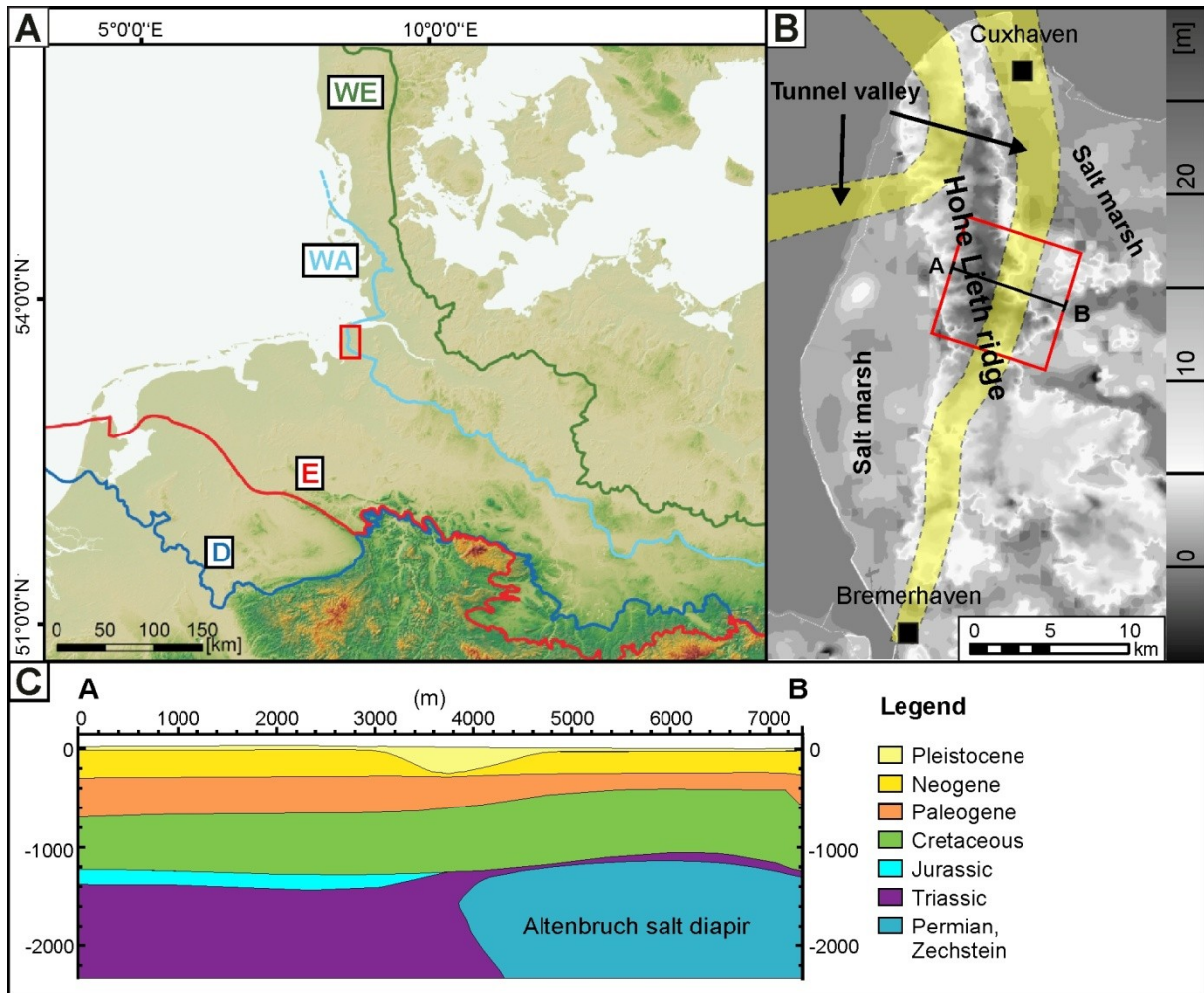


Figure 2: (A) Location of the Cuxhaven study area and maximum extent of the Pleistocene ice sheets: E = Elsterian; D = Saalian Drenthe, WE = Weichselian, WA = Saalian Warthe (modified after Winsemann et al., 2011). (B) Hill-shaded relief model of the study area, showing the outline of the Hohe Lieth ridge with location of Pleistocene tunnel valleys (light yellow). (C) 2D cross-section of the Cuxhaven study area, showing major bounding surfaces.

The lower boundary of the Middle to Late Miocene deposits is the intra Middle Miocene unconformity that can be traced as a strong seismic reflector or as a prominent downlap surface in most parts of the North Sea Basin (Cameron et al., 1993; Michelsen et al., 1995; Huuse & Clausen, 2001; Rasmussen, 2004; Møller et al., 2009; Anell et al., 2012). It coincides with a significant hiatus in the southern, central and northern North Sea Basin (Rundberg & Smalley, 1989; Huuse & Clausen, 2001; Stoker et al., 2005a, b; Eidvin & Rundberg, 2007; Köthe, 2007; Anell et al., 2012; Thöle et al., 2014).

The Middle Miocene hiatus is characterised by sediment starvation and/or condensation, which might have resulted from relative sea-level rise, either eustatic or in combination with tectonic subsidence (Gramann & Kockel, 1988; Cameron et al., 1993; Anell et al., 2012). In the study area, the age of the Middle Miocene unconformity is dated to 13.2-14.8 Ma (Köthe

2. Geological setting

et al., 2008). The overlying fine-grained, glauconite-rich Middle Miocene shelf deposits are characterised by an overall fining-upward trend (Gramann & Daniels, 1988; Gramann, 1989; Overeem et al., 2001; Kuster, 2005).

The Middle Miocene climatic optimum, with a sea-level high stand, was followed by a climatic cooling during the late Middle Miocene and an associated sea-level fall (Haq et al., 1987; Jürgens, 1996; Zachos et al., 2001; Kuster, 2005; Miller et al., 2005). In the study area, Late Miocene deposits consist of shelf and storm-dominated shoreface deposits with an overall coarsening-upward trend (Gramann & Kockel, 1988; Gramann, 1988, 1989; Kuster, 2005) and K-Ar apparent ages ranging from 9.5-11 Ma (Odin & Kreuzer, 1988).

The Pliocene was characterised by several phases of transgression and regression, which lead to the formation of unconformities that can be traced in most areas of the North Sea Basin (Mangerud et al., 1996; Konradi, 2005; Kuhlmann et al., 2004; Kuhlmann & Wong, 2008; Thöle et al., 2014).

2.2.3 The Pleistocene glaciations

During the Pleistocene, large parts of the Central European Basin were affected by the repeated advances of Fennoscandian ice sheets (Ehlers et al., 2011; Böse et al., 2012; Marks, 2011; Lang et al., 2018). The Middle Pleistocene Elsterian and Saalian ice sheets covered most of northern Germany; the Late Pleistocene Weichselian glaciation only affected the eastern parts of Germany (e.g. Caspers et al., 1995; Streif, 2004; Ehlers et al., 2011; Roskosch et al., 2015; Lang et al., 2018).

During the Elsterian glaciation (MIS 12 and 10), deep tunnel valleys were incised into the Neogene and Pleistocene deposits of northern Central Europe (Huuse & Lykke-Andersen, 2000; Lutz et al., 2009; Stackebrandt, 2009; Stewart & Lonergan, 2011; Lang et al., 2012, 2018; van der Vegt et al., 2012; Janszen et al., 2012, 2013, Stewart et al., 2013; Roskosch et al., 2015; Winsemann et al., 2015, 2016). The tunnel valleys were filled with Elsterian meltwater deposits, and till (Stackebrandt, 2009). In the coastal area of northern Germany, the tunnel valleys often comprise late Elsterian glaciolacustrine deposits of the Lauenburg Clay Complex (Kuster & Meyer, 1979, 1995; Linke, 1993; Knudsen, 1988, 1993a, b; Müller & Höfle, 1994; Litt et al., 2007). Holsteinian interglacial deposits (MIS 9) can be found

2. Geological setting

widespread over northern Germany (Litt et al., 2007, 2008). The Saalian complex spans MIS 8 to MIS 6 and is characterized by several pronounced climatic fluctuations (Litt et al., 2008).

The maximum extent of the Saalian ice cover in northern Germany (Figure 2A) was reached during the Older Saalian Drenthe ice advance (cf. Litt et al., 2007; Ehlers et al., 2011; Lang et al., 2018). Deposits include till, glaciofluvial and glaciolacustrine sediments. The youngest Saalian deposits of the Warthe glaciation had a maximum extent and only reaches the study area of Cuxhaven. The subsequent Eemian interglacial occurred during MIS 5e and lacustrine sediments and peats were deposited (Litt et al., 2008). The Weichselian glaciation (MIS 2) did not affect the study areas (Figure 2). The maximum line is placed to the NE of Germany and followed the centre line of Denmark (Hughes et al., 2016). Holocene tidal salt marsh and fluvial deposits, peats and soils characterise the German coast.

2.3 Geological setting of the Lutter anticline

The salt-cored Lutter anticline is located in the Harz foreland, 10 km northwest of Goslar. The cone-shaped anticline has a curved axis that plunges to the NE, is approximately 5 km wide, and is composed of Mesozoic sedimentary rocks. The study area lies between the Lower Saxony and Subhercynian Basin that form parts of the CEBS (cf. Figure 1). The Lutter anticline is formed by salt movement of the Upper Permian Zechstein initiated by extensional tectonics during the Late Triassic (Carlé, 1938; Hosseinidust, 1980) and their compressional reactivation during the Late Cretaceous related to the Africa-Iberia-Europe convergence (Sippel, 2009).

The Lutter anticline is bounded by the Gifhorn Fault Zone (Wolfshagen-Iberg-Lineament) to the east, by the Harz Mountains to the south and the Rhüden Anticline structure to the NW. The bedrock comprises Mesozoic lime-, mud- and sandstones, which show a distinct fault system. The Mesozoic strata are separated by the WNW-ESE trending Harz Boundary Fault from the Palaeozoic rocks of the Harz Mountains (Figure 1 and Figure 3). The Harz Boundary Fault is one of the major fault zones in the CEBS, where the folded Palaeozoic rocks of the Harz Mountains were thrust onto Mesozoic rocks. Seismic data display a steeply southwestward dipping fault (DEKORP-BASIN Research Group, 1999; Krawczyk et al., 1999; Tanner & Krawczyk, 2017). In the main phase of inversion, a displacement of ~7 km

2. Geological setting

occurred within 4 Ma at the Harz Boundary Fault, causing the removal of 2-3 km of Mesozoic overburden (von Eynatten et al., 2008) and the deposition of a ~2.5 km thick syn-tectonic succession in the Subhercynian basin (Voigt et al., 2006).

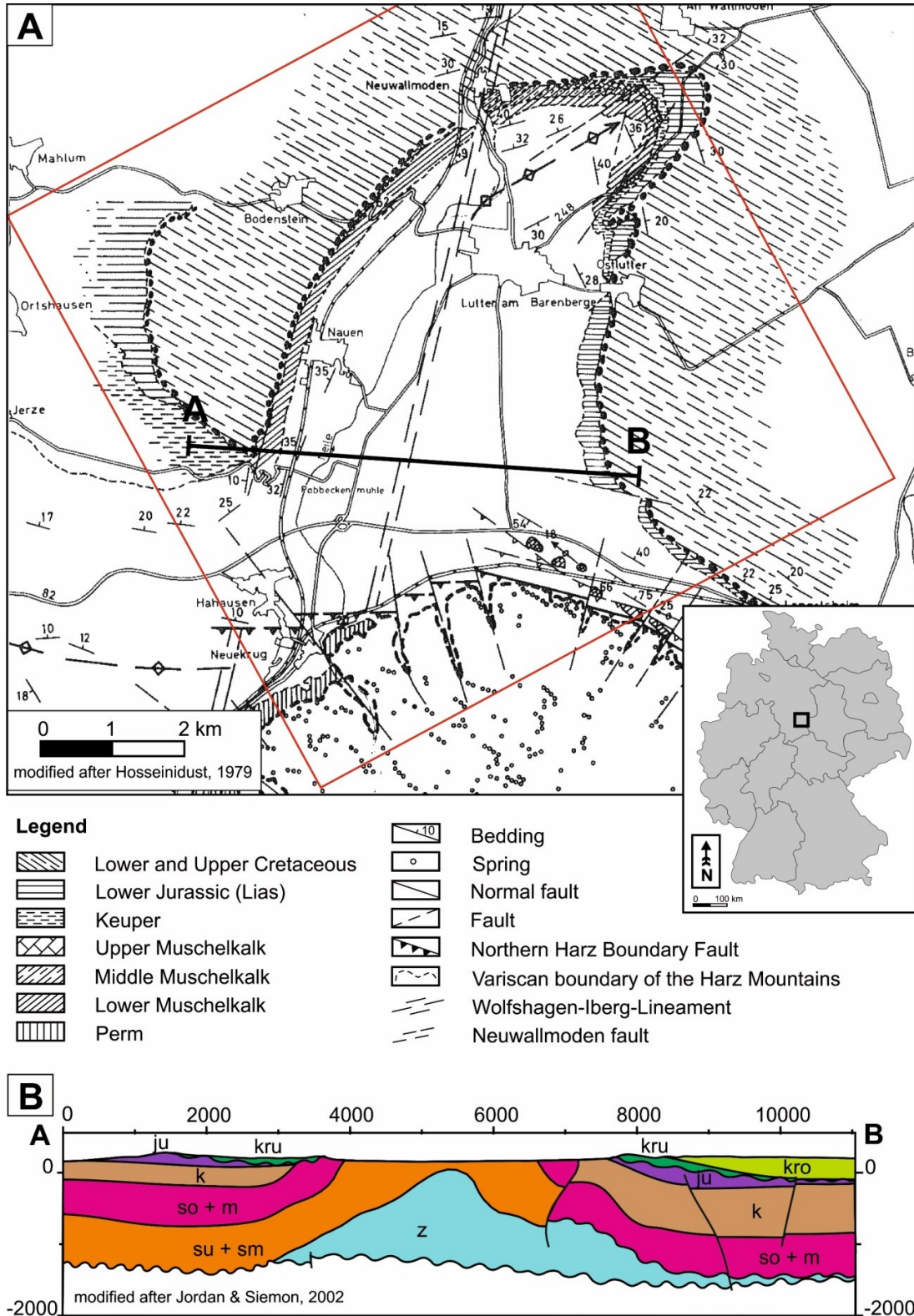


Figure 3: (A) Location of the Lutter anticline. The study area is indicated by a red rectangle (modified after Hosseinidust, 1980). (B) 2D cross-section of the study area, showing major stratigraphic horizons (modified after Jordan & Siemon, 2002).

2. Geological setting

In the early studies of the Lutter anticline, Hark (1956) and Hosseinidust (1980) carried out fairly detailed bedrock mapping and a significant amount of data on fractures was gathered (Figure 4). Fracture orientations in the Lutter anticline are dispersed, but according to Hark (1956) and Hosseinidust (1980), two main orientations of fracture systems are present in the Mesozoic strata of the Lutter anticline: NNE-SSW to NE-SW and WNW-ESE trending fracture systems. NNW-SSE trending fracture systems are subordinate. The local fracture systems are almost oriented parallel to the main fault orientations and can be correlated to tectonic evolution and salt movement (Hark, 1956; Hosseinidust, 1980). Within the Harz Mountains, valleys are developed that correspond to steeply-dipping faults that crosscut the Harz Boundary Fault.

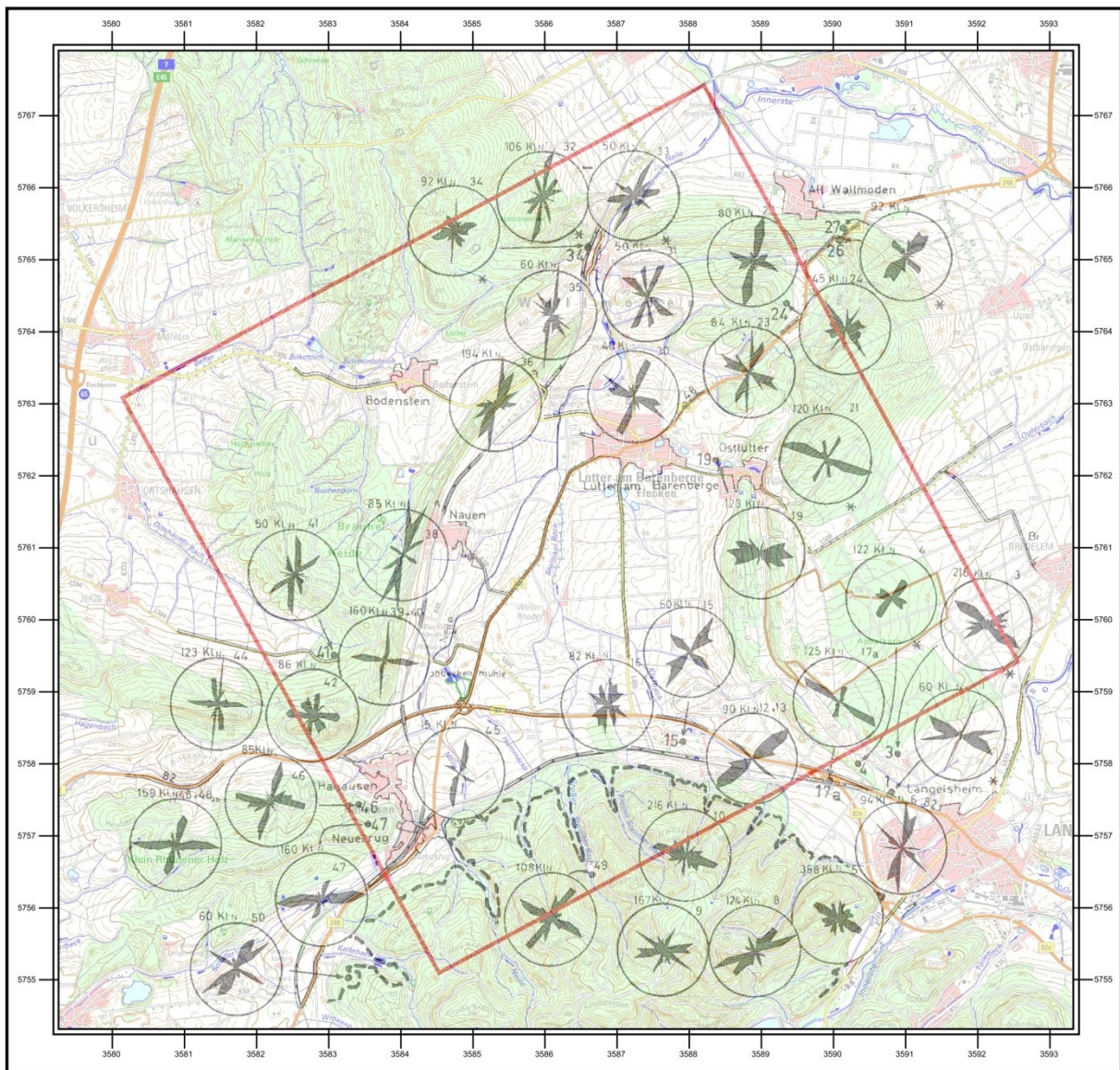


Figure 4: Overview of fracture orientations in the Lutter anticline taken from Hosseinidust (1980). Topographic base map 1:50000 (DTK50), Bundesamt für Kartographie und Geodäsie, Frankfurt am Main.

3. Database and Methods

3.1 Airborne electromagnetics - acquisition and processing

3.1.1 Frequency-domain helicopter-borne electromagnetics

The Federal Institute for Geosciences and Natural Resources (BGR) has covered parts of Germany using systematic, frequency-domain, helicopter-borne, electromagnetic surveys (HFEM, Figure 6), including the coastal region between Bremerhaven and Cuxhaven in northern Lower Saxony (grey lines in Figure 6C), and the Lutter anticline in the northwest part of the Harz Mountains (purple lines in Figure 7; Jordan & Siemon, 2002). Both surveys were conducted in 2000.

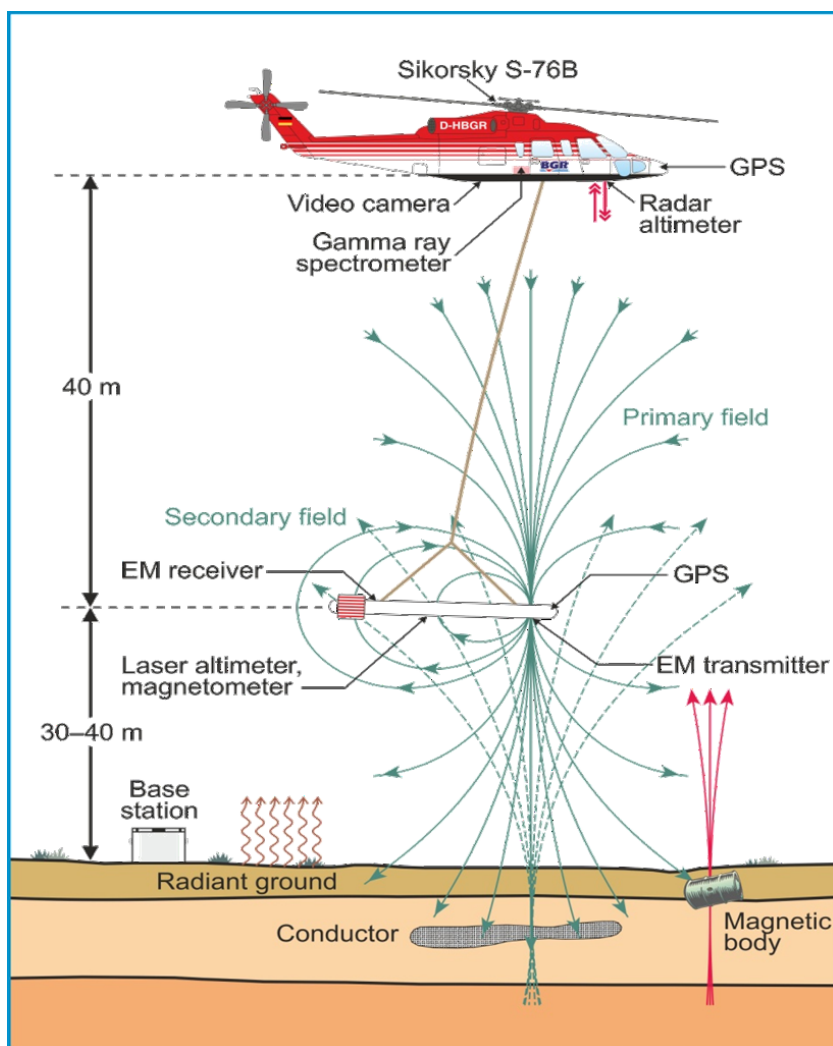


Figure 5: Sketch of the BGR airborne geophysical system. Source: BGR.

3. Database and Methods

In both test sites, the helicopter-borne surveys were flown on parallel-oriented flight lines with an average spacing of 250 m, connected by tie lines running perpendicular to the flight lines with a spacing of 1000 m (Siemon et al., 2002; Jordan & Siemon, 2002). The nominal flight altitude was 80 m and the terrain clearance was 30-40 m (Siemon et al., 2002; Jordan & Siemon, 2002; cf. Figure 5). The distance between consecutive values was about 3-4 m, assuming an average flight velocity of 100-150 km/h during the survey (Jordan & Siemon, 2002; Siemon et al., 2004).

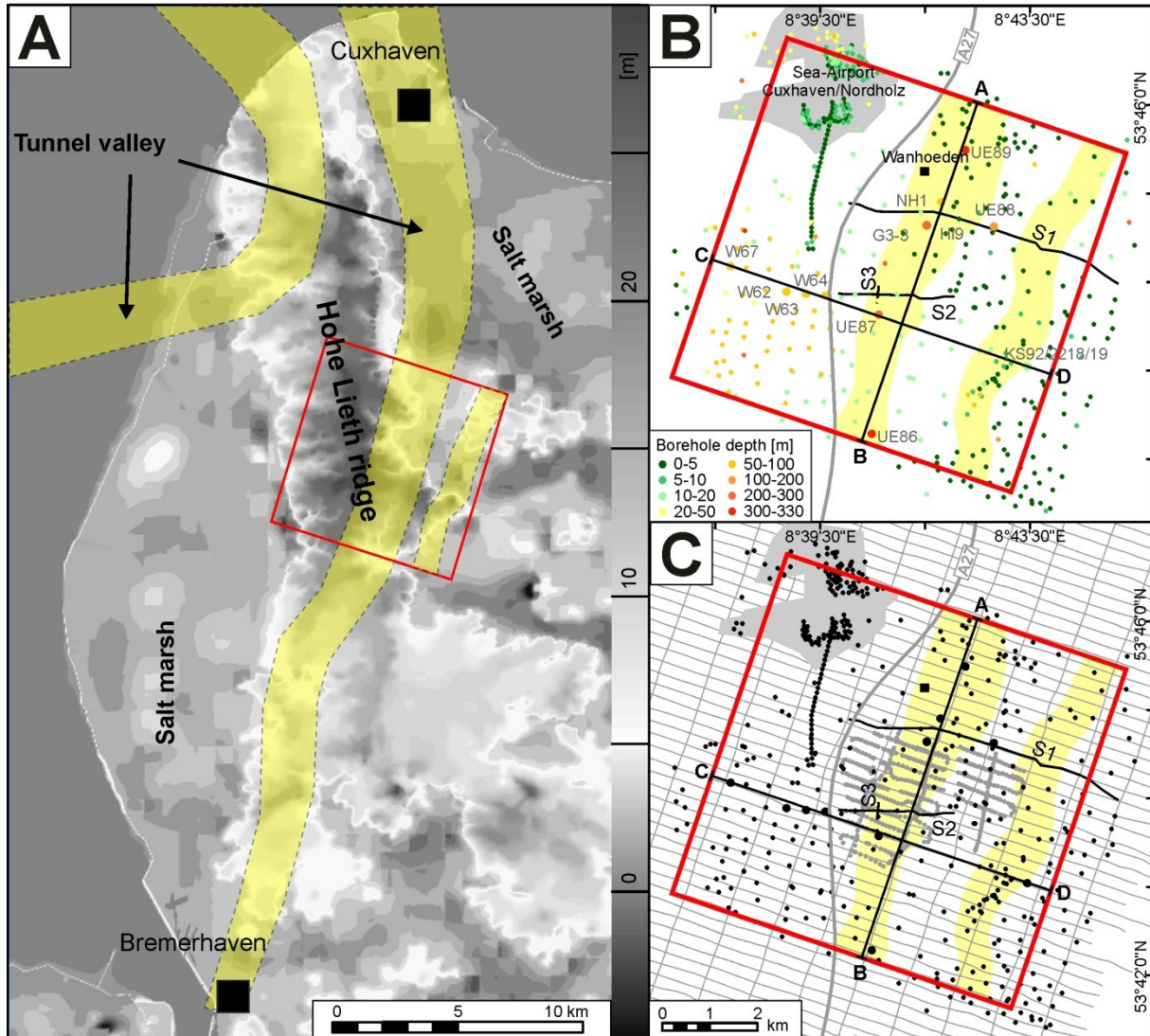


Figure 6: (A) Hill-shaded relief model of the study area, showing the outline of the Hohe Lieth ridge. (B) Close-up view of the study area with location of Pleistocene tunnel valleys (light yellow); location of boreholes (coloured dots); boreholes used in the seismic and cross-sections are indicated by larger dots; seismic sections S1 (Figure 18), S2 and S3 (Figure 19) are displayed as black lines. Cross-section A-B is visualised in Figure 20; C-D is visualised in Figure 21. (C) HFEM surveys are displayed as grey lines; HTEM surveys are displayed as dark grey dots.

3. Database and Methods

The HFEM system used in both surveys was a five-frequency device. The transmitter/receiver coil configuration was horizontal co-planar for all frequencies. The transmitter coils operated at frequencies of 0.4 kHz, 1.8 kHz, 8.6 kHz, 41.3 kHz and 192.6 kHz (Jordan & Siemon, 2002; Siemon et al., 2004). Maximum penetration depth was between 60-160 m, depending on the geology. Sampling rate was 0.1 s and the signal was split into in-phase I and out-of-phase Q components, relative to the transmitter signal. Due to the relatively small system footprint (about 100-150 m), i.e. the lateral extent of the main inductive response beneath the system, the dataset is characterised by a rather high spatial resolution, which decreases with depth (Siemon et al., 2004). This data provides a good basis for geological and geophysical modelling, mapping and evaluation of raw-materials and for environmental monitoring. The measured electromagnetic data provides excellent data for airborne geophysical interpretation and geological mapping (Jordan & Siemon, 2002).

The inversion of HFEM data to resistivity and depth values followed the workflow developed in Sengpiel & Siemon (2000) and Siemon (2001). It depended on an initially unknown subsurface resistivity distribution. Initially the resistivity was calculated based on a half-space model (Fraser, 1978). If the resistivity varies with depth, the uniform half-space model will yield different “apparent resistivity” and “apparent distance” values at each HFEM frequency (Siemon, 2001). The centroid depth is a measure for the penetration of the electromagnetic fields and represents the centre of the half-space. This depth value depends on the individual HFEM frequencies and on the resistivity distribution in the subsurface: the higher the ratio of resistivity and frequency, the greater the centroid depth. From apparent resistivity and centroid depth data pairs, a set of sounding curves was determined at each data point. These apparent resistivity vs. centroid depth-sounding curves are a smooth approximation of the vertical resistivity distribution. They were also used to define individual six-layer starting models at each data point for an iterative Marquardt-Levenberg inversion. The model parameters were modified until a satisfactory fit between the survey data and the calculated field data of the inversion model was achieved (Sengpiel & Siemon, 2000; Siemon et al., 2009a, b). Based on the low number of input parameters available (two per frequency), the number of individual model layers that can be resolved by 1D inversion, is limited. The 1D HFEM inversion results were extracted as a set of data points (reduced to approximately one sounding or 1D model every 7 m along the flight lines). The apparent resistivities are displayed separately at each frequency. Further data handling is described in the respective chapters of the individual case study.

3. Database and Methods

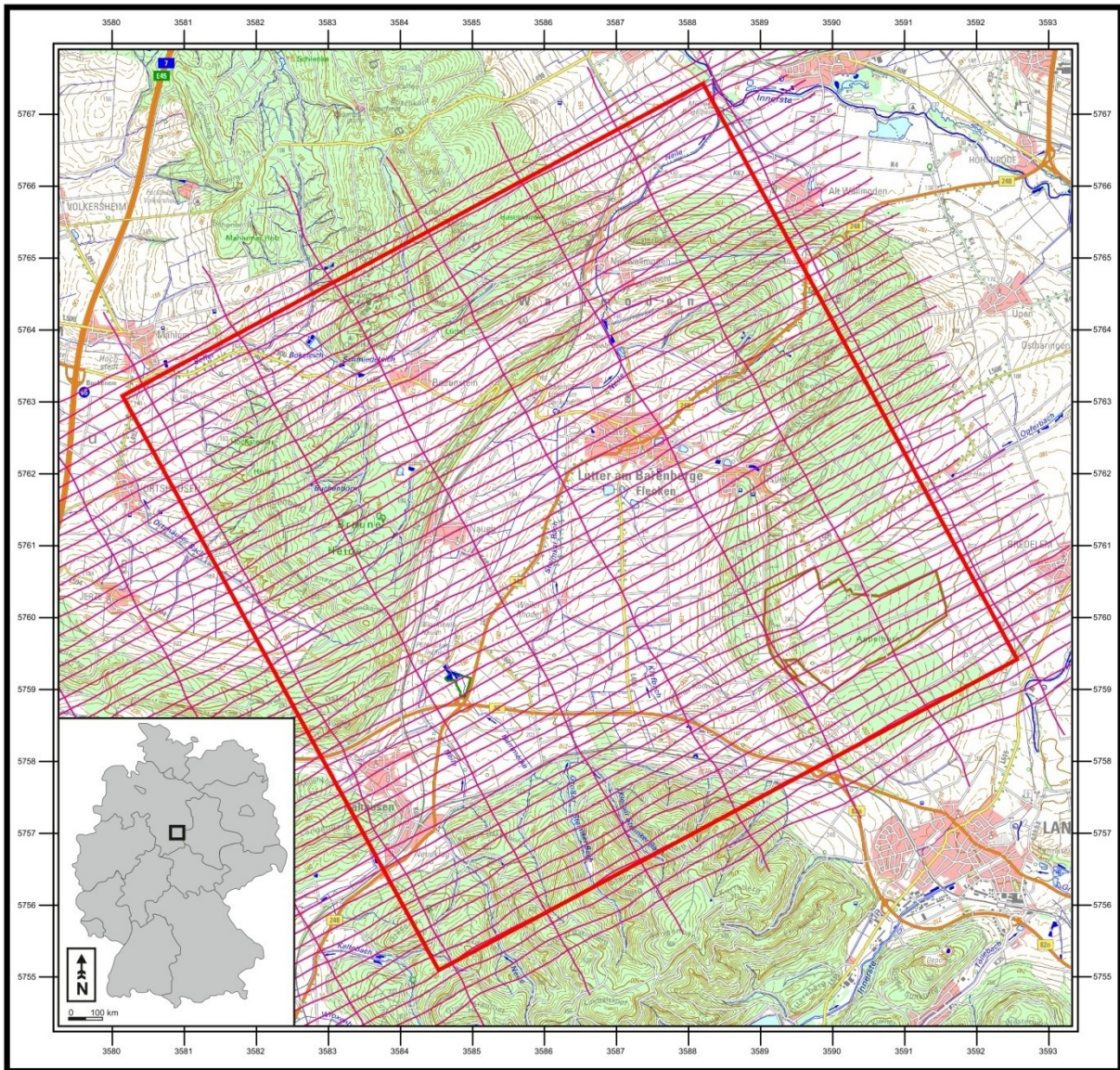


Figure 7: Location of the study area of the Lutter anticline (red rectangle). Flight lines of AEM are coloured in purple. Source: Topographic base map 1:50000 (DTK50), Bundesamt für Kartographie und Geodäsie, Frankfurt am Main.

3.1.2 Time-domain helicopter-borne electromagnetics

Additionally, a helicopter-borne transient electromagnetic (HTEM) survey was conducted by the University of Aarhus (BurVal Working Group, 2009; Rumpel et al., 2009) on behalf of the Leibniz Institute for Applied Geophysics (LIAG, formerly GGA-Institute) in the Cuxhaven study area. The HTEM soundings are restricted to an area of 3.96 km by 2.8 km (grey dots in Figure 6C). The HTEM system operated with a transmitter loop on a six-sided frame (Sørensen & Auken, 2004). In the survey, the distance between consecutive soundings was about 75 m, if one assumes an average flight velocity of 18 km/h during the survey (Figure 6C).

The system is operated with low and high transmitter moments. A low transmitter moment of approximately 9000 Am^2 was generated by a current of 40 A in one measurement cycle. The received voltage data were recorded in a time interval of 17-1400 μs . A current of 40-50 A in four loop turns generated a high moment of approximately 47000 Am^2 . The voltage data of high moment measurements were recorded in a time interval of 150-3000 μs . The acquisition for both, low and high transmitting moments were carried out in cycles of four datasets (320 stacks per dataset for low and 192 stacks per dataset for high moment measurement). Subsequently, the arithmetic mean value of low and high moment datasets were averaged for each to one dataset and subsequently interpreted as one geophysical model. The resolution of the uppermost part of the subsurface is limited by the recording lag time of the HTEM system, which does not start until about 17 μs , and strongly depends on the near-surface conductivity and thus on lithology and the pore-water content (Steuer et al., 2009). This results in near-surface layers being commonly merged into one layer in the model.

The maximum penetration depth is about 250 m and depends on the subsurface resistivity. Because the method cannot resolve thin depositional units ($< 5 \text{ m}$) individual depositional units may be merged into thicker model layers. With increasing depth, the resolution decreases and thus restricts the vertical resolution to approximately 15-20 m in the shallow subsurface, which increases to 20-50 m at 100 m depth. Also, the horizontal resolution decreases with depth. At about 25 m depth, the diameter of the footprint from which data are obtained is about 75-100 m and exceeds 300-400 m at 100 m depth (West & Macnae, 1991; Jørgensen et al., 2005; 2013). Therefore, small-scale spatial variations in geology are less well resolved at deeper levels than the shallower parts (Newman et al., 1986).

The Aarhus Workbench software was used to process the HTEM data (Steuer, 2008; Steuer et al., 2009). The software integrates all steps of the processing workflow from management of the raw data to the final visualisation of the inversion results. The software provides different filtering and averaging tools, including the correction of GPS signal, tilt and altitude values. HTEM data were inverted using a five-layer model with a spatially-constrained inversion (SCI) option of *em1dinv* (Steuer, 2008; Viezzoli et al., 2008; Steuer et al., 2009; HGG, 2011). SCI takes many adjacent datasets into account, which are connected by distant dependent lateral constraints to impose continuity in areas with less data coverage, by supplying information on the expected geological coherency. The inversion results strongly depend on the starting model used and the SCI settings, especially the strength of constraints.

The 1D HTEM inversion results were extracted as a set of models, which are characterised by a limited spatial resolution, due to the large distance between soundings and the relatively large lateral extent of the main inductive response beneath the system.

3.2 Geological depth maps and borehole data

An initial subsurface model was constructed from a commercial SRTM dataset with a resolution of 50 m and published depth maps of the geologic succession (Baldschuhn et al., 1996; Rumpel et al., 2009; Hese, 2012).

Furthermore, in the Cuxhaven area lithology logs of 488 boreholes were used to reconstruct the subsurface architecture of the Cenozoic deposits and to define major geological units. The commercial software package GeODin® (Fugro Consult GmbH, 2012) was used for the data management. Borehole location data were corrected for georeferencing errors.

The interpretation of the tunnel-valley fill is based on five borehole logs that penetrate all five lithological facies units (Figure 6B). A resistivity log was only available for borehole HI9 Wanhoeden, located in the centre of the test site, which penetrates the Cuxhaven tunnel valley (Figure 6B).

3.3 Acquisition and processing of p-wave seismic data

To gain an insight into the large-scale depositional architecture at the Cuxhaven site, three 2D reflection seismic sections were used, acquired by LIAG (Leibniz Institute for Applied Geophysics Hannover) in 2002 and 2005 (black lines in Figure 6B). The 2D reflection seismic sections include a 6 km-long, WNW-ESE oriented seismic line S1 and a 2.4 km-long, W-E trending seismic line S2 that is located 1 km further to the south (Figure 6C). Seismic line S2 intersects with the 0.4 km-long, N-S trending seismic line S3. The survey design and the processing of the sections at seismic line S1 (Wanhoeden), S2 (Midlum 3) and S3 (Midlum 5) are described in Gabriel et al. (2003), Wiederhold et al. (2005b) and Rumpel et al. (2006a, b; 2009).

Data processing was carried out by LIAG with the commercial Landmark software package ProMAX® and followed the workflow for vibroseis data described in Yilmaz (2001). The seismic vibrator operated with a sweep ranging from 50-200 Hz. The survey design led to a maximum target depth of 1600 m with a common-midpoint spacing of 5 m for seismic line S1 and 2.5 m for seismic line S2 and S3. Assuming a velocity of 1600 m/s and a maximum frequency of about 150 Hz, wavelengths of about 10 m are expected and thus the minimum vertical resolution should be in the range of a quarter of a wavelength, but at least about 4 m for the shallow subsurface. Increasing velocity and decreasing frequency with depth leads to a decrease in resolution with depth (wavelength of about 22 m in 1000 m depth). For migration as well as for depth conversion a simple smooth velocity function is used, with a start velocity of 1500 m/s increases to about 2200 m/s at 1000 m depth.

3.4 GOCAD models

To improve the interpretation of the subsurface architecture, a workflow was developed in which the interpretation results of borehole lithology logs, 2D reflection seismic sections and 3D resistivity grids based on 1D AEM inversion results, were integrated (Figure 6, Figure 8 and Figure 9). In order to achieve this, the Paradigm™ GOCAD® software for 3D subsurface modelling was used (Paradigm, 2011).

3. Database and Methods

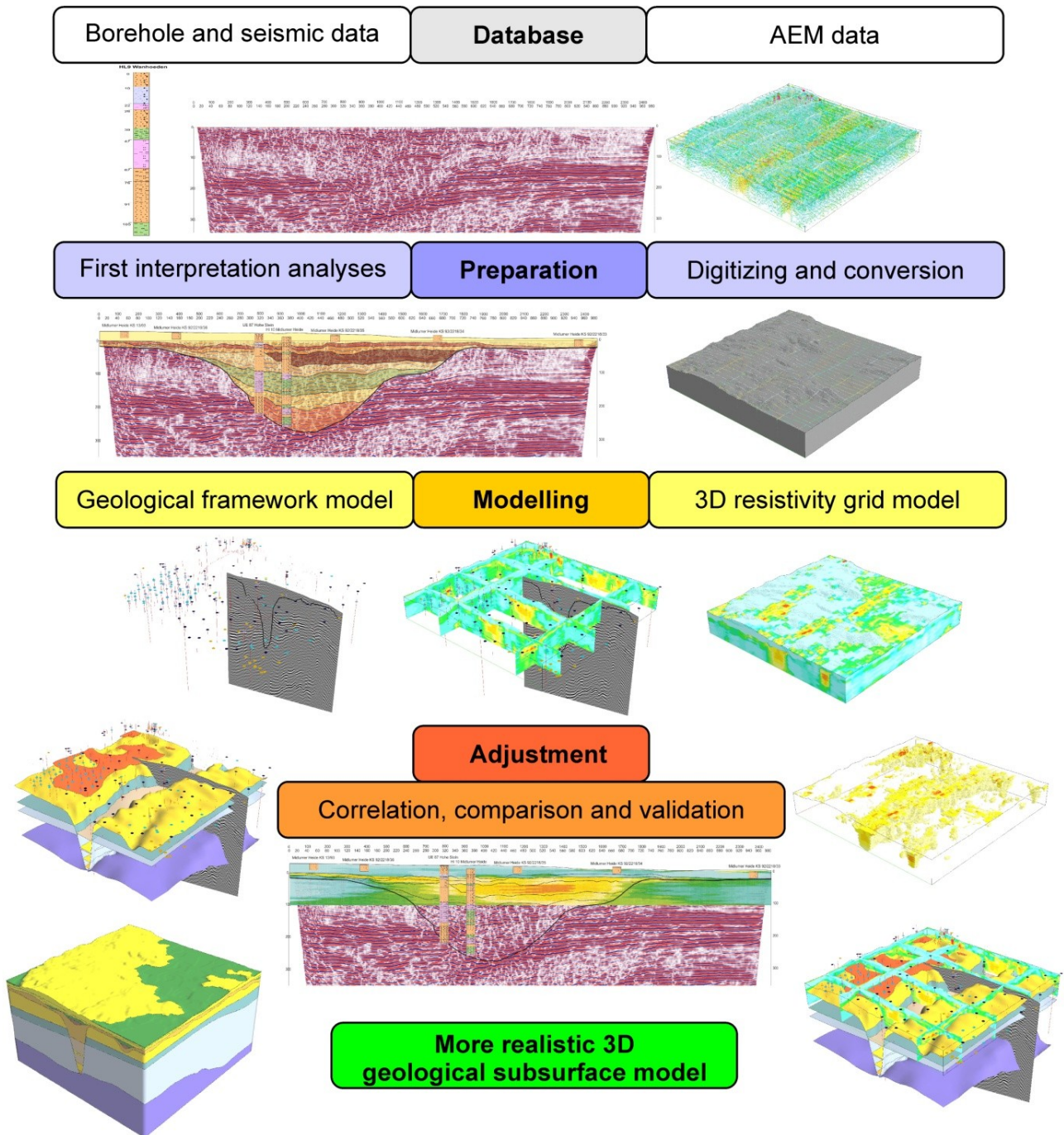


Figure 8: Workflow for the study area of Cuxhaven.

3.4.1 Construction of an initial 3D geological subsurface model based on the interpretation of borehole and seismic data

Study area of the Cuxhaven tunnel valley

For the Cuxhaven study area, the first step was the construction of a basic subsurface model of the tunnel valley and its Neogene host sediments, integrating borehole lithology logs and 2D reflection seismic sections (Figure 9A, Figure 18 to Figure 21).

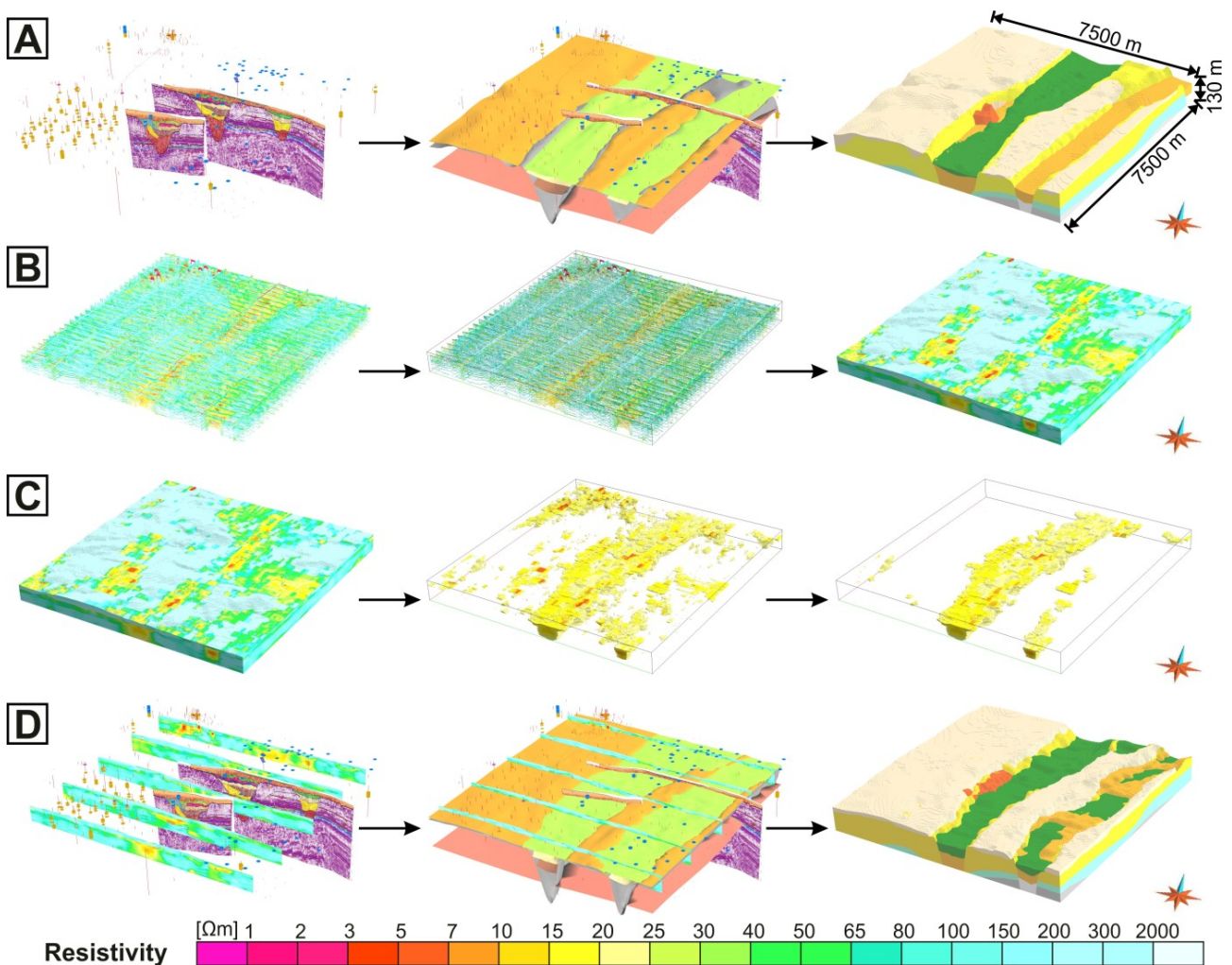


Figure 9: Application for the construction of combined geological/geophysical subsurface models, illustrated by HFEM data. (A) Construction of the 3D geological subsurface model based on borehole and seismic data. (B) Construction of a continuous 3D resistivity voxel grid based on 1D HFEM inversion results. The resistivity data were integrated into a regular-structured grid, analysed by means of geostatistical methods and subsequently interpolated. (C) The selection of specific resistivity ranges provides a first estimate of the large-scale depositional architecture. The clay distribution in the study area is shown, indicated by HFEM resistivity values between 3 and 25 Ωm . (D) Adjustment of the 3D geological subsurface model by integrating information of the 3D resistivity grid.

The scheme of Mitchum et al. (1977) was used for the analysis of seismic sections. Each seismic unit is defined by the external geometry, the internal reflector configuration, and seismic facies parameters, such as amplitude, continuity and density of reflectors (Table 1 and Table 2; Figure 18 and Figure 19). The 2D seismic interpretation results, combined with borehole lithology analysis, defined 15 stratigraphic marker horizons, which represent the tops of each depositional unit (Table 1 and Table 2).

In GOCAD, a discrete modelling approach was applied, that creates triangulated surfaces from points, lines, open and closed curves (Mallet, 2002). With the Discrete Smooth Interpolation (DSI) algorithm the roughness of the triangulated surfaces was minimised (Mallet, 2002). The 3D subsurface model consists of a series of triangulated surfaces that represent the bounding surfaces of the depositional units (Caumon et al., 2009; cf. Table 1 and Table 2; Figure 9).

Study area of the Lutter anticline

For the Lutter test site, the approach based on the construction of an initial 3D geological subsurface model was similar, but solely a Digital Elevation Model (SRTM data with a resolution of 50 m), published depth maps and main faults of the Geotectonic Atlas 3D (Baldschuhn et al., 1996) the Paradigm™ GOCAD® software (Paradigm, 2011), without borehole data, were used.

The resulting 3D model has an extent of 9.1 km by 9.1 km by 100 m depth. It consists of the following stratigraphic horizons: base Upper Permian (Zechstein), base Lower Triassic (Buntsandstein), base Middle Triassic (Muschelkalk), base Upper Triassic (Keuper), base Lower Jurassic (Liassic), base Lower Cretaceous and base Upper Cretaceous (cf. Figure 10 and Figure 26).

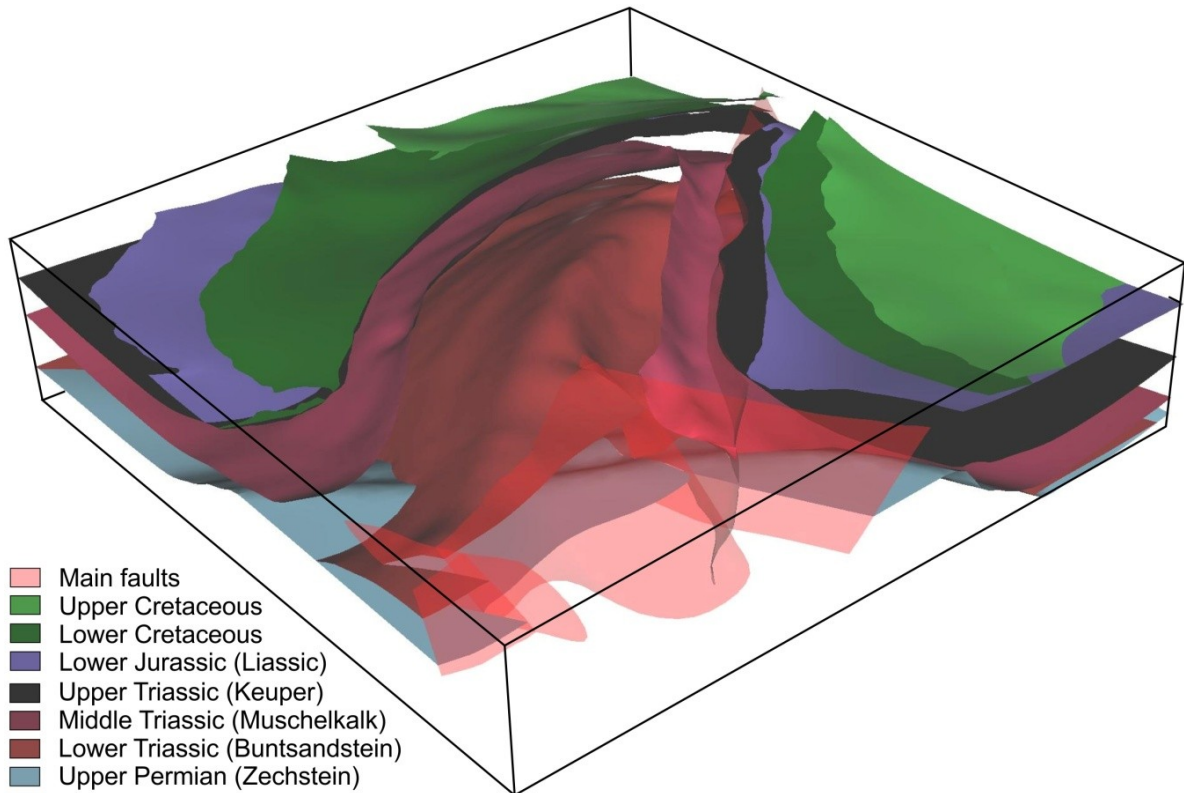


Figure 10: 3D geological subsurface model of the Lutter anticline, based on a digital elevation model (SRTM data with a resolution of 50 m), published depth maps of the Geotectonic Atlas 3D (Baldschuhn et al., 1996).

3.4.2 Construction of 3D resistivity grids based on AEM data

One technique to transform subsurface resistivity data from a set of 1D vertical inversion models into a 3D model is 3D interpolation. The applied 3D interpolation algorithm requires discrete data in all directions, discarding the layered approach used in the inversion, and leads to a smoothing effect between previously-defined layer boundaries of 1D AEM inversion.

In the first step, the 1D AEM inversion models were imported into the GOCAD modelling software (Figure 9B).

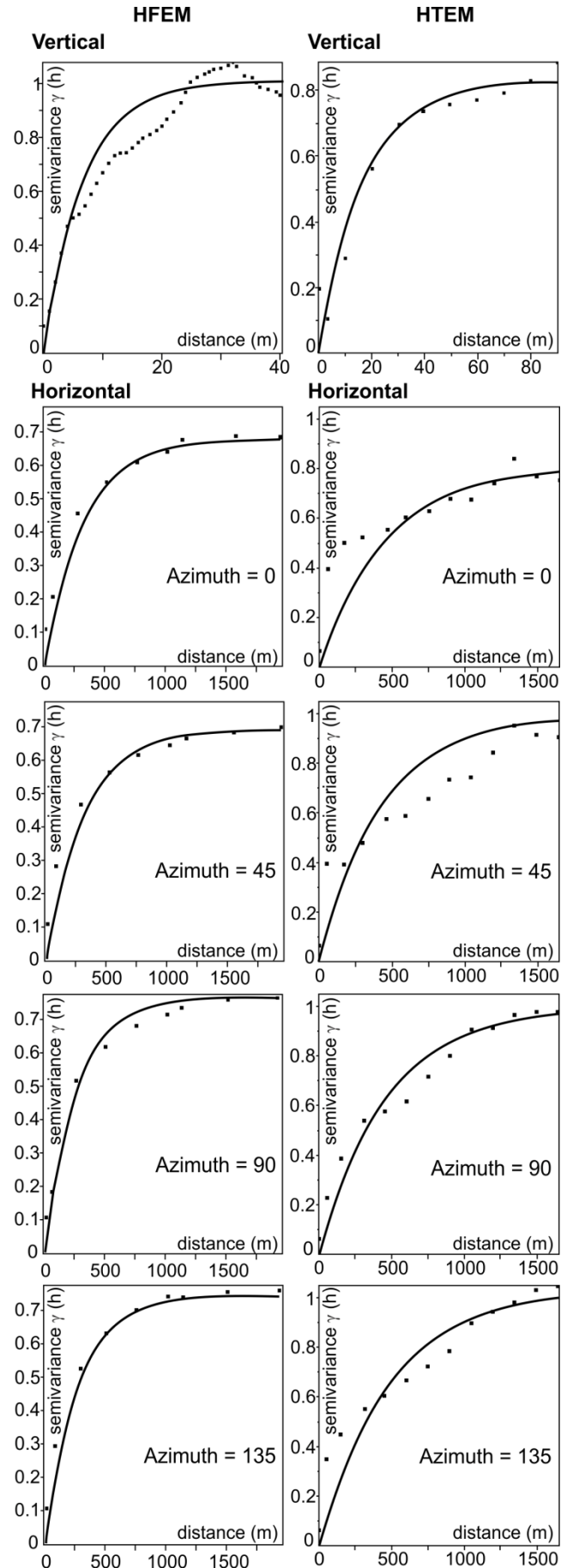
Subsequently, each AEM dataset was transformed into a regular-spaced voxel grid with rectangular hexahedral cells.

The dimensions of the resistivity grid should preserve the maximum resolution of the data, in order to incorporate as much detail as possible. The voxel resolution and the size of the area are important issues because a high amount of voxels (typically millions) may exceed the hardware and software capacities, if it is handled in a real-time 3D environment. To minimise the problems with resolution and performance, a compromise between data resolution and model handling has to be found.

In the Cuxhaven area, large differences in AEM data distribution and penetration depths required the construction of two independent grid models with a different resolution. For the dataset of 1D HFEM inversion results a grid with horizontal and vertical cell sizes of 10 m and 1 m, respectively, was used, which provides a good compromise between data resolution and model handling.

For the dataset of 1D HTEM inversion results, an enlarged grid with horizontal and vertical cell sizes of 20 m and 2.5 m, respectively, provides the best results.

Figure 11: Experimental vertical and horizontal semivariograms derived from the 1D HFEM and HTEM inversion results of the study area. Variography was performed in different directions (azimuths of 0, 45, 90 and 135 degree) with a tolerance of 22.5 degrees. The manually-fitted exponential models are also indicated.



The arithmetic mean was used to transform and estimate the resistivity value of a cell based on each 1D AEM inversion model. The estimation of resistivity at unsampled locations in order to get a continuous 3D resistivity grid model of the subsurface was achieved by the ordinary kriging method (Krige, 1951).

A 1D vertical analysis combined with a 2D horizontal analysis of the 1D AEM inversion models was carried out, since sedimentary successions tend to be more variable in the vertical direction than in the horizontal direction and this often results in zonal anisotropy. Therefore a 1D vertical analysis combined with a 2D horizontal analysis of the 1D AEM inversion models is carried out. Kriging uses semivariogram models to infer the weighting given to each data point and therefore takes both distance and direction into account. Variography was performed in different directions (azimuths of 0, 45, 90 and 135 degrees) with a tolerance of 22.5 degrees and an adjusted bandwidth to survey the resistivity isotropy in each resistivity model (Figure 11). For each AEM dataset, best results in block weighting were obtained by using an exponential function. The analysis of HFEM data results in a vertical range of 25 m and a horizontal major principal axes with an angle of 19 degrees and a range of 1000 m, and a perpendicular minor principal axes with a range of 780 (Figure 11). The analysis of HTEM data results in a vertical range of 50 m and a horizontal major principal axes with an angle of 130 degrees and a range of 1500 m, and a perpendicular minor principal axes with a range of 1300 m (Figure 11). The 3D interpolation results for each voxel over the whole study area in an estimated value for the resistivity.

Uncertainties of 3D resistivity grid modelling

- 1) Data processing of vintage 1D AEM inversion models did not eliminate anthropogenic effects (such as the airport Cuxhaven/Nordholz in the northwest of the study area). Hence, the processed AEM databases contained erroneous data from anthropogenic noise (Siemon et al., 2011).
- 2) 1D AEM inversion models are always simplified realisations of the subsurface resistivity distribution, particularly if only models with few layers are used to explain the AEM data. As AEM resolution decreases with depth, the layer thicknesses generally increase with depth, which corresponds to the probability that several thin layers of various depositional units may be merged to a thicker resistivity layer.

3) Uncertainties may originate from the interpolation method (Pryet et al., 2011). This thesis focuses on uncertainties caused by the kriging interpolation method of the 1D AEM inversion results. A geostatistical uncertainty estimate is provided by the kriging variance $\sigma^2_{\text{KRI}}(x, y, z)$, which depends on the spatial variability of the parameter and the distance to individual data points. This leads to the construction of a 3D grid that contains both resistivity values and their uncertainties (Pryet et al., 2011). Once the model is built, the analysis of uncertainties between data points (i.e. between flight lines) is expressed by the standard deviation σ_{KRI} (Figure 12). The standard deviation can be used to evaluate the credibility of the interpolated data, and to eventually exclude soundings or groups of soundings with high uncertainty and instead emphasise high-quality soundings. A value close to zero indicates high uncertainty and a value close to one indicates low uncertainty of resistivity values. This information can be used to evaluate the relationship between borehole lithology and 3D resistivity data and hence to quantify uncertainties in the depositional architecture.

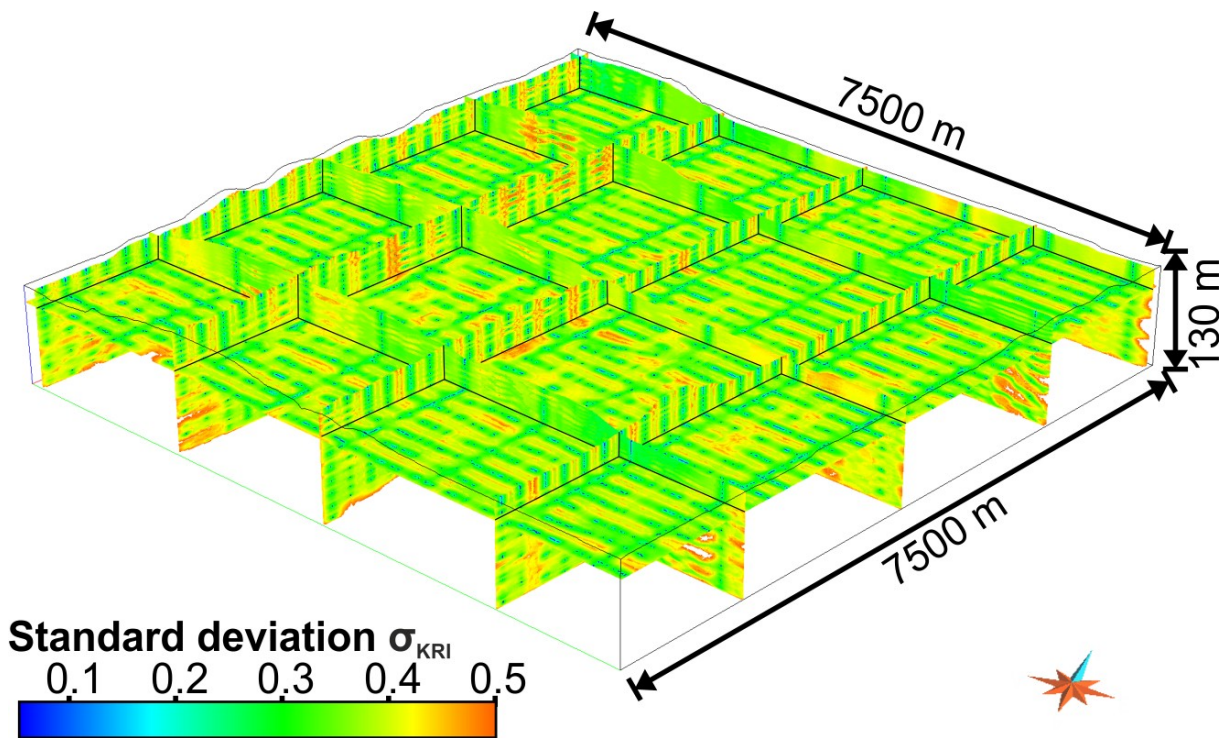


Figure 12: 3D view of kriging uncertainty on log-transformed resistivity for the Cuxhaven test site. The kriging standard deviation σ_{KRI} from the interpolation process of HFEM data is displayed. Low uncertainty traces (dark-blue) indicate the flight lines while the greatest uncertainty is across lines (rather than along lines).

3.4.3 The relationship between lithology and resistivity

Geological (borehole data, field observations) and AEM resistivity information were linked with the aim to use resistivity as a proxy for lithology (see: Bosch et al., 2009; Burschil et al., 2012b; Marker et al., 2016; Christensen et al., 2017).

The measured resistivity in the subsurface is essentially controlled by the movement of charged ions in pore fluids and by conductivity of secondary minerals. The electrical properties of the material are described by conductivity (reciprocal of resistivity). The electrical conductivity describes the ability of a material to conduct an electrical current. This parameter spans several orders of magnitude, with respect to rocks and minerals in the Earth (Figure 13).

Electromagnetic methods have the ability to define geological structures by relating electrical resistivity to the composition of rocks and other processes affecting them (Bedrosian et al., 2016). However, most minerals that form rock are electrical insulators. Although water is a good conductor of electricity, saline groundwater generally contains dissolved compounds that greatly enhance electrical conductivity (Siemon et al., 2015). Groundwater movement is facilitated by interconnected pores and fractures, thus causing hydrothermal alteration of the host rocks.

The resistivity is defined by Ohm's Law, $E = \rho J$; E [V/m] and J [A/m²]. It is defined as the ratio of the potential difference to the current I [A] across a material that has a cross-sectional area of 1 m² and is 1 m long

$$\rho = E/J = \Delta V / I$$

where ρ is the resistivity, which depends on the material and is measured in Ωm . The reciprocal of resistivity is conductivity ($1/\rho = \sigma$) [Siemens/m] or [S/m].

Figure 13 is a summary of the resistivity (conductivity) of various rock-forming materials.

The main parameters that control the electrical resistivity are the degree of water or brine saturation, temperature, porosity as well as electrical resistivity of the fluid filling the pore space (Palacky, 1987). When working with fractured zones, porosity and permeability are controlled by the fractures. The porosity level tends to decrease with depth, which then reduces the effect of the pore fluid conditions. Consequently, resistivity increases, countering to some extent the effect of higher salinity that is commonly inferred to lie in the deeper parts

within the systems. In the pores, the salinity is high; thus it controls the electrical resistivity (Palacky, 1987).

According to Archie (1942), resistivity for clay-free sediments is inversely proportional to the pore-water ion content. If the specific pore-water ion content is known throughout the different geological units and structures, estimates in lithology variations related to the clay content and type can be obtained. Because saline groundwater is absent in both study areas, resistivity changes are almost related to changes in lithology.

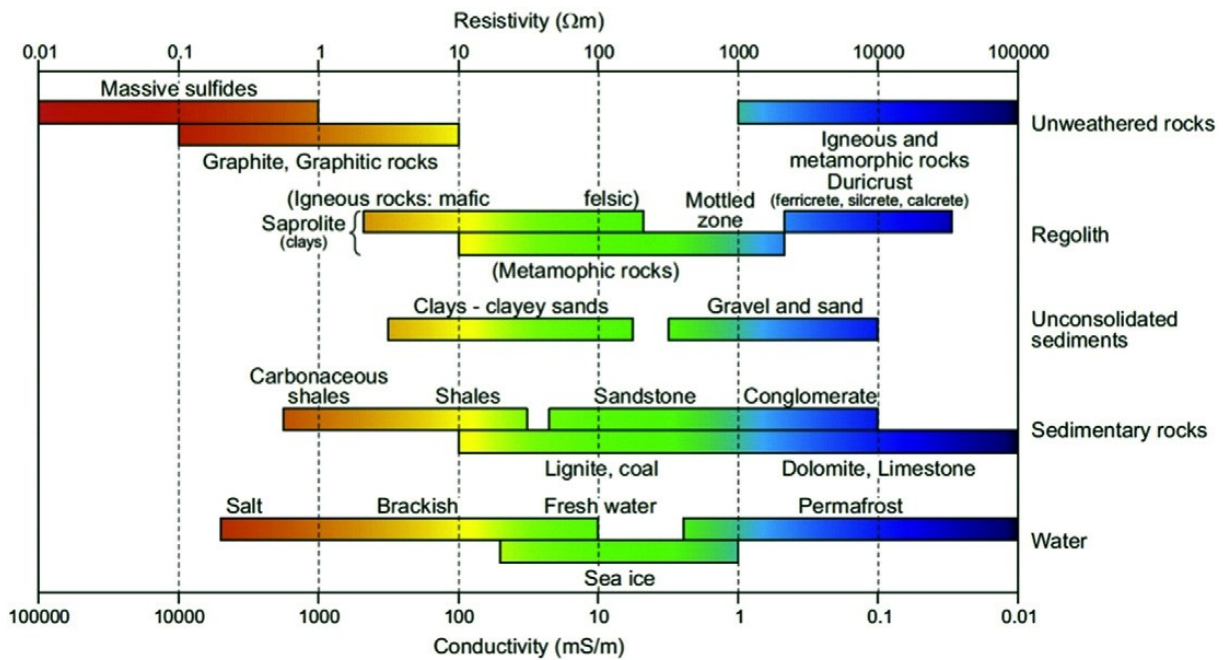


Figure 13: Conductivity-resistivity values of various geological materials, spanning massive sulphides to graphite at high conductivities, to limestone, duricrust and silcrete with low conductivities (modified after Palacky, 1987). Clay and sand differ in conductivity by up to three orders of magnitude, similar to fresh versus saline water, respectively.

Study area of the Cuxhaven tunnel valley

Sediment descriptions from 487 borehole logs and the resistivity log from borehole H19 were used to combine both parameters in the Cuxhaven study area. The lithologies were divided into seven grain-size classes based on the borehole descriptions. In accordance with data resolution, the representative lithology in each borehole was determined and the corresponding interpolated resistivity at this location was extracted from the 3D resistivity grids based on the two different AEM datasets. That the lithology logs within the study area have varying resolution that range from one centimetre to one metre, depending on the drilling method and data collection used. This may lead to a discrepancy between the

lithology log and the vertical resolution of the 3D AEM resistivity grids, which results in insufficient resistivity-grain size relationships. To reduce the uncertainty between the lithology logs and resistivity grid, all logs were analysed and mean and median resistivity values were calculated for each class that allowed derivation of grain size from resistivity (Figure 23). Grouping the data into resistivity classes and counting the number of occurrences of each lithology, resulted in the proportion of occurrences of each grain-size class per resistivity group (Figure 23). As high resistivity values in the study area often represent dry sediments, the focus is put on resistivity values up to 250 Ωm .

Study area of the Lutter anticline

A similar approach for the regional determination of Palaeozoic and Mesozoic rock types and their architecture, and resistivity gradients and their orientation followed in the Lutter study area. Mudstones and shales typically have low resistivities, while lime- and sandstones typically exhibit high resistivities (Keller, 1966; Palacky, 1987). A lithological log of the Lutter anticline, correlated to resistivity, is displayed in Figure 25. Displacements in the resistivity pattern are interpreted to indicate major faults.

3.4.4 Integration of the 3D resistivity grids into the 3D geological subsurface model

Study area of the Cuxhaven tunnel valley

In order to test the match between the 3D resistivity grid models (based on 1D inversion results of AEM data) and the 3D geological subsurface model (based on borehole, seismic and depth map data), both were integrated into GOCAD (cf. workflow displayed in Figure 8). In order to verify the validity and accuracy of data and their integration in the Cuxhaven study area, a mutual comparison between seismic reflector pattern and their corresponding resistivities obtained from the 3D AEM resistivity grids in GOCAD followed (Figure 18C, D and Figure 19C, D). Grain-size classes defined from borehole logs were related to resistivity values which were derived from the 3D AEM resistivity grid models (Figure 23).

Study area of the Lutter anticline

In the study area of the Lutter anticline, the 3D geological subsurface model based on the Digital Elevation Model (SRTM data with a resolution of 50 m), published depth maps and main faults of the Geotectonic Atlas 3D (Baldschuhn et al., 1996) and the 3D resistivity grid (based on the interpolated 1D inversion results of AEM data) were integrated into GOCAD (Figure 14).

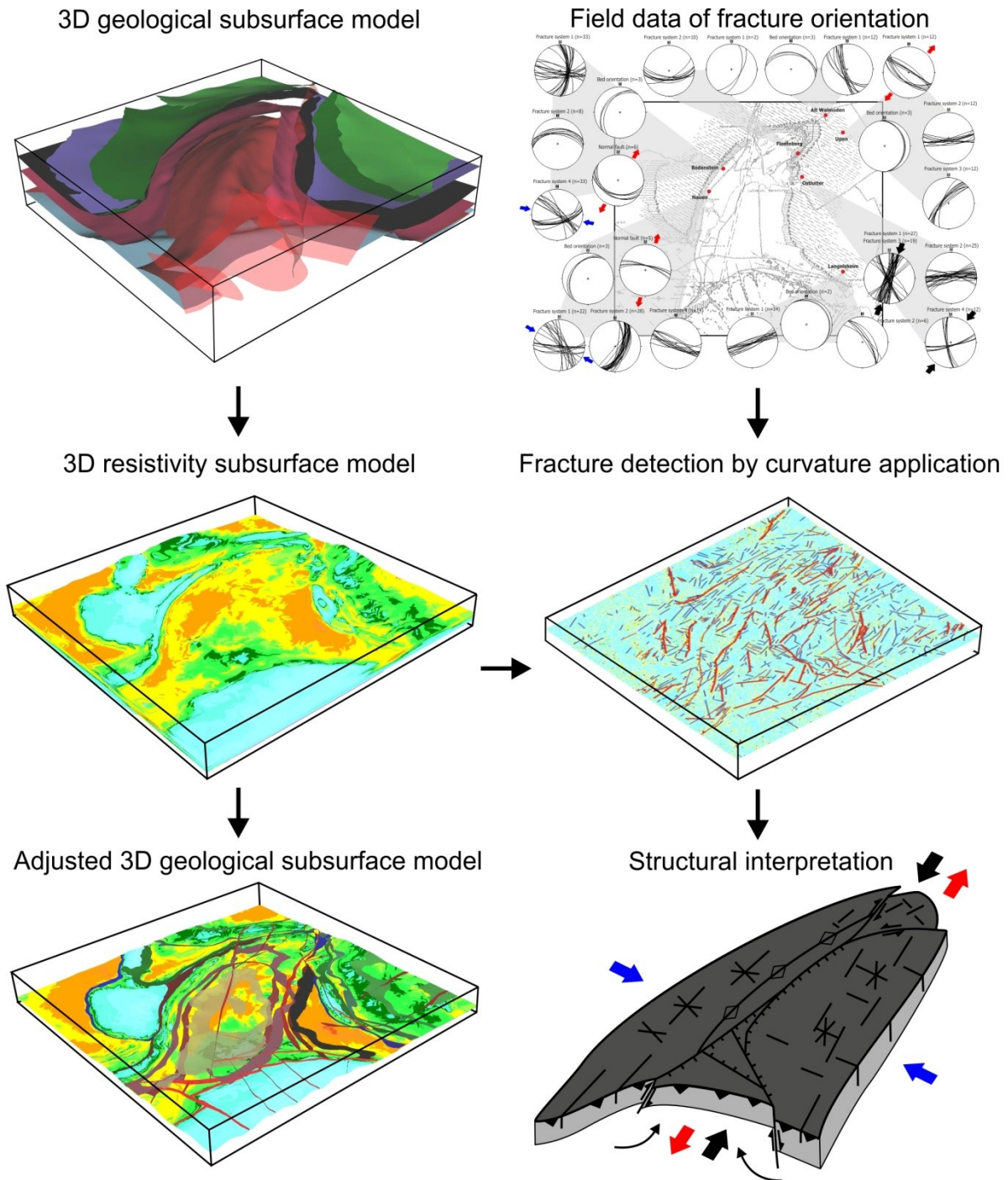


Figure 14: Workflow for the study area of the Lutter anticline.

3.4.5 Adjustment of the 3D geological subsurface model

The GOCAD modelling software has various possibilities to visualise properties such as resistivity values of the 3D grid models to facilitate use and interpretation of data. This includes changes in the colour scale, the selection of given resistivity ranges and voxel volumes. The selection of specific resistivity ranges in the 3D resistivity grid, in particular, provides first rough estimate of the three-dimensional geological architecture (Figure 9D).

This study proposes a method for 3D geological modelling of AEM data in which the limitations are jointly considered together. The relationship between lithology and resistivity and its corresponding resistivity values was used to adjust the bounding surfaces of the geological framework model. After adjusting the geological framework, the updated 3D geological subsurface models were combined with the 3D HFEM voxel grid. Voxel grids can hold an unlimited number of attributes and different parameters can be added to the grid structure as attributes such as lithology, facies or model uncertainty. The high resolution of the regular voxel model allows the maintenance of the subsurface structure. The result is a more reliable reconstruction of the shallow subsurface architecture (Figure 14, Figure 18, Figure 19, Figure 20 and Figure 21). Nevertheless, internal lithology variations, as identified on seismic sections, and the heterogeneity of sediments represented by overlapping resistivity ranges, often lead to ambiguous lithological interpretation.

3.4.6 Verification of the 3D geological subsurface models by means of HFEM forward modelling

The apparent resistivity values at each frequency of the HFEM survey (Figure 24A) were compared with the apparent resistivity values derived from the initial 3D geological subsurface model, based on borehole and seismic data (Figure 24B) and the adjusted 3D geological subsurface model was derived from the 3D AEM resistivity grids (Figure 24C). This allowed identification of differences and uncertainties in each dataset.

At each HFEM data point, the thickness and the median resistivity value of each geological unit derived from the different 3D geological subsurface models (Table 1 and Table 2) were used to create a 1D resistivity model. For all 1D models, synthetic HFEM data were derived by forward calculation (Siemon, 2012). To verify the HFEM data, apparent resistivities were

used to compare the measured and modelled HFEM data for two reasons: 1) The apparent resistivities are almost always independent of altitude variations of the HFEM system (Siemon et al., 2009a), and 2) they represent an approximation of the true resistivity distribution in the subsurface. The corresponding depth levels, however, vary as the centroid depth values depend on the penetration depth of the electromagnetic fields.

3.4.7 Fracture analysis in the study area of the Lutter anticline

Field data of fracture orientation

Detailed fracture mapping made by Hosseinidust (1980; based on 5405 measurements; cf. Figure 4) and my own geological field observations are used for correlation between resistivity trends and fracture set orientations (Figure 14, Figure 28 and Figure 29).

At seven outcrops, I collected 277 fracture and bed orientation datasets in the most accessible and exposed parts of the Lutter anticline. The fracture orientation was measured with a Clar compass and visualized on lower-hemisphere stereographic projections. Most of the analysed outcrops are located along the topographic ridges of the anticline, where Mesozoic rocks are exposed. Fracture populations (or sets) were defined on the basis of common orientation (strike and dip). The software Stereo32© was used to present the results of the analysis on stereonet of the orientation data from each measurement site. The results of fracture orientation are in good accordance with the results made by Hosseinidust (1980). Fractures were treated in the same way in the statistical analysis of fracture orientations and were considered as indicative of paleostress orientation.

Fracture detection by curvature application

Bedrock diversity causes the development of specific fractures to have a direct connection to the flow system of surface and groundwater. Subsequently, differences between fractures and fracture systems filled with water and the host rocks should correlate with changes in resistivity (Palacky, 1987; Paine & Collins, 2017).

For the enhancement of the faintest resistivity variations in bedrock, an improved method for a fast and efficient mapping of the regional distribution and organization of small-scale structural features is needed. The method used for the detection of local fracture and fracture systems is based on interpretation of geometry attributes of subtle resistivity signatures. The interpretation of geometry attributes is not new at all and has a proven track-record in oil industry for seismic interpretation (Roden et al., 2015) and many other industries and disciplines outside geology, e.g. medicine and terrain analysis. It is evident, from each of these geometric attributes, that there is an improvement in the image delineation of fault/fracture trends with the spectral decomposition volumes.

Geometric attribute features in GOCAD software (Paradigm, 2011) were used to analyse the resistivity pattern to determine the bed orientation and to detect small-scale changes corresponding to folds, faults and fractures. Especially fractures are important fabrics, because the bisector of the acute angle in the fracture set defines the orientation of the maximum principle stress of deformation (Hancock, 1985). Furthermore, the direct connection of fractures to the flow system of surface and groundwater is an important benefit for drinking-water supply.

From the infinite number of possible geometry attributes, only a small subset of especially curvature attributes were used, which were found to be most applicable to resistivity data. The purpose of a surface-related attribute like curvature is to enhance or give rise to a particular aspect or property of a surface, which may otherwise be difficult or impossible to observe, without introducing artefacts. Curvature is a two-dimensional property of a curve and describes how strong the curve is at any particular point on the curve, i.e. how much the curve deviates from a straight line at this point (cf. Figure 15). The two-dimensional concept can easily be extended into three-dimensions of a surface by comparing it to a plane. The intersection that the plane makes with the surface describes a curve from which curvature can be calculated at any point along the curve. From the infinite number of orthogonal normal curvatures, which pass through a particular point on a surface, a curve exists that defines the

largest absolute curvature. This is called the maximum curvature and the perpendicular curvature is called the minimum curvature (Roberts, 2001).

All the curvature attributes presented in this thesis are based on a curvature analysis of the 3D resistivity grid and the first 30 m beneath the surface. Examination of the resistivity grid indicates that the data is generally of good quality and in continuity with the mapped stratigraphic bedding.

In order to calculate the curvature at a particular point, a local quadratic surface was fitted in a least-squares sense by using the surrounding grid cells. The approach is able to find orientation and continuity trends within the resistivity grid and to compute the maximum curvature and an azimuth value for each cell. The software enables one to display the results as a histogram (Figure 31). A comparison of 3D resistivity pattern with topographic base maps was used for verifying the sources for electromagnetic anomalies.

The use of the maximum curvature attribute is very effective at delimiting faults and fault geometries. A fault on this attribute is represented by the juxtaposition of positive curvature values (red/yellow) and negative curvature values (blue). In addition, the curvature also defines the orientation of these faults, as positive and negative curvature values represent the up- and down-thrown side of the fault, respectively.

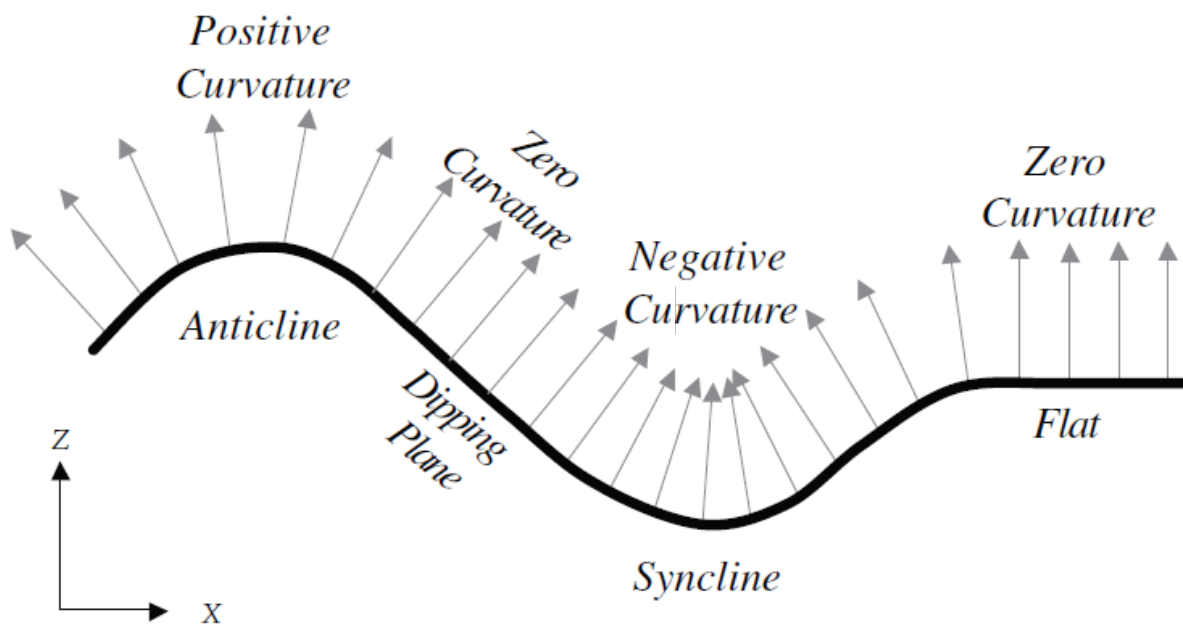


Figure 15: Sign convention for curvature attributes. The grey arrows represent vectors, which are normal for the surface. The curvature measures zero, where these vectors are parallel on flat or planar dipping surfaces. Where the vectors diverge over anticlines, the curvature is defined as positive and where they converge over synclines, the curvature is defined as negative (Roberts, 2001).

4. Results

4.1 Case study 1: The Cuxhaven tunnel valley

4.1.1 Depositional architecture of the Cuxhaven tunnel valley and its Neogene host sediments, as defined by seismic and borehole data analysis

Neogene marine and marginal marine deposits

The Neogene succession is 360 m thick and unconformably overlies open marine to paralic Oligocene deposits (cf. Figure 3C, Kuster, 2005). On the basis of previous investigations of the Neogene sedimentary successions (Gramann & Daniels, 1988; Odin & Kreuzer, 1988; Gramann, 1988, 1989; Overeem et al., 2001; Kuster, 2005; Köthe et al., 2008; Rumpel et al., 2009), four seismic units were mapped within the Neogene deposits (Early to Late Miocene deposits and Pliocene deposits) each bounded at the base by an unconformity. These seismic units can be correlated to seismic units in the North Sea Basin (Michelsen et al., 1998; Møller et al., 2009; Anell et al., 2012). The main characteristics of seismic units, including seismic facies, sedimentary facies and mean resistivity values are summarised in Table 1. The overall thickening observed in the westward dip direction of the seismic units is interpreted as an effect of the salt rim syncline subsidence that created accommodation space (cf. Maystrenko et al., 2005a, b; Grassmann et al., 2005; Brandes et al., 2012).

Seismic unit U1 represents fine-grained, Early to Middle Miocene deposits (23.8-16 Ma) bounded at the base by a high-amplitude reflector, truncating the underlying Oligocene deposits (Table 1; Figure 18A, B and Figure 19A, B). The basal downward-stepping patterns have been interpreted as prograding shelf-shore face deposits (cf., Posamentier & Allen, 1999; Catuneanu, 2002). The upper seismic unit onlaps and conformably overlies the basal deposits and is interpreted as a transgressive and high-stand deposit (Posamentier & Allen, 1999; Catuneanu, 2002).

Seismic unit U2 represents fine-grained, Middle Miocene deposits (16-11 Ma), bounded at the base by a strong continuous high-amplitude reflector, which is partly developed as an erosional surface (Table 1; Figure 18A, B and Figure 19A, B). The basal, downward-stepping

4. Results - Case study 1: The Cuxhaven tunnel valley

patterns are interpreted as prograding shelf-shore face deposits that formed during sea-level lowstand (cf., Posamentier & Allen, 1999; Catuneanu, 2002). In the upper part, the retrogradational and aggradational reflector patterns indicate deposition of open marine sediments during transgression and sea-level highstand (Posamentier & Allen, 1999; Catuneanu, 2002; Kuster, 2005).

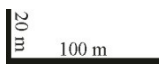
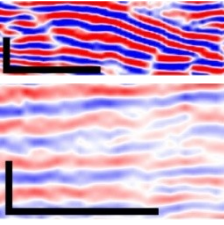
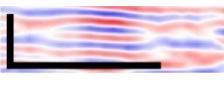
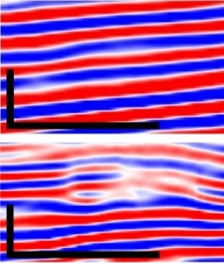
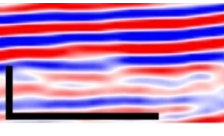
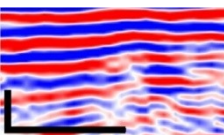
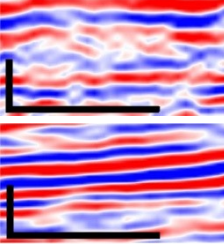
Seismic unit U3 represents Late Miocene (11-5.3 Ma), storm-dominated, shelf and shore face deposits bounded at the base by an erosional unconformity (Table 1; Figure 18A, B and Figure 19A, B). Basal reflectors with onlap terminations indicate deposition during sea-level rise (cf., Posamentier & Allen, 1999; Catuneanu, 2002). The maximum flooding surface is indicated by a continuous, high-amplitude reflector that separates the lower, retrograding strata from the overlying prograding highstand strata (Posamentier & Allen, 1999; Catuneanu, 2002; Catuneanu et al., 2011).

Seismic unit U4 (Table 1; Figure 18A, B and Figure 19A, B) is interpreted as an incised-valley fill based on the overall lens-shaped geometry (Dalrymple, 1992; Møller et al., 2009; Catuneanu et al., 2011). It is bounded at the base by an erosional unconformity that deeply cuts into seismic unit U3 (Table 1; Figure 18A, B and Figure 19A, B). The formation of this incised valley might be related to the eustatic sea-level fall at the end of the Messinian, which approximately reached 90 m (Miller et al., 2005). During this time, deeply-incised valleys formed offshore Denmark (Møller et al., 2009). The NNW-SSE trending valley may indicate an early course of the River Weser or Elbe, although this is speculative because no borehole data are available from the central valley-fill deposits. Paleomagnetic and bio-stratigraphic data (Daniels & Gramann, 1988; Gramann, 1989) from a borehole, located approximately 3 km northwest of seismic line S1, probably at the incised-valley margin, reveal Early Pliocene, fine-grained marine deposits (Kuster, 2005). Therefore, the basal incised-valley fill is probably Early Pliocene in age. The sub-parallel pattern of the lower valley fill (seismic lines S1 and S2; Table 1; Figure 18A, B and Figure 19A, B) have been interpreted as transgressive estuarine deposits (Dalrymple et al., 1992; Reinson, 1992; Veeken & van Moerkerken, 2013). Evidence for a transgressive back stepping is indicated by onlap reflector terminations onto the truncation surface on seismic line S1 and S2. The effects of ravinement erosion coupled with fluvial onlap may have resulted in the formation of a sub-aerial unconformity to be directly overlain by transgressive strata (Dalrymple, 1992; Catuneanu, 2002; Strong & Paola, 2008; Embry, 2009). The upper part of the incised-valley fill is characterised by mound- and small-scale U-shaped elements, interpreted as prograding deltalobes (Plink-Björklund, 2008).

4. Results - Case study 1: The Cuxhaven tunnel valley

Borehole data from adjacent marginal areas reveal marine to paralic sediments, which are rich in heavy minerals (Gramann, 1989; Kuster, 2005).

Table 1: Seismic and sedimentary facies of the Oligocene and Neogene marine to marginal marine deposits.

	<i>Seismic pattern</i>		<i>Sedimentary facies</i>	<i>Interpretation</i>	<i>Seismic Unit</i>	<i>Thickness [m]</i>	ρ [Ωm]			
							<i>B+S</i>	<i>Com.</i>	<i>Adj.</i>	
Miocene	Pliocene		Fine-grained sand and silt	Estuarine deposits (Gramann, 1989; Kuster, 2005) of an incised valley	U4	30-120	99	97	100	
			Fine-grained sand	Open shelf to storm-dominated deposits of the upper and lower shoreface (Gramann, 1989; Rasmussen et al., 2010; Rasmussen & Dybkjær, 2013)	U3	15-40	88	90	100	
		Clay and silt coarsening upwards into fine-grained sand	30-85			73	75	40		
	Middle	Serra.		Glauconitic clay and silt	Transgressive shelf deposits (Gramann, 1989; Kuster, 2005; Köthe, 2008; Rasmussen et al., 2010)	U2	10-70	-	-	-
		Lang.		Glauconitic clay, silt and fine-grained sand	Marine outer shelf deposits (Gramann, 1989; Overeem et al., 2001; Kuster, 2005)	U1	10-85	-	-	-
	Early	Burg.								
		Aquit.								
Oligocene			Clay, silt and fine-grained sand	Marine deposits (Gramann, 1989; Kuster, 2005)	U0	~ 220	-	-	-	

Median resistivity values are extracted from the HFEM grid model and are related to the 3D geological subsurface model based on borehole and seismic data (*B+S*), the adjusted 3D geological subsurface model derived from the 3D AEM resistivity grids (*Com.*) and the adjusted 3D geological subsurface model with manually-adjusted resistivity values based on lithology log information (*Adj.*).

Pleistocene and Holocene deposits

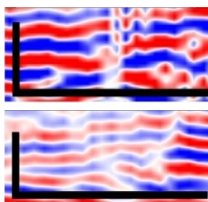
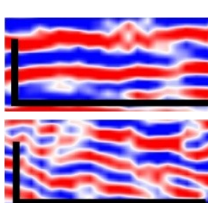
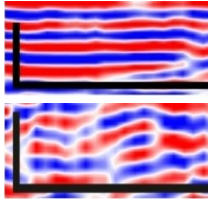
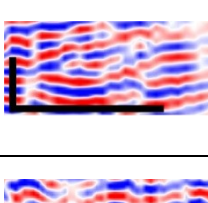
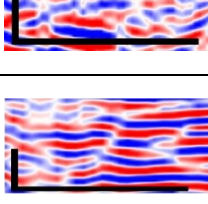
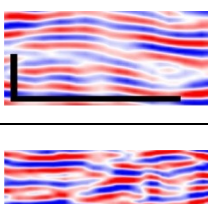
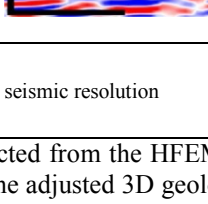
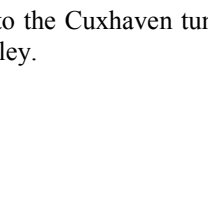
Pleistocene deposits unconformably overly the marginal-marine Neogene sediments and are separated at the base by an erosional surface that is characterised by two steep-walled tunnel valleys that pass laterally into subhorizontal surfaces (Figure 18A, B). The large tunnel valley is up to 350 m deep and 2 km wide (seismic lines S1 and S2, Figure 18A, B and Figure 19A, B) and has previously been described by Kuster & Meyer (1979), Siemon et al. (2002, 2004), Gabriel et al. (2003), Siemon (2005), Wiederhold et al. (2005a), Gabriel (2006), Rumpel et al. (2009) and BurVal Working Group (2009). The smaller tunnel valley in the east is up to 200 m deep and 1 km wide (seismic line S1, Figure 18A, B). In total, eight seismic subunits were mapped within these tunnel valleys and the marginal areas (U5.1-U5.8; cf. Table 2; Figure 18B and Figure 19B). The main characteristics of seismic subunits, including seismic facies, sedimentary facies, and mean resistivity values are summarised in Table 2.

The dimension, geometry, internal reflector pattern and sedimentary fill of the troughs correspond well to Pleistocene tunnel-valley systems described from northern Germany (Ehlers & Linke, 1989; Stackebrandt, 2009; Lang et al., 2012; Janszen et al., 2013), Denmark (Jørgensen & Sandersen, 2009), the Netherlands (Kluiving et al., 2003) and the North Sea Basin (Wingfield, 1990; Huuse & Lykke-Andersen, 2000; Praeg, 2003; Lutz et al., 2009; Kehew et al., 2012; Moreau et al., 2012). The lowermost tunnel-valley fill (seismic subunit U5.1) is characterised by discontinuous, partly-inclined and hummocky, high- to medium-amplitude reflector pattern interpreted as coarse-grained Elsterian meltwater deposits, as indicated by borehole data.

Seismic subunits U5.2 to U5.5 represent glaciolacustrine deposits that belong to the Lauenburg Clay Complex. This interpretation is based on the overall deposits of clay and fine- to medium-grained sand and the wedge-shaped geometry, which indicates delta or subaqueous fan sedimentation into underfilled tunnel valleys (Lang et al., 2012; Veeken & van Moerkerken, 2013; Moreau & Huuse, 2014). The sharp to erosional bounding surfaces and grain-size variations within seismic subunits U5.2 to U5.6 are related to ice-marginal fluctuations (cf., Janszen et al., 2012a). The glaciolacustrine deposits of the Lower Lauenburg Clay Complex (seismic subunits U5.2 to U5.4) are interpreted as one major transgressive-regressive (ice retreat-ice-advance) cycle (Table 2; Figure 18A, B and Figure 19A, B).

4. Results - Case study 1: The Cuxhaven tunnel valley

Table 2: Seismic and sedimentary facies of the Pleistocene deposits.

		<i>Seismic pattern</i>	<i>Sedimentary facies</i>	<i>Interpretation</i>	<i>Seismic unit</i>	<i>Thickness [m]</i>	ρ [Ω m]			
							<i>B+S</i>	<i>Com.</i>	<i>Adj.</i>	
Holocene		Thickness is below the seismic resolution	Fine-grained sand and peat, contain clay and silt	Salt marsh deposits (Höfle et al., 1985; Knudsen, 1988; Gabriel, 2006)		up to 9	64	64	60	
Pleistocene	Late									
	Wei.									
	Eem.									
	Saalian	Drenthe	Hummocky, low- to high-amplitude reflectors passing laterally into continuous, horizontal-parallel or parallel-inclined reflectors		Fine- to coarse-grained sand and diamicton	Diamicton, glaciofluvial and terminal moraine deposits (Ehlers, 2011)	U5.8 sat. unsat.	10-50	128	138 140 480 500
		Holsteinian	Discontinuous, hummocky to inclined-parallel, high- to medium-amplitude reflectors		Clay, silt and fine-grained sand with shells	Marine to marginal marine deposits (Kuster & Meyer, 1979; Knudsen, 1988)	U5.7 U5.7*	6-45	24 69	32 30
	Middle	Elsterian	Horizontal-parallel, reflectors passing laterally into discontinuous, hummocky high- to medium-amplitude reflectors		Clay and silt with some fine-grained sand	Glaciolacustrine deposits of the Upper Lauenburg Clay Complex (Kuster & Meyer, 1979)	U5.6 U5.6*	10-45	16	14 52 10
			Continuous to discontinuous, hummocky, parallel, medium- to high-amplitude reflectors		Fine- to medium-grained sand, silty	Glaciolacustrine deposits of the Lower Lauenburg Clay Complex (Kuster & Meyer, 1979)	U5.5 U5.5*	20-35	29 100	25 91 25 70
		Discontinuous, hummocky, low- to high-amplitude reflectors		Fine- to medium-grained sand, delta deposit	Glaciolacustrine deposits of the Lower Lauenburg Clay Complex (Kuster & Meyer, 1979; Ortlam, 2001)	U5.4	up to 50	33	34 150	
		Discontinuous, parallel, hummocky, medium- to low-amplitude reflectors, partly transparent		Clay and silt	Glaciolacustrine deposits of the Lower Lauenburg Clay Complex (Kuster & Meyer, 1979)	U5.3	up to 55	31	27 15	
		Parallel-inclined, hummocky, subhorizontal, low- to high-amplitude reflectors		Fine-grained sand fining upwards to silty clay	Fine-grained glaciofluvial deposits (Kuster & Meyer, 1979)	U5.2 U5.2*	25-65	38 66	35 58 35 35	
Discontinuous, partly inclined and hummocky, high- to medium-amplitude reflectors			Coarse-grained sand and gravel fining upwards into medium-grained sand	Coarse-grained glaciofluvial deposits, basal tunnel-valley fill (Kuster & Meyer, 1979)	U5.1	70-160	41	33 120		
Thickness is below the seismic resolution			Fine- to medium-grained sand, silt, pebbles	Proglacial meltwater deposits		up to 10	67	66 70		

Median resistivity values are extracted from the HFEM grid model and are related to the 3D geological subsurface model, based on borehole and seismic data (*B+S*), the adjusted 3D geological subsurface model derived from the 3D AEM resistivity grids (*Com.*) and the adjusted 3D geological subsurface model with manually adjusted resistivity values based on lithology log information (*Adj.*). Seismic subunits U5.1-U5.8 refer to the Cuxhaven tunnel-valley fill. Values marked with *, refer to the small-scale tunnel valley to the east of the Cuxhaven tunnel valley.

4. Results - Case study 1: The Cuxhaven tunnel valley

Seismic subunits U5.5 to U5.6 represent an overall transgression related to the final ice-sheet retreat. According to Knudsen (1993a, b) the uppermost Lauenburg Clay Complex (U5.6) was already under marine influence. The fine-grained, glacial deposits of the Lauenburg Clay Complex are restricted to the tunnel valleys and are unconformably overlain by marine Holsteinian interglacial deposits (U5.7). The strong seismic reflectivity contrast indicates interbedded clay, silt, and fine-grained sand and can be correlated with borehole data (cf., Kuster & Meyer, 1979; Knudsen, 1988, 1993a, b; Janszen, 2012; Janszen et al., 2012; Table 2; Figure 18A, B and Figure 19A, B). Seismic subunit U5.8 covers the entire seismic sections (Table 2; Figure 18A, B and Figure 19A, B) and is interpreted as Saalian meltwater deposits and till, which unconformably overlie the Neogene, Elsterian and Holsteinian deposits. The strong lateral variation of the reflector pattern within the tunnel valley might indicate prograding delta lobes into the abandoned tunnel valley, as it has also been described by Lang et al. (2012), Janszen (2012) and Janszen et al. (2012) in other tunnel valleys. The continuous horizontal-parallel reflector pattern at the tunnel-valley margin points to a glaciofluvial deposition.

Figure 17 presents a sketch of the paleogeographic reconstruction of the Bremerhaven-Cuxhaven area.

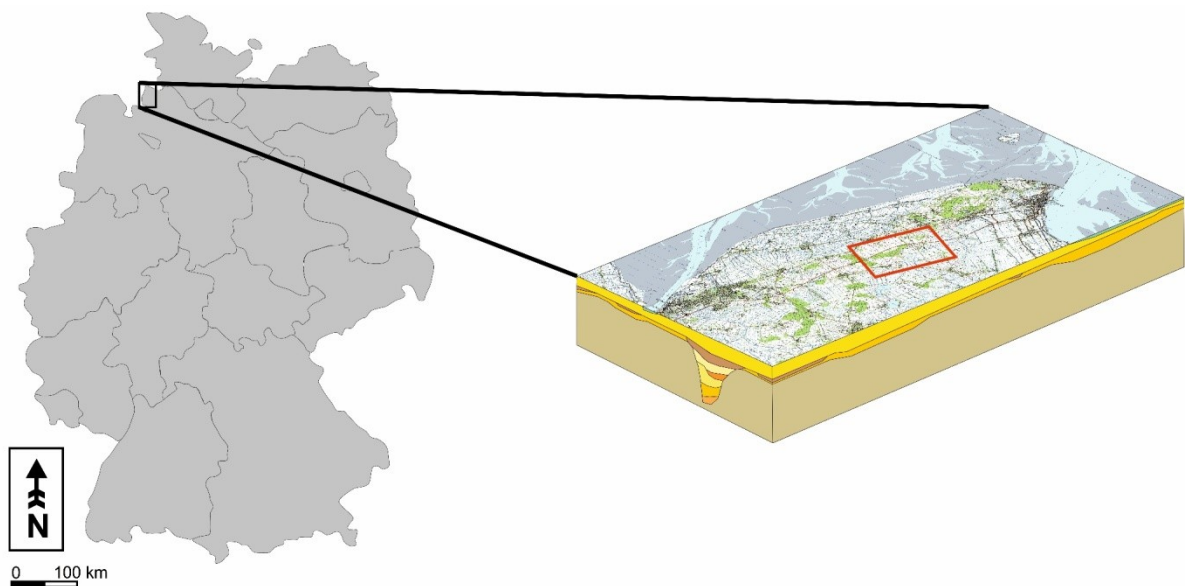


Figure 16: Overview map of the sketches presented in Figure 17, the paleogeographic reconstruction.

4. Results - Case study 1: The Cuxhaven tunnel valley

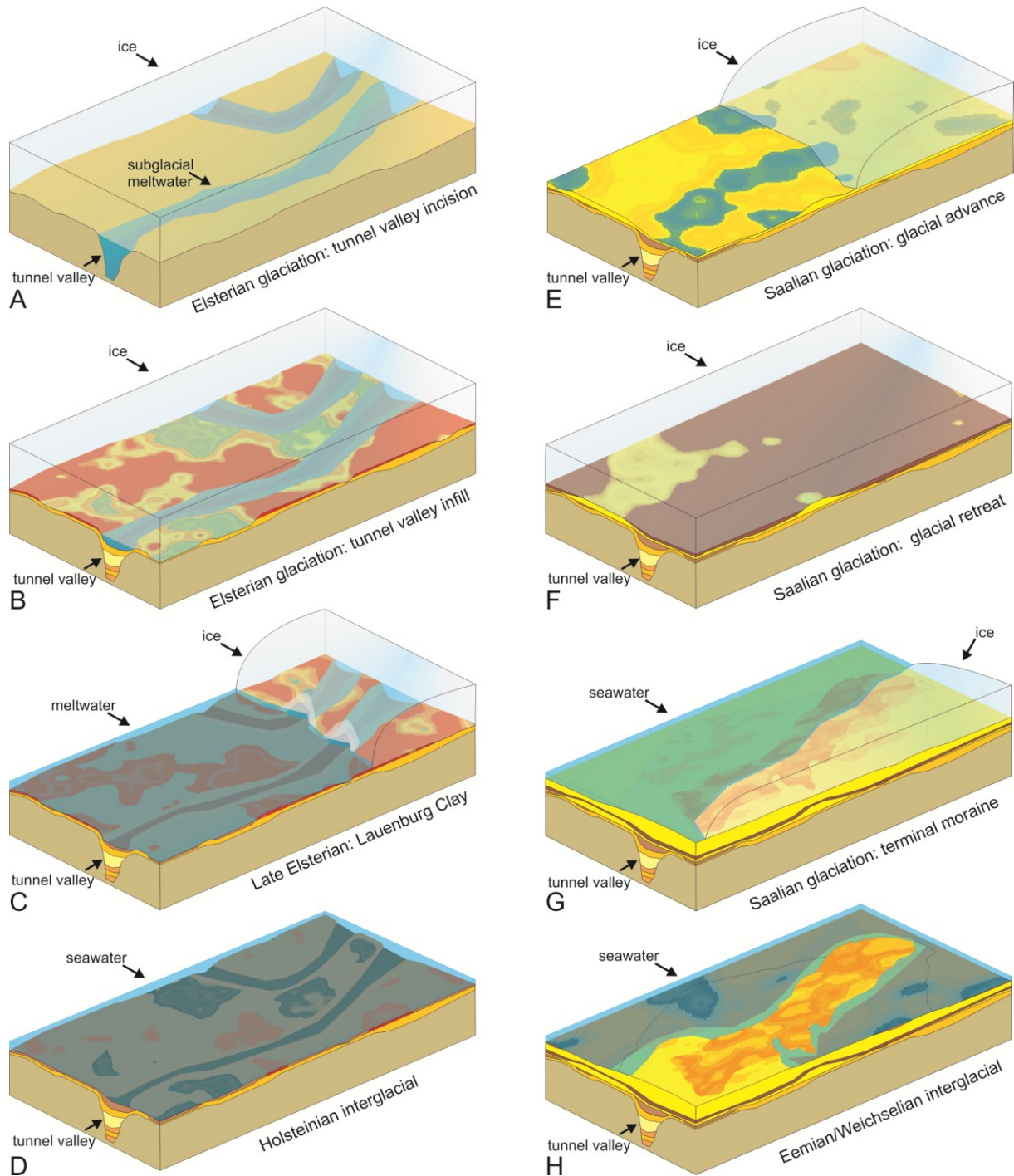


Figure 17: Paleogeographic reconstruction of the Bremerhaven-Cuxhaven area (figures are not to scale). (A) Formation of tunnel valley incisions during Elsterian glaciation. (B) Tunnel valley infill and deposition of subglacial till during Elsterian glacial retreat. (C) Formation of a probably subglacial lake during the Late Elsterian glaciation. (D) Formation of a marine environment during the Holsteinian interglacial. (E) Saalian ice advance. (F) Deposition of subglacial till during the Saalian glacial retreat. (G) Formation of a terminal moraine during the Saalian glaciation. (H) Formation of wetlands during the Eemian and Weichselian.

4.1.2 Integration of the resistivity grid model and the geological subsurface model

Comparison of borehole resistivity logs with model resistivity data

The borehole HI9 Wanhoeden penetrates the western marginal tunnel-valley fill (cf. Figure 6C and Figure 18B). The lowermost fill consists of Elsterian glaciolacustrine fine- to medium-grained sand and silt alternations of the Lower Lauenburg Clay Complex (U5.2-5.4). It underlies the Upper Lauenburg Clay Complex which consists of clay, silt and fine-grained sand alternations (U5.5-5.6) and marine Holsteinian interglacial deposits (U5.7; Figure 18B and Figure 22). The resistivity log of borehole HI9 displays strong resistivity variations, which can be correlated with the alternation of clay- and sand-rich beds (Figure 22). The 3D resistivity grid model based on 1D HFEM inversion results displays a similar resistivity log to the one in the borehole and thus a good lithological match. The upper bounding surface of the Upper Lauenburg Clay Complex and of the marine interglacial Holsteinian clay can be also identified on the 3D resistivity grid (Figure 22). The interpolated 3D resistivity grid based on 1D HTEM inversion results, however, reveals only one conductor. While the Upper Lauenburg Clay Complex is nearly fully imaged, the interglacial marine Holsteinian clay is not well defined, which may be caused by the limited resolution of the TEM method. The highly conductive sediments of the Upper Lauenburg Clay Complex lead to a reduced penetration of the EM fields and hence, resistivities of the sediments below the Upper Lauenburg Clay Complex are not detectable with the transmitter moments that are used in this survey.

An important difference between resistivity values of the measured resistivity log of borehole HI9 and the extracted values from the 3D resistivity grids based on 1D AEM inversion results is the amplitude of high resistivity values, which is considerably lower in the 3D resistivity grids (Figure 22). This difference can be explained by the applied AEM methods, which are more sensitive to conductive sediments (Steuer et al., 2009). In addition, the AEM system predominantly generates horizontal currents, whereas EM borehole systems use vertical currents for measuring the log resistivity. Sediment anisotropy as well as scaling effects have to be taken also into account.

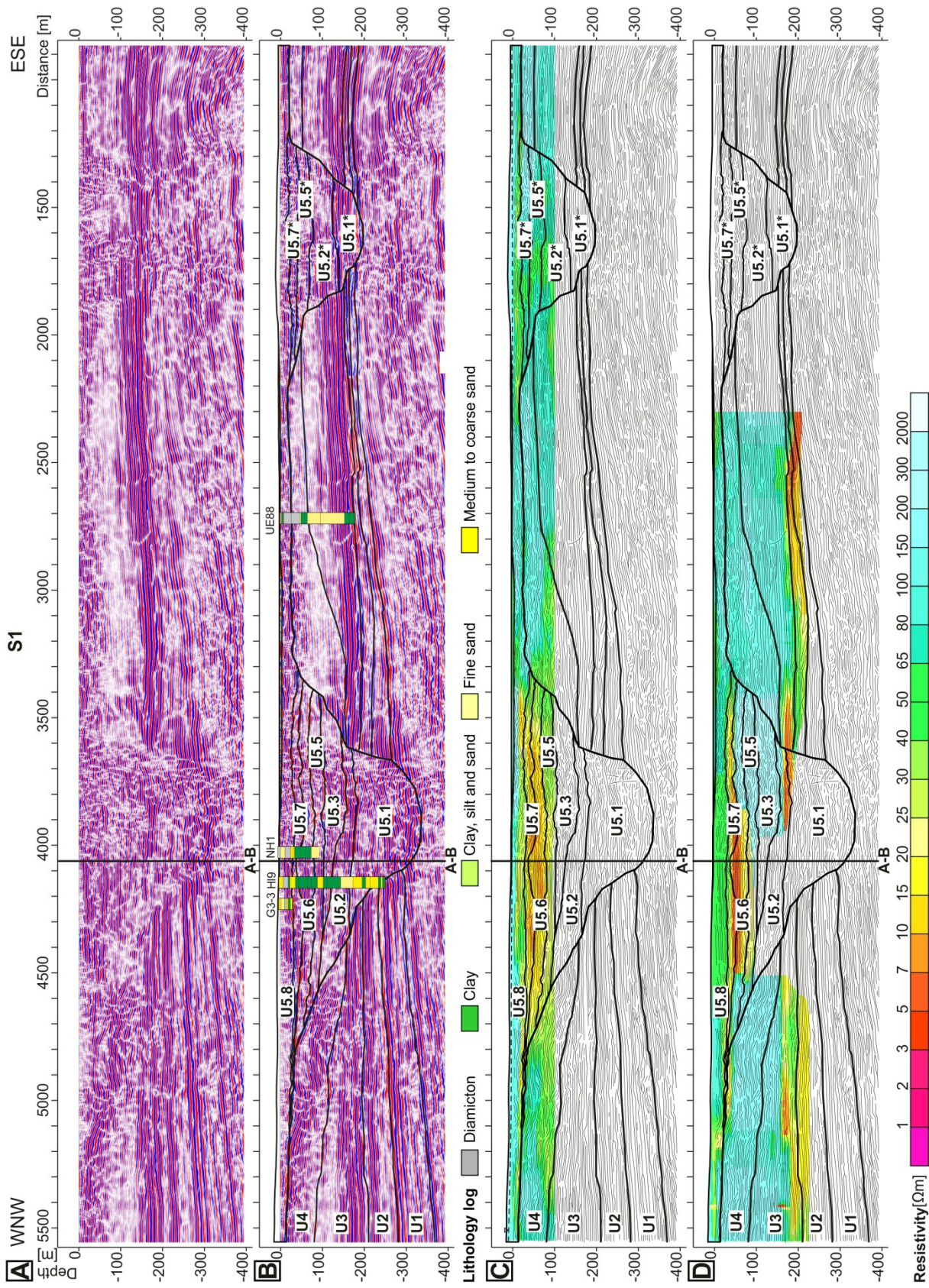


Figure 18: 2D reflection seismic section S1 combined with borehole logs. Seismic units are described in tables 1 and 2. (C) 2D reflection seismic section S1 combined with resistivity data, extracted from the 3D HFEM resistivity grid. Dashed line indicates the groundwater table. (D) 2D reflection seismic section S1 combined with resistivity data, extracted from the 3D HTEM resistivity grid. For location see Fig. 1C and D.

4. Results - Case study 1: The Cuxhaven tunnel valley

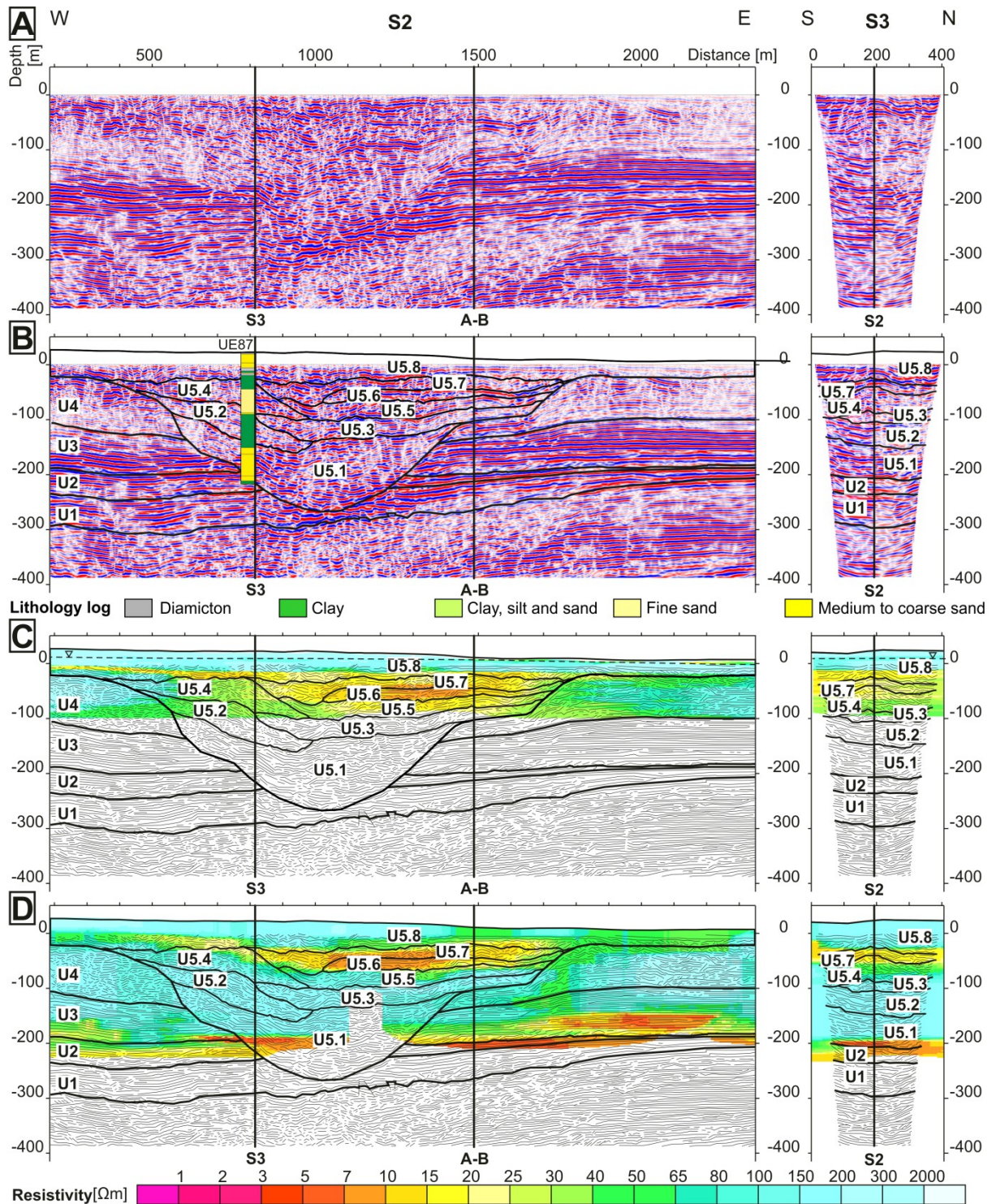


Figure 19: 2D reflection seismic sections S2 and S3 combined with airborne electromagnetic data. (A) 2D reflection seismic sections S2 and S3. (B) Interpreted seismic sections S2 and S3 with borehole logs. Seismic units are described in Tables 1 and 2. (C) 2D reflection seismic sections S2 and S3 combined with resistivity data, extracted from the 3D HFEM resistivity grid. Dashed line indicates the groundwater table. (D) 2D reflection seismic sections S2 and S3 combined with resistivity data, extracted from the 3D HTEM resistivity grid. For location see Figs. 1C and 1D.

4. Results - Case study 1: The Cuxhaven tunnel valley

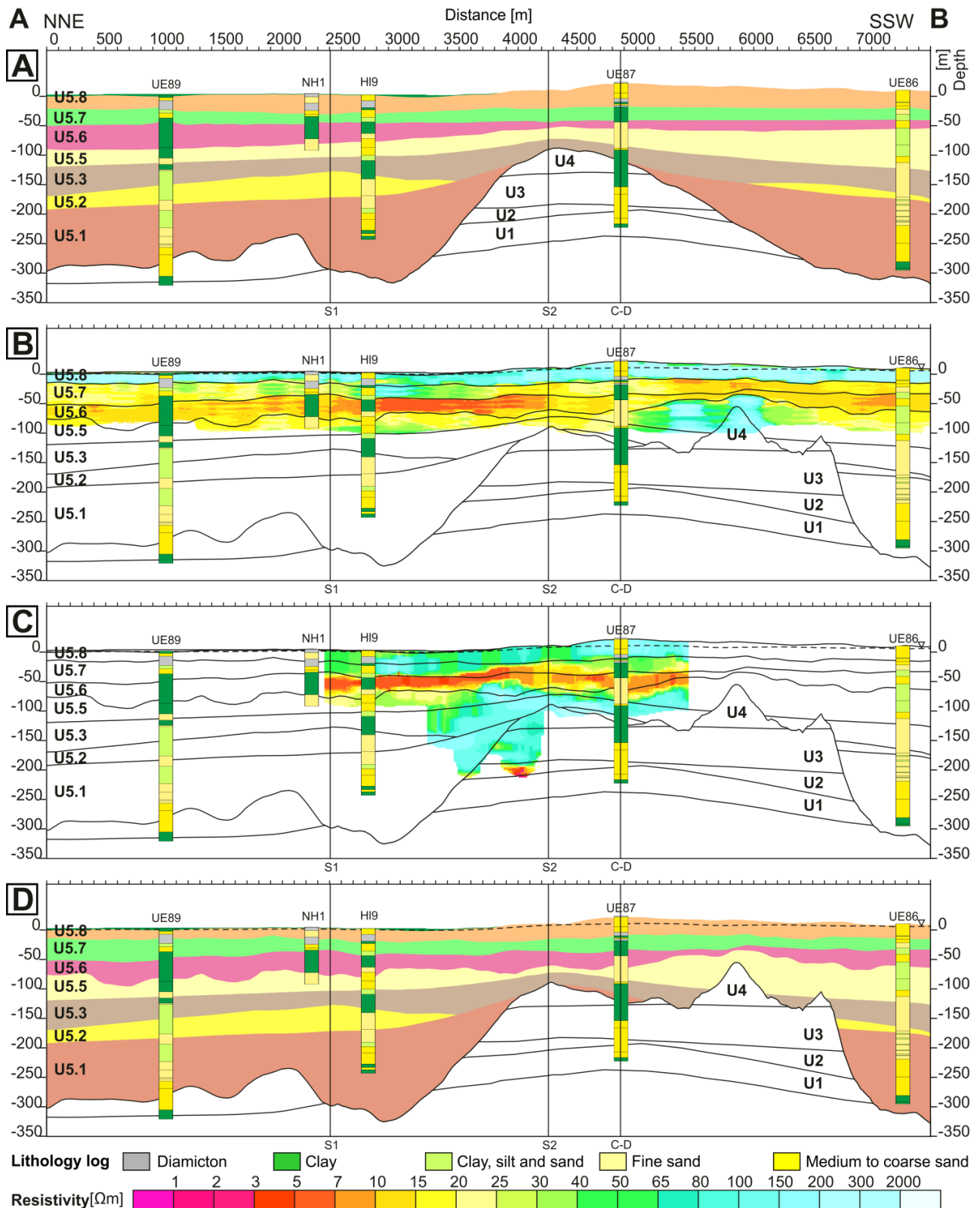


Figure 20: 2D cross-section of the study area (A-B in Figure 6C and D), showing major bounding surfaces and resistivity values based on borehole, seismic and AEM data. Dashed line indicates the groundwater table. (A) 2D cross-section extracted from the 3D geological model based on borehole and seismic data. Only the Pleistocene deposits are shown in colour. (B) 2D cross-section extracted from the adjusted 3D geological model and the corresponding resistivities derived from the 3D HFEM voxel grid. (C) 2D cross-section extracted from the adjusted 3D geological model and the corresponding resistivities derived from the 3D HTEM voxel grid. (D) 2D cross-section extracted from the adjusted 3D geological model. Only the Pleistocene deposits are shown in colour.

4. Results - Case study 1: The Cuxhaven tunnel valley

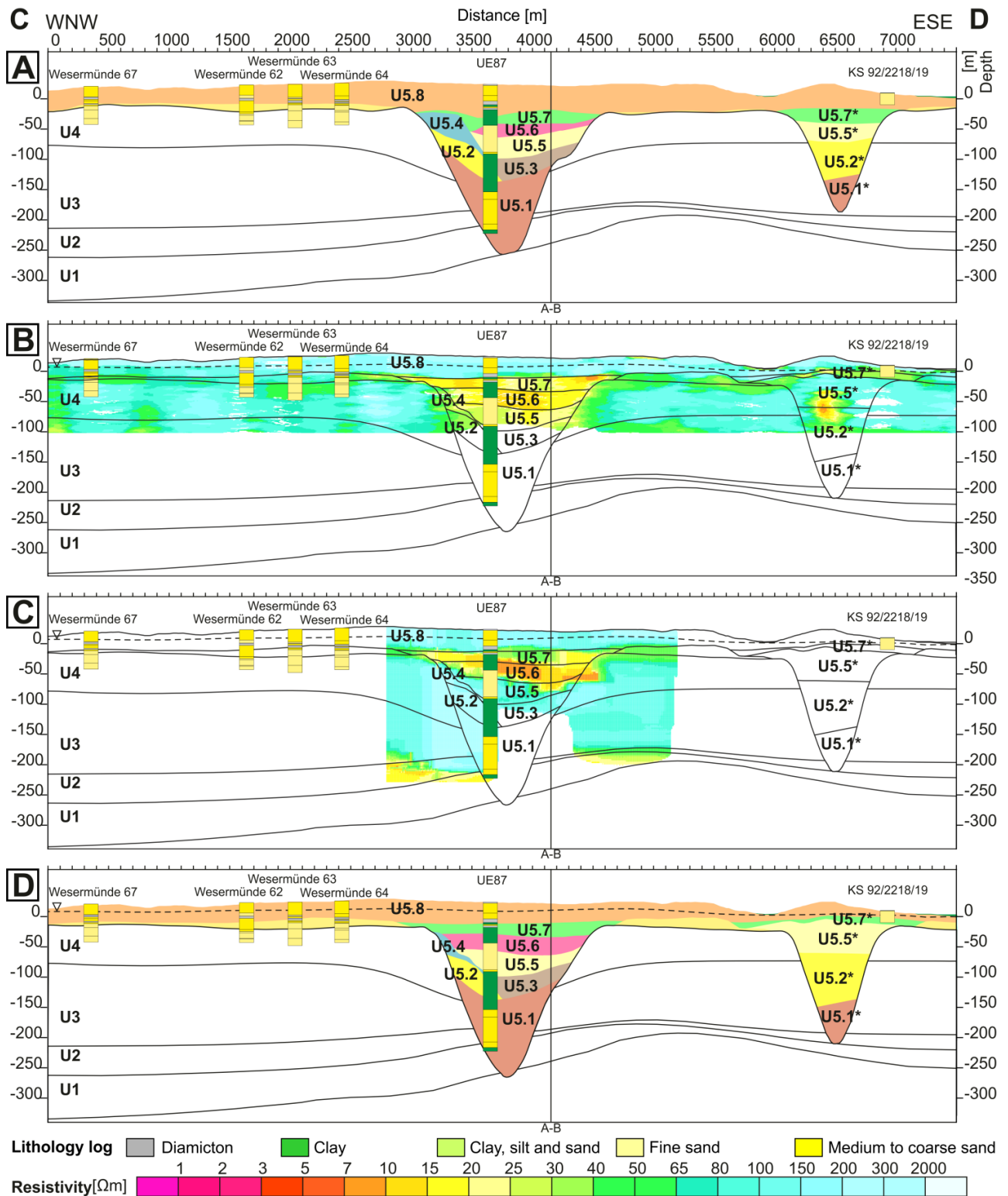


Figure 21: 2D cross-section of the study area (C-D in Figure 6C and D), showing major bounding surfaces and resistivity values based on borehole, seismic and AEM data. Dashed line indicates the groundwater table. (A) 2D cross-section extracted from the 3D geological model based on borehole and seismic data. Only the Pleistocene deposits are shown in colour. (B) 2D cross-section extracted from the adjusted 3D geological model and the corresponding resistivities derived from the 3D HFEM voxel grid. (C) 2D cross-section extracted from the adjusted 3D geological model and the corresponding resistivities derived from the 3D HTEM voxel grid. (D) 2D cross-section extracted from the adjusted 3D geological model. Only the Pleistocene deposits are shown in colour.

4.1.3 Relationship between borehole lithology logs and AEM model resistivities

The analysis shows that resistivity generally increases with grain size and permeability (cf. chapter 3.4.3), also shown by Burschil et al. (2012b) and Klimke et al. (2013) for HTEM data. However, there are substantial differences between borehole lithology and resistivity values derived from the two interpolated 3D AEM resistivity grids (Figure 23). The 3D HFEM resistivity grid indicates that clay (grain-size class 1) has an average resistivity of 30 Ωm in the study area. This value corresponds to previous results of AEM data, commonly reported in the literature for clay (Burschil et al., 2012b; Klimke et al., 2013). In comparison to borehole resistivity (commonly between 5-20 Ωm) the 3D HFEM resistivity value is slightly too high and this may be caused i) by a certain amount of silt and sand content or ii) by the limited resolution of the HFEM method that provide an over- or underestimated thickness or merging of lithological units. The average resistivity value for deposits mainly consisting of clay to silt, is 31 Ωm (grain-size class 2), for clay- and silt-rich fine sand it is 31 Ωm (grain-size class 3), for diamicton it is 80 Ωm (grain-size class 4), for fine sand it is 105 Ωm (grain-size class 5), for silt-rich fine to coarse sand it is 125 Ωm (grain-size class 6) and for fine to coarse sand with gravel it is 125 Ωm (grain-size class 7).

The relationship between borehole lithology and resistivity data extracted from the grid based on 1D HTEM inversion results does not allow lithology to be clearly defined in 3D (Figure 23). The average resistivity value for clay from the dataset (grain-size class 1) is 56 Ωm and may be skewed due to the small sample number. The average resistivity value for deposits mainly consisting of clay to silt is 62 Ωm (grain-size class 2), for clay- and silt-rich fine sand it is 53 Ωm (grain-size class 3), for diamicton it is 115 Ωm (grain-size class 4), for fine sand it is 107 Ωm (grain-size class 5), for silt-rich fine to coarse sand it is 55 Ωm (grain-size class 6), and for fine to coarse sand with gravel it is 85 Ωm (grain-size class 7).

The histograms for both resistivity datasets (see Figure 23) demonstrate that the measured values for sand are higher than for deposits with a certain clay content. However, overlapping resistivity values for sand-dominated sediments and deposits with clay content are generally found to have a lower resistivity range, especially for the HTEM resistivity dataset. The coarser-grained sediments (grain-size class 4 to 7) have a wide variety of resistivity values and seem too low, especially for the HTEM dataset. Figure 23 displays these large resistivity

ranges. The variance in values is interpreted to result from the mixed lithological components, the limited resolution of the AEM system, as well as the less-distinctive imaging of low-conductive sediments.

The larger overlaps of HTEM resistivity values can be explained as effect of restricted HTEM data coverage and the projection of interpolated resistivity values onto the borehole locations. Similar HTEM resistivity values were found at the island of Föhr (Burschil et al., 2012a, b) and for the region of Quakenbrück, southwestern Lower Saxony (Klimke et al., 2013). Nonetheless, discrimination of different lithologies with a wide range of resistivity values is possible by integrating with other datasets, for example borehole or seismic reflection data.

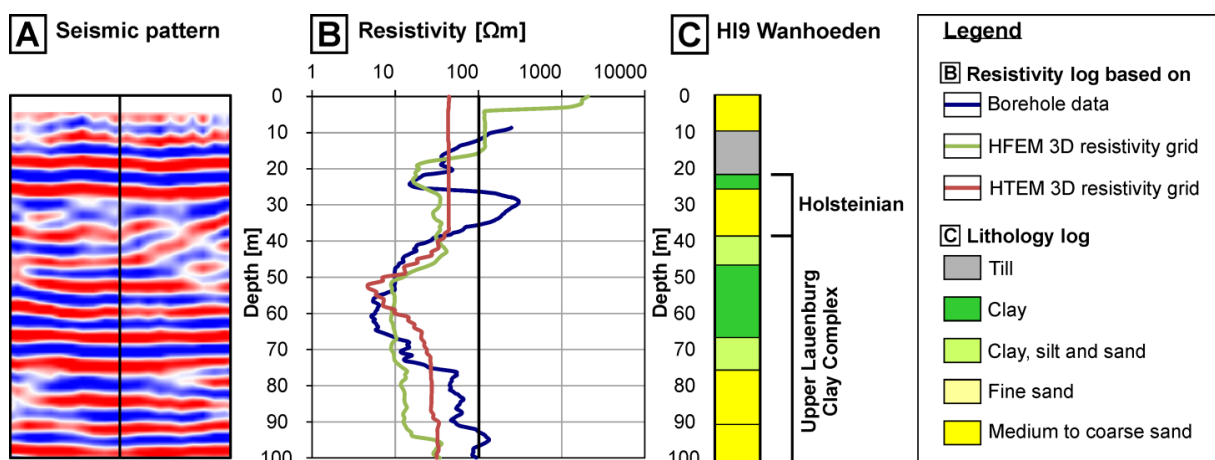


Figure 22: Seismic section (A), resistivity log (B) and lithology log (C) of borehole HI9 Wanhoeden (after Besenecker, 1976). The blue curve shows the measured resistivity log of the borehole; the green curve displays the resistivity log extracted from the 3D HFEM resistivity grid and the red curve displays the projected resistivity log extracted from the 3D HTEM resistivity grid.

4.1.4 Correlation of the HFEM resistivity model with the geological model

Neogene marine and marginal marine deposits

At depths between 10-120 m, the spatial resistivity pattern is characterized by elongate structure with gradual large-scale variations (100-300 m) of medium to high resistivity values that indicate the heterogeneous infill of the Late Miocene incised valley (seismic unit U4; Figure 18C and Figure 19C). A positive correlation with the hummocky seismic reflector pattern and borehole lithology indicates that the resistivity pattern images grain-size variations of vertically- and laterally-stacked delta lobes (cf. Figure 18C and Figure 19C).

Pleistocene deposits

In lithology, the difference between the fine-grained, glacial Pleistocene deposits of the upper tunnel-valley fill and the coarser-grained, Neogene, marginal-marine sediments is expressed as a distinct resistivity contrast, which can be clearly traced at depth (Figure 18C, Figure 19C and Figure 20B).

The margin of the Cuxhaven tunnel valley is indicated by a gradual shift from low to medium resistivity values of Pleistocene deposits (seismic subunits U5.5, U5.6 and U5.7; Figure 18C, Figure 19C, Figure 20B and Figure 21B) to higher resistivity values of the Pliocene host sediments (seismic unit U4; Figure 18C, Figure 19C, Figure 20B and Figure 21B). The resistivity pattern of the HFEM model enables a good three-dimensional imaging of the internal tunnel-valley fill. Large- and small-scale, elongate, wedge-shaped or lens-shaped variations in the resistivity pattern can be correlated with major seismic units and smaller-scale architectural elements, such as individual channels (cf. Figure 18C: U5.7 between 3800-4000 m) and lobes (cf. Figure 18C: U5.6 and U5.7 between 3600-3700 m).

The overall tabular geometry of the glaciolacustrine deposits of the Lauenburg Clay Complex (seismic subunit U5.6) and the marine Holsteinian interglacial deposits (seismic subunit U5.7) are both characterised by low resistivity values in the tunnel-valley centre (Figure 18C, Figure 19C, Figure 20B and Figure 21B) and gradually into higher resistivity values towards the tunnel-valley margin. The higher resistivity values towards the tunnel-valley margin have been interpreted to be the result of bleeding of higher resistivity values from the neighbouring Pliocene sediments. Alternatively, it could be interpreted as an indicator for coarse-grained material (e.g. delta foresets at the margin of the tunnel valley in Figure 19C: U5.2 and U5.4 between 700-800 m; in Figure 18C: U5.5 at 4300 m and U5.6 at 4500 m). The comparison with lithology data from boreholes proves that the Lauenburg Clay Complex (seismic subunit U5.6) and the marine Holsteinian deposits (seismic subunit U5.7) are approximately imaged at the correct depths. The HFEM resistivity pattern however, does not image a distinct boundary between the glaciolacustrine Lauenburg Clay Complex and the marine Holsteinian interglacial deposits due to their similar grain sizes.

Within the tunnel-valley centre, thick, conductive, fine-grained beds of the Lauenburg Clay Complex limit the penetration depth of the HFEM system, leading to a decrease in resolution and a less distinct resistivity pattern of underlying fine- to medium-grained sand (cf. Figure

19C, seismic subunit U5.5 in seismic line S2). Similar results have been also observed by Steuer et al. (2009).

In the eastern part of the study area, lower resistivity values in HFEM data are identified, which differ from the Neogene host sediments. Its geometry and resistivity values suggest a smaller-scale tunnel valley and probably indicate a fill of fine-grained glaciolacustrine (Lauenburg Clay Complex) and/or interglacial marine (Holsteinian) deposits (Figure 18C). The low resistivity contrast between this tunnel-valley fill and the Neogene host sediments probably indicate relatively similar grain sizes, but this remains speculative because no borehole log control is available.

In the uppermost part of the Pleistocene succession, between 0-10 m depth (seismic subunit U5.8; Figure 18C and Figure 19C), a distinct shift from low to very high resistivity values indicates a strong increase in electrical resistivity. This resistivity shift is interpreted to represent the transition between water saturated and unsaturated sediments – it represents the groundwater table contact. This strong resistivity contrast allows the detection of the groundwater table within a range of approximately 2 m and clearly outlines the Hohe Lieth ridge as the most important groundwater recharge area, which has also been documented by Blindow & Balke (2005).

4.1.5 Correlation of the HTEM resistivity model with the geological model

Neogene marginal-marine deposits

At depths between 180-150 m (seismic unit U3), the resistivity pattern is characterised by a sharp contrast from low to medium resistivity values (Figure 18D, Figure 19D, Figure 20B and Figure 21B). This upward increase in resistivity is interpreted as an abrupt facies change from finer-grained shelf deposits to coarser-grained shore face deposits, which is also recorded in borehole data (Kuster, 2005) and might be related to the rapid onset of progradation during the highstand systems tract.

Correlation of the resistivity pattern with borehole data indicates that the low resistivity values tie to marine Early Tortonian clays (seismic unit U3). At depths between 120-80 m, large-

scale, lateral variations of low to medium resistivity values, parallel to seismic reflections, can be identified. Altogether, resistivity contrast and seismic pattern, characterised by strong reflectivity contrasts, are interpreted to result from grain-size variations, which probably indicate the Tortonian to Messinian, storm-dominated, shore-face deposits (seismic unit U3; Table 1; Figure 18D and Figure 19D; Walker & Plint, 1992; Catuneanu, 2002; Kuster, 2005; Catuneanu et al., 2011). Gradual vertical transitions from low to high resistivity values within the upper Neogene unit (seismic unit U4; Figure 18D and Figure 19D) correspond to borehole lithology data, with an overall coarsening-upward trend and are interpreted as prograding delta lobes (e.g. Dalrymple et al., 1992; Plink-Björklund, 2008). This interpretation is further supported by the seismic pattern of lobate units (Figure 18A, B and Figure 19A, B).

Pleistocene deposits

The lithology contrast between the fine-grained glacial Pleistocene deposits at the base and the underlying coarser-grained Neogene marginal-marine sediments is expressed as a distinct change in resistivity, which can be clearly traced in the shallow subsurface between 20-30 m depth and corresponds to the lower boundary of seismic unit U5 (Figure 18D and Figure 19D). The tunnel-valley margin can be identified in borehole data; however in the deeper subsurface it is not clearly imaged by the HTEM resistivity data. At the tunnel-valley margin, the resistivity resembles that of the adjacent Neogene host sediments and therefore its boundary may not be as easily distinguished (Figure 18D, Figure 19D, Figure 20C and Figure 21C). The inability of the HTEM data to have contrasting resistivity values to define the tunnel valley boundary is probably caused by the large lateral footprint of the HTEM system, the inversion approach (SCI) and the kriging method, which leads to a smooth transition between individual resistivity values.

The upper Cuxhaven tunnel-valley fill is characterised by different vertically-stacked resistivity patterns. The highly conductive sediments of the Lauenburg Clay Complex lead to a reduced penetration of the EM field and the resistivity of the sediments below are not detectable with the transmitter moments used in this survey. This suggests that the medium resistivity values, imaged at depths between 160-80 m, do not necessarily show the true resistivities of Pleistocene sand within the tunnel valley recorded in borehole data (seismic subunits U5.1 to U5.4; Figure 18D and Figure 19D). However, the distinct shift towards higher resistivity values in the unit below the highly conductive sediments of the Lauenburg

4. Results - Case study 1: The Cuxhaven tunnel valley

Clay Complex probably indicates coarser-grained deposits of seismic subunit U5.5 (Figure 18D and Figure 19D). At depths between 80-10 m, low resistivity values can be correlated with fine-grained glaciolacustrine sediments of the Lauenburg Clay Complex and interglacial Holsteinian deposits (seismic subunit U5.6 and U5.7; Figure 18D and Figure 19D). The comparison of the resistivity data with the borehole logs and seismic data (Figure 19B) indicates that the resistivity pattern clearly images the correct depth of these depositional subunits.

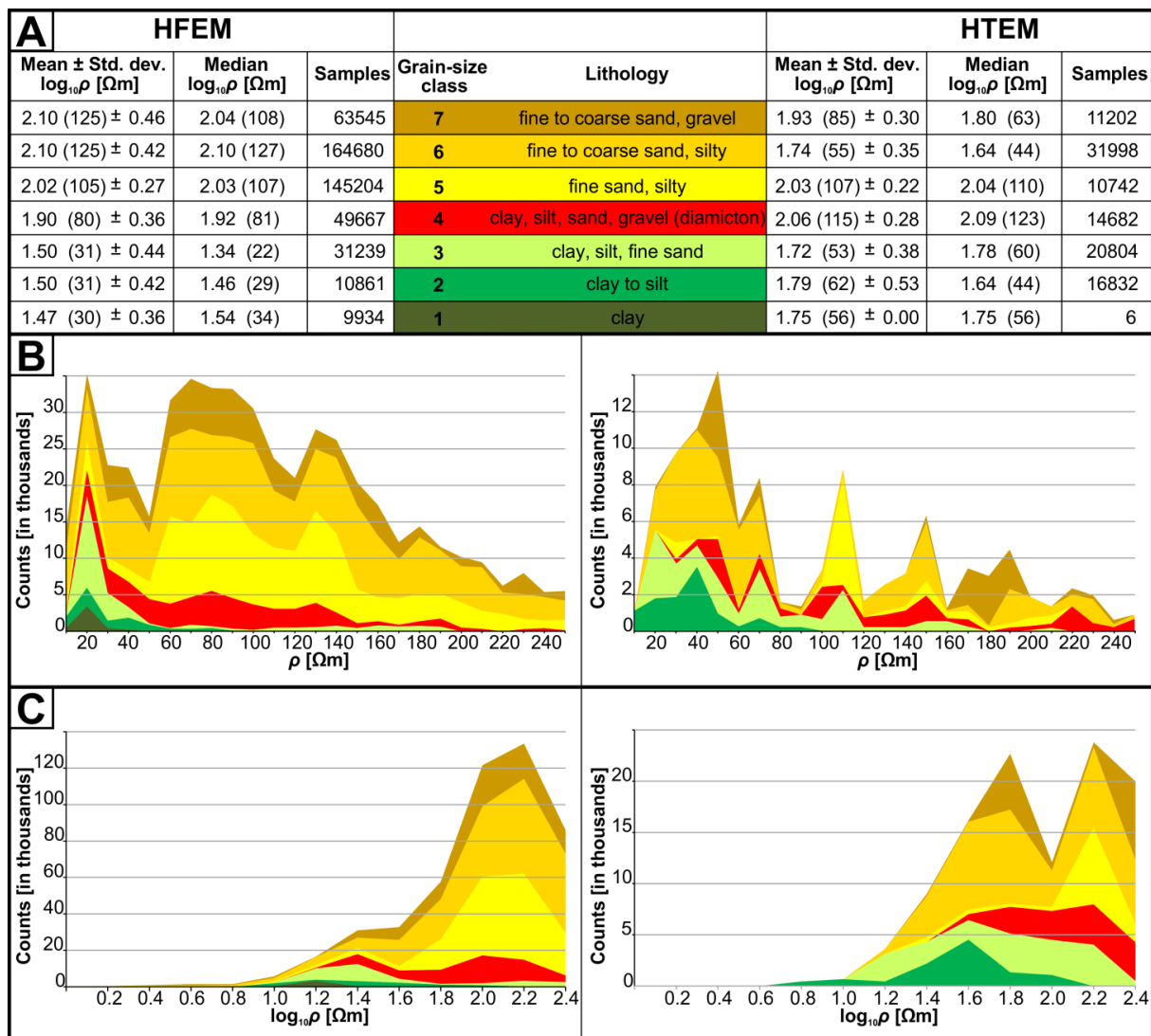


Figure 23: Grain-size classes and related resistivity histograms extracted from the interpolated 3D HFEM and HTEM resistivity grid. A) Grain-size classes and related resistivity extracted from the interpolated 3D HFEM and HTEM resistivity grid. Mean values, standard deviation, median values, number of counts for common resistivity (logarithmic values) are shown. B) Histogram showing resistivity classes of HFEM and HTEM data for each grain-size class as stacked bars (linear scale). C) Histogram showing resistivity classes of HFEM and HTEM data for each grain-size class as stacked bars (logarithmic scale). The absence of resistivity values lower than $1 \log_{10} \Omega\text{m}$ indicates that the influence of anthropogenic noise and saltwater can be excluded.

4.1.6 Verification of apparent resistivity values extracted from the 3D subsurface models

The comparison of the apparent resistivity values derived from the HFEM data (Figure 24A), the initial geological subsurface model based on borehole and seismic data (Figure 24B) and the adjusted geological subsurface model derived from the 3D AEM resistivity grids (Figure 24C) generally show a relationship that indicates that both geological models are able to explain the principal resistivity distribution at several HFEM frequencies. The apparent resistivity images of the initial 3D geological subsurface model show a relatively sharp resistivity contrast between the Pleistocene tunnel valley and the adjacent Neogene deposits (Figure 24B), particularly at the lower frequencies (at greater depths), defining a simple tunnel-valley geometry with a low sinuosity. The apparent resistivity map derived from the initial 3D geological subsurface model (B), however, does not image the tunnel-valley fill at the highest frequency (at shallow depths). The difference between the apparent resistivity images can be explained by the limited coverage of borehole and seismic data, which leads to restricted information about the subsurface architecture. The apparent resistivity images of the adjusted 3D geological subsurface model derived from the 3D AEM resistivity grids (Figure 24C) show a more complex tunnel-valley geometry characterised by a higher sinuosity and smaller-scale variations of the resistivity pattern. This more complex interpretation of the tunnel valley can be better aligned with the apparent resistivity images of HFEM data (Figure 24A) and the lithology variations recorded by borehole data. Nevertheless, uncertainties remain and are caused by the decreasing resolution with depth, which may lead to less contrast in the resistivity images. This is especially apparent at the lowest frequency, whereby the resistivity images are influenced by underlying sediments. This often leads to the bottom layer of the 1D inversion models being incorrect. This problem was reduced by the manual adjustment of resistivity values of bottom units in the adjusted 3D geological subsurface model that was derived from the 3D AEM resistivity grids based on lithology information (i.e. particularly the resistivity value for the lower part of unit U3 representing clay and silt was reduced by a factor of about 2; cf. Table 1). The resistivities of the valley infill were adjusted if the calculated mean values were misleading for the sediment type (i.e. too high resistivities attributed to clay and silt units were reduced, e.g. seismic subunit U5.3, and too low resistivities attributed to sandy units were increased, e.g. seismic subunit U5.1 and U5.4; cf. Table 2). Some other values were rounded up.

4. Results - Case study 1: The Cuxhaven tunnel valley

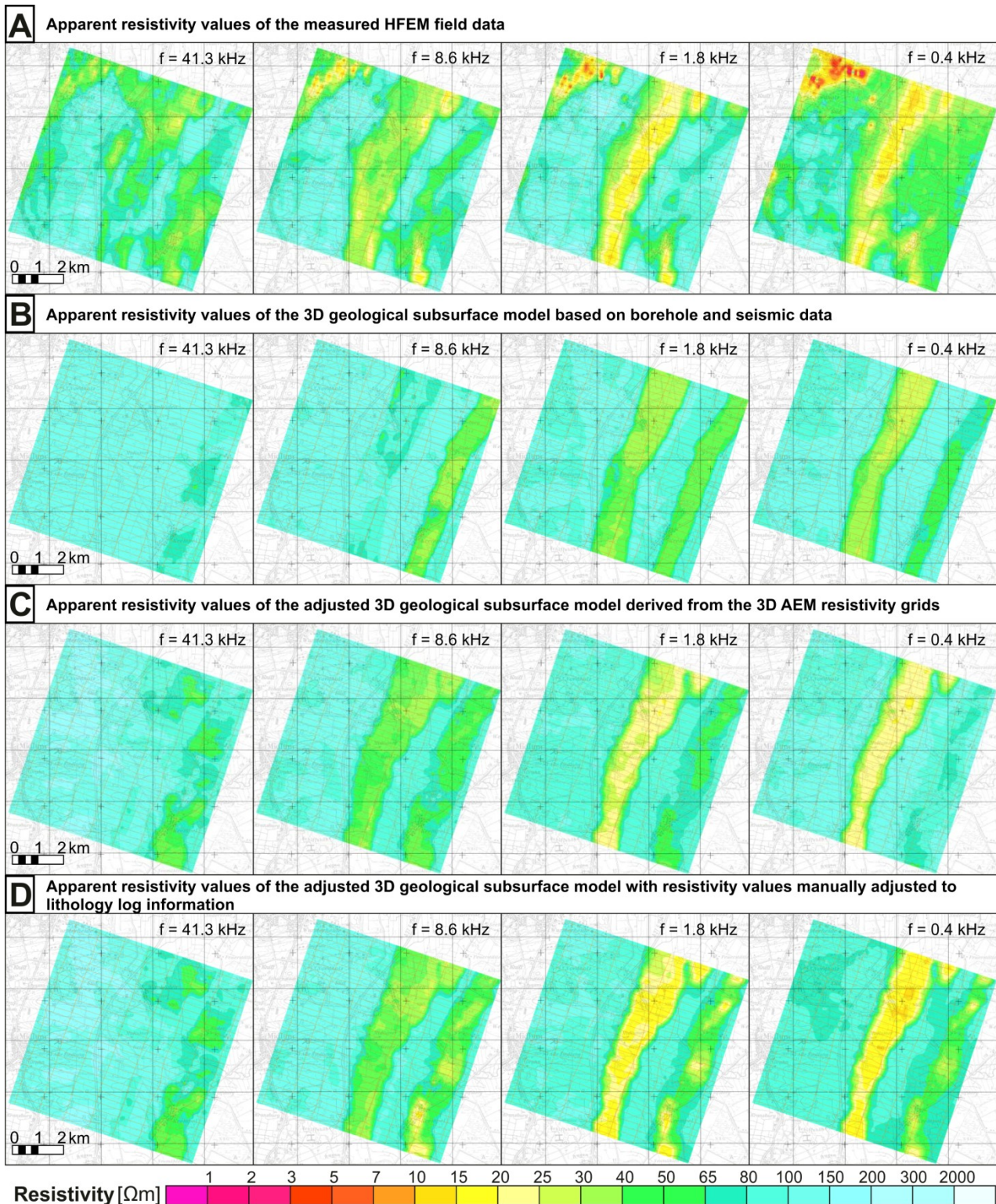


Figure 24: Apparent resistivity images at different frequencies, corresponding to centroid depths, which increase from left to right. (A) Apparent resistivity images of measured HFEM data. (B) Apparent resistivity images extracted from the 3D geological subsurface model based on borehole and seismic data. (C) Apparent resistivity images extracted from the adjusted 3D geological subsurface model derived from AEM data. (D) Apparent resistivity images extracted from the adjusted 3D geological subsurface model derived from AEM data with manually adjusted resistivity values based on lithology log information.

4. Results - Case study 1: The Cuxhaven tunnel valley

The apparent resistivity values were recalculated after correction (Figure 24D). These resistivity images represent the subsurface architecture much better and are closer to the apparent resistivity maps represented in the HFEM data, i.e. the adjusted geological model explains the HFEM data in a more effective manner. Nevertheless, differences in the images of the apparent resistivity patterns remain. This is caused by a resolution of the 3D geological subsurface model, which is too low and which does not represent detailed sediment variability, and incorrectly estimated resistivities attributed to the geological units. A good example of this effect is the area of the smaller tunnel valley in the eastern part of the study area (Figure 24D), where the clay and silt deposits (lower part of U3) are obviously thinner or/and resistive and the central part of the valley fill U5.5* was estimated to be too broad and too conductive. On the other hand, the low apparent resistivities in the northwest of the study area, which occur particularly at low frequencies, are caused by anthropogenic sources (airport Cuxhaven/Nordholz).

4.2 Case study 2: The Lutter anticline

4.2.1 The 3D geological subsurface model

The 3D structural model of the Lutter anticline was built based on published geological depth maps and a resistivity subsurface model of processed AEM-datasets that were constructed in this study (Figure 14). This allows to produce a robust, common subsurface model.

The resistivity analysis revealed several different rock types and the location and orientation of faults. The resistivity pattern matches the geological map, which indicates that the resistivity is strongly controlled by the lithology of the near surface rocks (Jordan & Siemon, 2002). Thus it was possible to connect specific resistivity values to individual lithologies (Figure 25).

This allows the use of changes in resistivity as an indicator for changes in lithology. The initial bounding surfaces of the 3D geological subsurface model were adjusted based on the AEM data. High resistivities in the southern study area clearly correspond to greywackes of the Harz Mountains (Figure 26). Mesozoic mudstones and siltstones are represented by low resistivity values, whereas Mesozoic limestones and sandstones are characterized by high resistivity values. The tilted limestones of the Lower Muschelkalk are clearly detectable due to their high resistivities. Main fault and fracture zones were detected by disruptions and offsets in the resistivity pattern.

4. Results - Case study 2: The Lutter Anticline

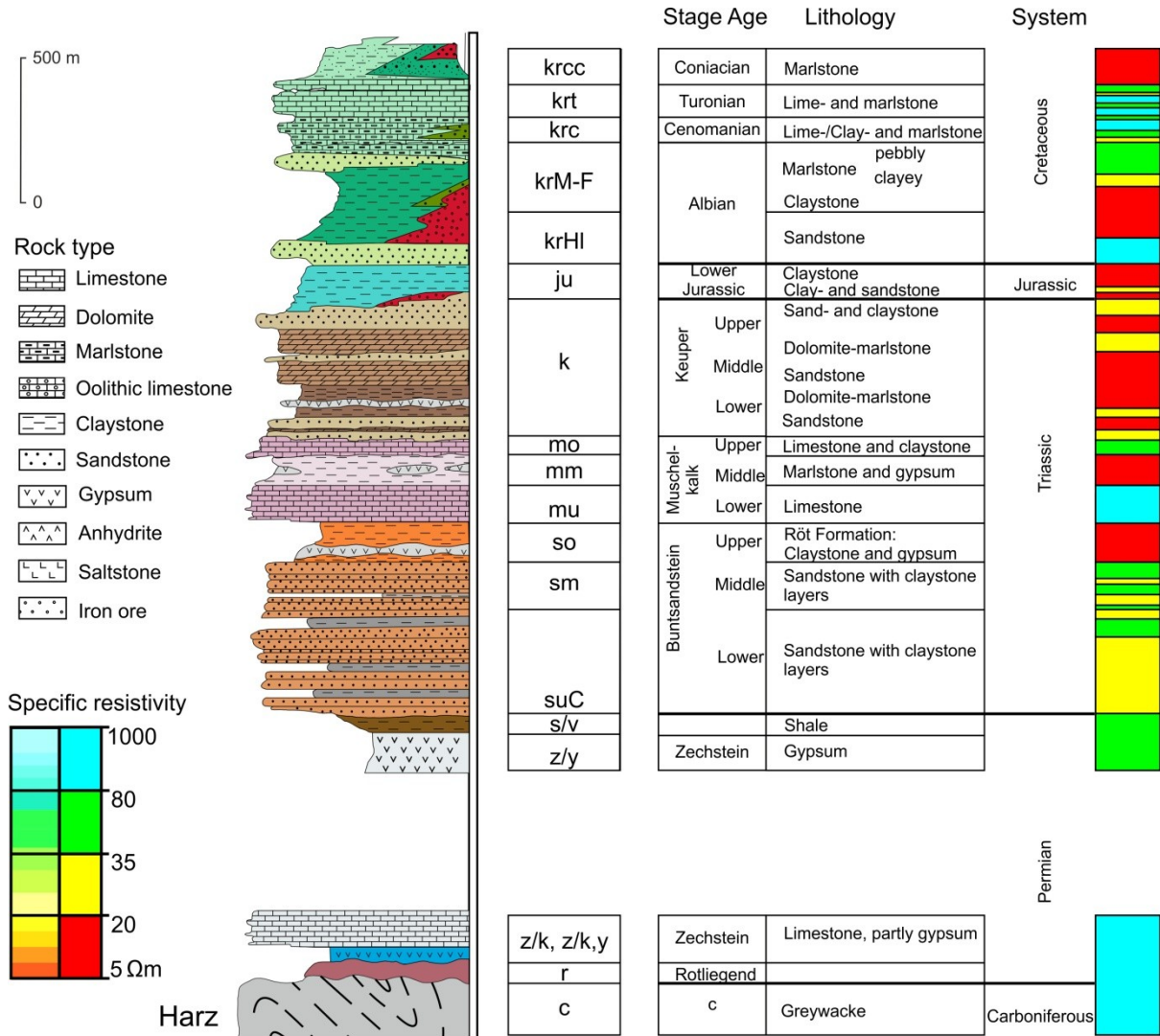
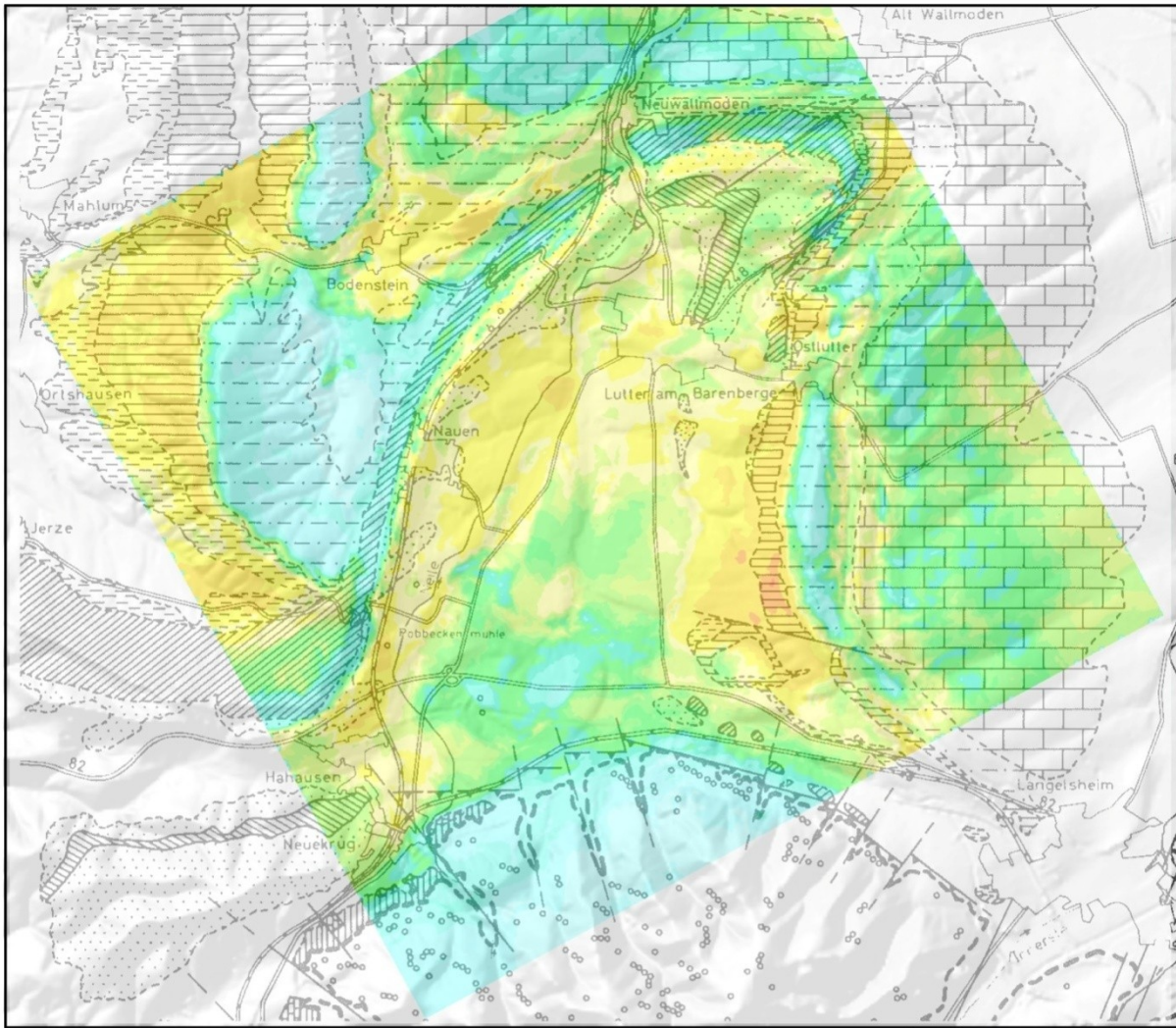


Figure 25: Lithological log of the Subhercynian basin; showing rock types with the corresponding specific resistivity pattern derived from the Lutter anticline study area (modified after Zellmer & Holländer, 1996; Jordan & Siemon, 2002).

4. Results - Case study 2: The Lutter Anticline



modified after Hosseinidust, 1980

Legend

	Pleistocene		Perm (Zechstein)
	Upper Cretaceous		Perm (Rotliegend)
	Lower Cretaceous		Variscan boundary of the Harz Mountains
	Lower Jurassic (Lias)		Fault
	Upper Triassic (Keuper)		Northern Harz Boundary Fault
	Middle Triassic (Muschelkalk)		Spring
	Middle/Lower Triassic (Buntsandstein/Rogenstein)		

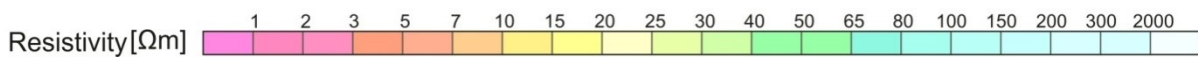


Figure 26: Near-surface resistivity pattern extracted from the 3D subsurface model on top of the geological map of the study area. The geological map is taken from Hosseinidust (1980).

4. Results - Case study 2: The Lutter Anticline

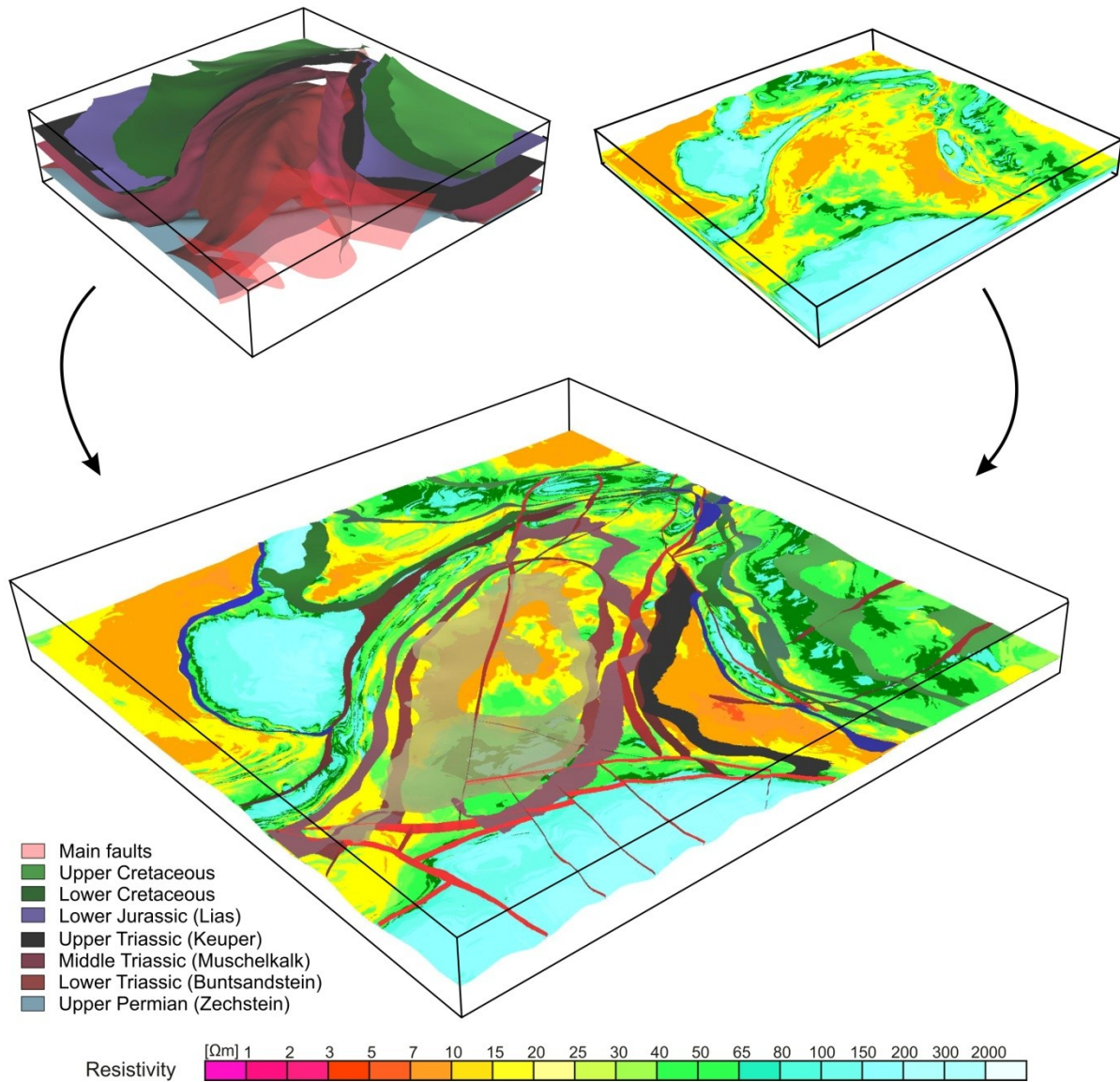


Figure 27: Visualization of the workflow that was performed for the Lutter anticline study. The 3D geological subsurface model (A) was correlated with the resistivity model (B) to construct a common model (C) that allows the comparison of the resistivity pattern with the orientation of the main structural elements.

4.2.2 Outcrop data and interpretation

The results from the outcrop analyses are shown in Figure 4, Figure 28 and Figure 29. The figures show stereographic projections of the tectonic fabrics. From this dataset, two conceptual models were derived (Figure 30), in which the orientation of the major horizontal extensional paleostress is indicated by red arrows and the major horizontal compressional paleostress directions are indicated by blue and black arrows.

The stereographic projections of the tectonic fabrics indicate that the architecture of the Lutter anticline is structurally complex. It is composed of folded Mesozoic rocks with a complex fracture system. Fractures are dominated by three main trends, mainly striking NNE-SSW to NE-SW, WNW-ESE to NW-SE and minor NNW-SSE trends (cf. Figure 4, Figure 28, Figure 29 and Figure 30). The fracture distribution shows significant variation. Fractures of the western limb are dominated by NNE-SSW to NE-SW strike, while fractures of the eastern limb are dominated by WNW-ESE to NW-SE strike. In the northeastern part of the Lutter anticline both fracture systems are equally present. For fracture development in the area of the Lutter anticline, two models are possible (Figure 30). The first one requires one extensional phase and several deformation phases in account and the second one is simpler with only one deformation phase in the Upper Cretaceous.

Model A:

During the Late Triassic the area was affected by NNE-SSW directed extension (Best, 1996; Best & Zirngast, 2002; Lohr et al., 2008) and the WNW-ESE oriented fracture set may have developed as consequence of this tectonic phase (Hosseiniidust, 1980).

In the Early Cretaceous an E-W directed compression affected the CEBS (Lohr et al., 2008). The conjugate WNW-ESE trending shear fractures are likely related to this phase.

During the Late Cretaceous inversion phase related to the Africa-Iberia-Europe convergence, the Lutter anticline was affected by NNE-SSW directed compression and the WNW-ESE trending fractures developed (cf. Hosseiniidust, 1980; Sippel, 2009). During this time, the Harz Boundary Fault was active and the folded Palaeozoic rocks of the Harz Mountains were thrust onto the Mesozoic rocks of the Subhercynian Basin. The stereographic projections indicate that especially the eastern limb of the anticline is characterised by WNW-ESE

4. Results - Case study 2: The Lutter Anticline

trending fractures. During this time, salt movement, accompanied by local subsidence, affected the eastern limb and may have caused normal faulting; the so called Neuwallmoden Fault, which trends NNE-SSW across the Lutter anticline, and probably separates the western from the eastern limb of the Lutter anticline (Hosseinidust, 1980; Sippel, 2009).

In the area of the eastern limb, the regional stress field might have been superimposed by a more local stress state, related to the movements along the Neuwallmoden Fault, thereby leading to a deviation of fracturing direction (Hosseinidust, 1980). A superimposition of differently-directed paleostress east of the Neuwallmoden Fault is also postulated as an explanation for differently-oriented horizontal stylolite (Hosseinidust, 1980). Displacements in the Mesozoic strata in the northeastern part of the Lutter anticline are interpreted as strike-slip faults related to the Late Cretaceous contraction. The formation of the Lutter anticline is supposed to have been strongly controlled by salt movement that deformed its overburden (Carlé, 1938; Hark, 1956). The pronounced radial fracture pattern of the Lutter anticline can be interpreted as a stress field perturbation due to the salt pillow (Stewart, 2006; Brandes et al., 2013; Ahlers et al., 2018).

Model B:

It is possible that only the Late Cretaceous phase of inversion is responsible for fracture development in the area of the Lutter anticline. Both the Neuwallmoden Fault and the Harz Mountains experienced uplift, relative to the Subhercynian Basin (Mohr, 1982). Assuming the reverse movements along the Northern Harz Boundary and the Neuwallmoden Fault to have taken place coevally and considering the perpendicularity of their strike directions, stress states between these closely-located faults would have had to balance divergent kinematics (Hosseinidust, 1980; Sippel, 2009) as can be observed in directional variations in the regional and local fracture trends (Figure 28 and Figure 30).

4. Results - Case study 2: The Lutter Anticline

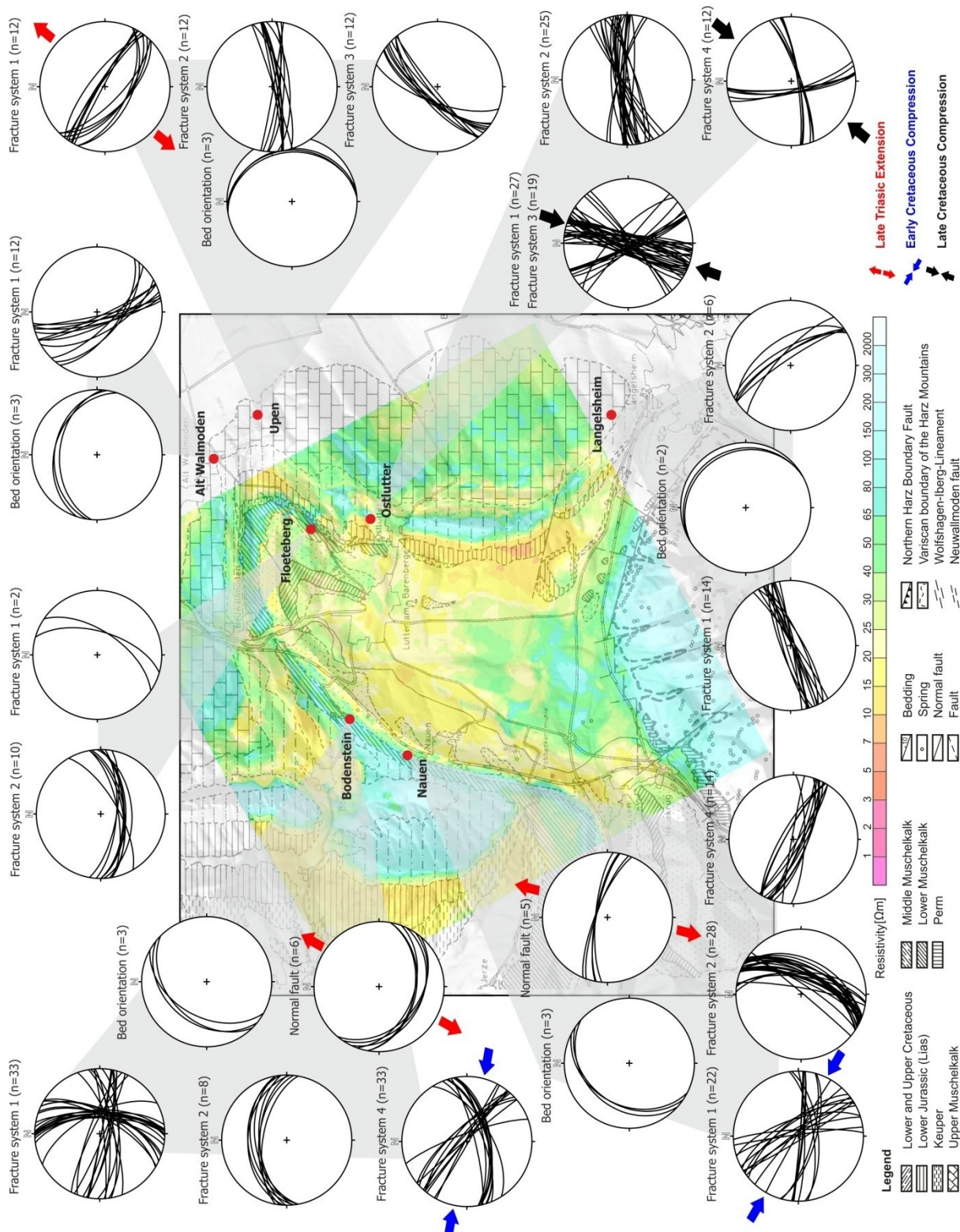


Figure 28: Locations of geological field observations showing orientations of beds, faults and fractures.

4. Results - Case study 2: The Lutter Anticline

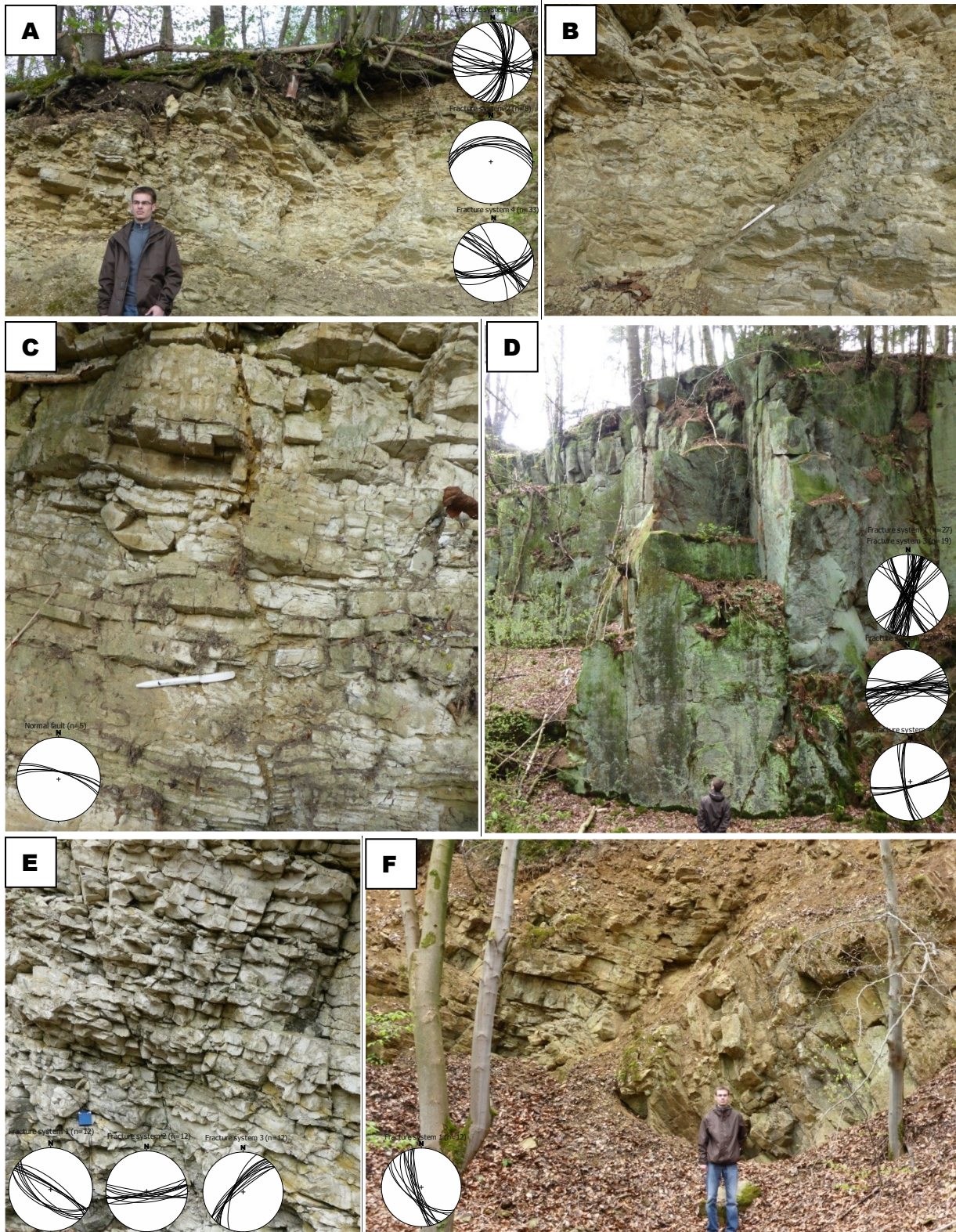


Figure 29: A) and B) Middle Triassic limestone at the western tip of the Lutter anticline with conjugate fracture sets. C) Fault developed in Middle Triassic limestone at Nauen. The displacement of marker beds clearly indicates normal fault kinematics. D) Lower Cretaceous sandstone at Ostlutter. E) Upper Cretaceous limestone with conjugate normal faults at Upen. F) Folded Middle Triassic limestone in an open pit next to the B 248 (Floeteberg).

4. Results - Case study 2: The Lutter Anticline

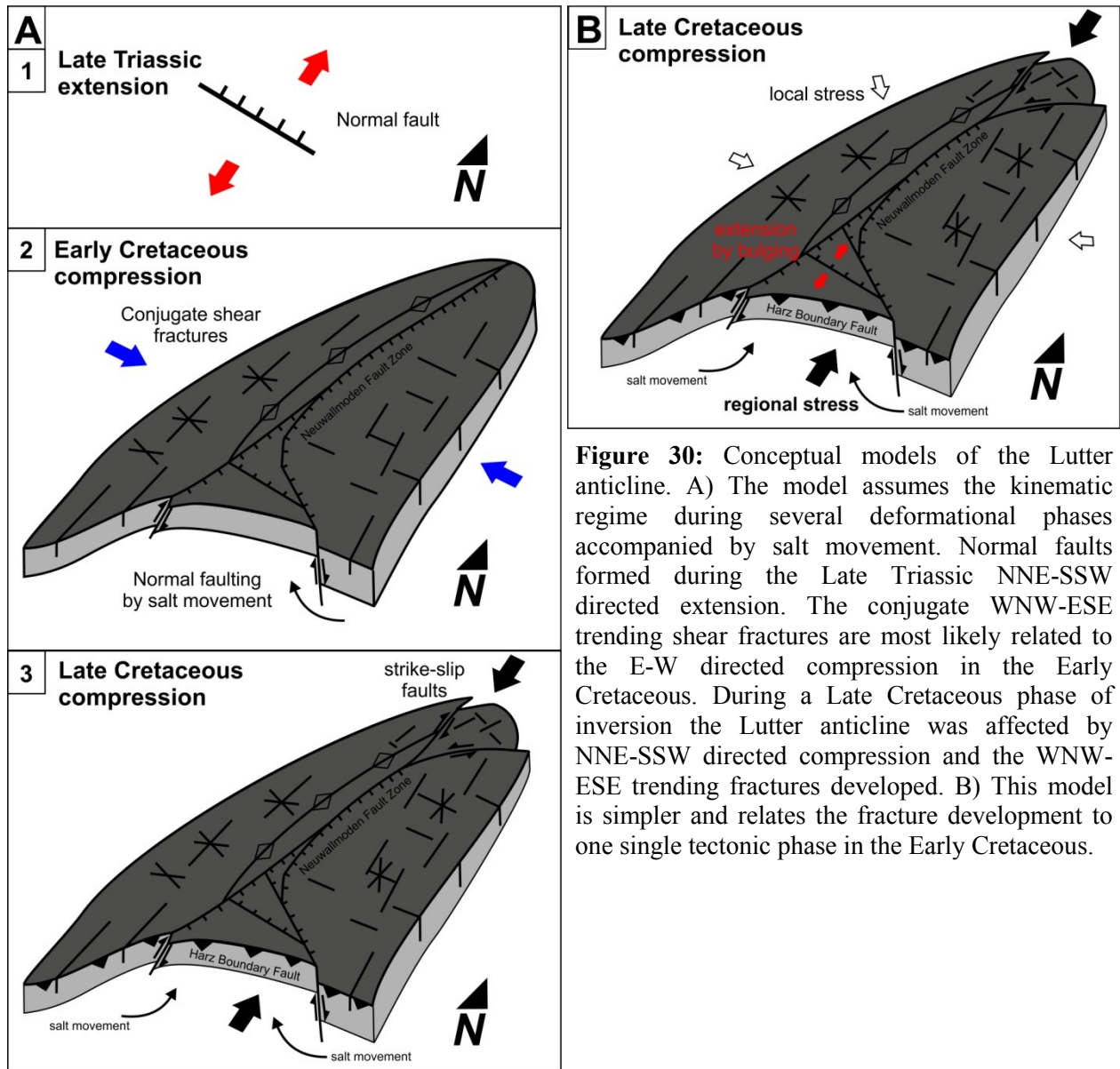


Figure 30: Conceptual models of the Lutter anticline. A) The model assumes the kinematic regime during several deformational phases accompanied by salt movement. Normal faults formed during the Late Triassic NNE-SSW directed extension. The conjugate WNW-ESE trending shear fractures are most likely related to the E-W directed compression in the Early Cretaceous. During a Late Cretaceous phase of inversion the Lutter anticline was affected by NNE-SSW directed compression and the WNW-ESE trending fractures developed. B) This model is simpler and relates the fracture development to one single tectonic phase in the Early Cretaceous.

4.2.3 Directional geometry analysis of the subtle resistivity signature - correlation with outcrop data

The processed data shows resistivity trends, derived from resistivity grid data, which reflect the fracture orientation that was measured in outcrops. The maximum curvature application is able to find orientation and continuity trends within the resistivity grid data and to compute an azimuth value for each cell. In Figure 31, the directional trends are summarized in a histogram as the regional azimuths of resistivity.

The mapped resistivity trends displayed in Figure 32 and Figure 33 consistently show dominant orientations, one aligned along a NNE-SSW to NE-SW axis and another aligned along WNW-ESE to NNW-SSE axis trends (cf. Figure 26, Figure 32, Figure 33 and Figure 34). One set is parallel to the trend of the anticline axis; the other set is roughly perpendicular to the fold axis.

The NNE/NE trends also consistently exhibit the clearest and longest features, as can be seen on the resistivity map, indicating more continuous, larger and elongated features (Figure 32). The spatial distribution of the NNE-SSW structural trends varies across the Lutter anticline. The major NNE-trending structures are restricted to the central region and the flanking areas of the Lutter anticline, whereas to the north they are dominated by NE-trending structures (Figure 32, Figure 33 and Figure 34). Similar trends can also be observed in fracture orientation of the outcrop data (cf. Figure 4 and Figure 28).

The WNW-ESE to NW-SE trend is evident, roughly orthogonal to the NNE/NE-trend and more localized on the eastern limb of the Lutter anticline. Additionally, the NW-SE directional trends show some diversification and show scattered azimuths around the maxima of 106 and 286 degrees. These directional variations can be also observed in the stereographic projections of fracture sets measured in the outcrops.

Across the Lutter anticline, a system of more continuous, larger elongated features is present. In the southern areas, these features are more scattered with a diffuse orientation. Northward, the features trend N-S and in the northeastern part they show a NE-SW direction. These features probably indicate the Neuwallmoden fault system, interpreted to separate the western from the eastern limb (Hosseindust, 1980). Resistivity trends apparent on the eastern limb and especially in the northern part of the Lutter anticline are much more variable and

segmented, compared to those on the western limb. This is interpreted to indicate strike-slip faults related to the upper Cretaceous contractional tectonic phase.

The electromagnetic anomalies in the study area show a certain degree of local variability. This correlates with the pronounced radial fracture pattern of the northeastern part of the Lutter structure (Figure 4 and Figure 34), which can be interpreted as a result of stress field perturbation related to the salt structure (cf. Brandes et al., 2013).

Consequently, the derived trends do not entirely reflect the fracture pattern. However, the dominant trends observed in the resistivity pattern are aligned along NNE-SSW and WNW-SSE axes, comparable to the outcrop observations. Both major trends in the resistivity pattern appear to be offset, locally displaced.

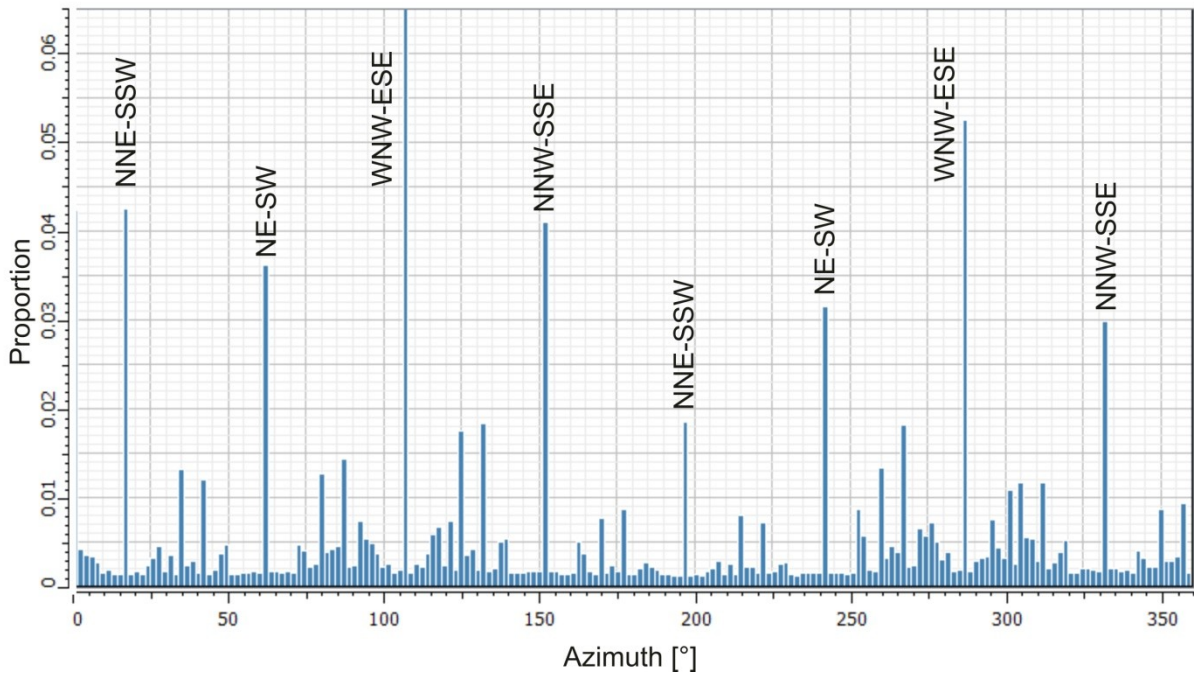


Figure 31: Directional trends summarizing the regional azimuths of resistivity.

4.2.4 Geological interpretation

The Lutter anticline study demonstrates that resistivity subsurface models are suitable for a structural analysis. The 3D model of the Lutter anticline visualizes the complex geometry of the anticline, together with a series of faults and fractures of different dimensions. The anticline plunges NNE to NE and is composed of Mesozoic rocks that host different fracture sets and faults. The analysis of the structural elements is based on outcrop and resistivity data and indicates that there are three dominant fracture orientations with a NNE-SSW to NE-SW,

4. Results - Case study 2: The Lutter Anticline

WNW-ESE to NW-SE and a NNW-SSE trend (Figure 31, Figure 32, Figure 33 and Figure 34).

The NNE-SSW and WNW-ESE trends in the resistivity pattern correlate with fractures in the subsurface (Figure 33 and Figure 34). This is supported by the observation of offsets in the resistivity pattern and trends of maximum curvature, based on the analysis of resistivity grid data.

The data can be interpreted in two ways: the first model that relates the different fractures to individual deformation phases that affected the CEBS in Triassic, Early and Late Cretaceous times and second model that can explain the fracture evolution with one tectonic phase, namely the Late Cretaceous inversion.

The NNE-SSW trending fractures follow the orientation of major basement faults formed during the extensional tectonics in the Middle to Late Triassic. Resistivity features in the central and northern part of the Lutter anticline probably indicate major faults or fault zones related to the Neuwallmoden Fault, as also assumed by Hosseinidust (1980) and Mohr (1982).

The WNW-ESE trending fractures in the Mesozoic rocks are interpreted to have formed during tectonic inversion, when the Harz Mountains were thrust northwards (Brandes et al., 2013) and ongoing salt tectonics that occurred during the Late Cretaceous to Early Paleogene, driven by the Africa-Iberia-Europe convergence (Maystrenko et al., 2005a; Kley & Voigt, 2008).

The northern part of the Lutter anticline is characterized by an eastward change in the resistivity pattern, as seen in the fracture orientation of outcrop data, probably indicating a more intense deformation in the vicinity of the northern Harz Boundary Fault.

The WNW-ESE trending pattern interferes with the NNE-SSW trending pattern within the Lutter anticline (Figure 33). This suggests that NE-trending strike-slip faulting has especially affected the eastern limb of the Lutter anticline during the formation of the Harz Mountain thrusting in the Late Cretaceous.

The observed trends in resistivity also allow the coevally fracture development during the Late Cretaceous contractional phase to be shown.

4. Results - Case study 2: The Lutter Anticline

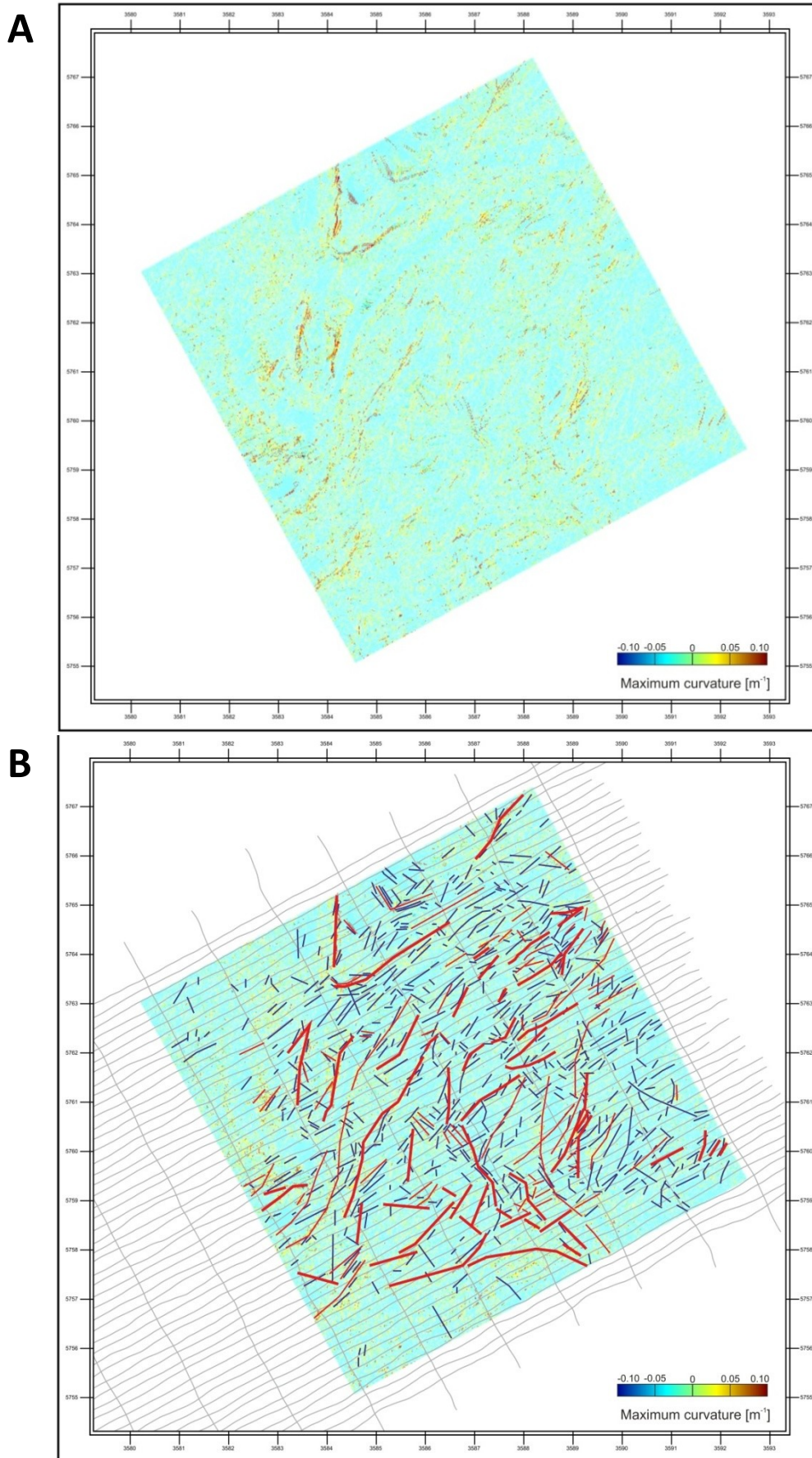


Figure 32: A) 3D resistivity grid colour coded by maximum curvature. B) Interpreted major fracture zones in red colour and minor fracture zones in blue colour determined by maximum curvature amplitude. Flight lines of AEM are coloured light grey.

4. Results - Case study 2: The Lutter Anticline

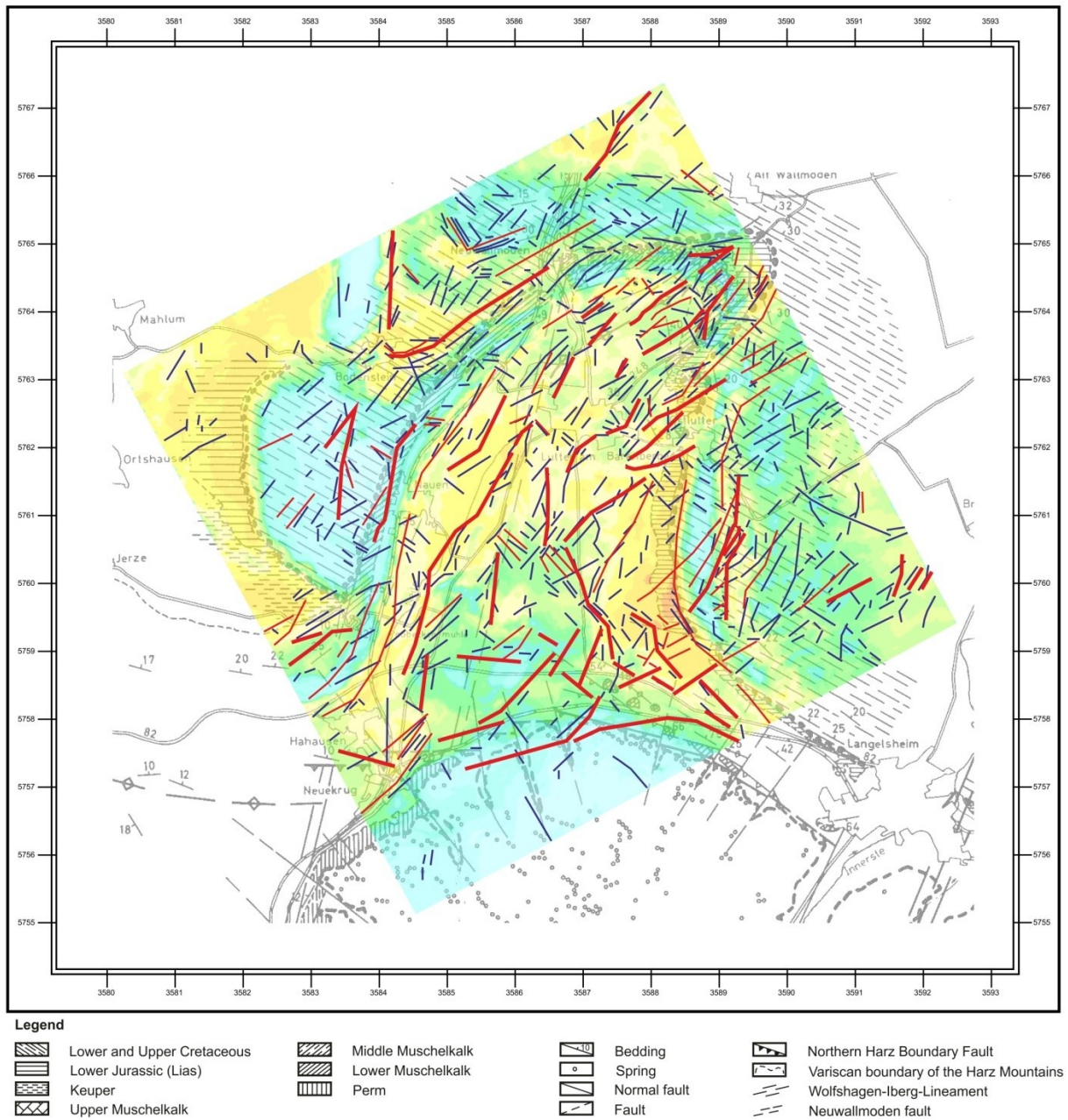


Figure 33: Interpreted orientation of fracture zones based on mapped trends of maximum curvature application together with the geology and resistivity.

4. Results - Case study 2: The Lutter Anticline

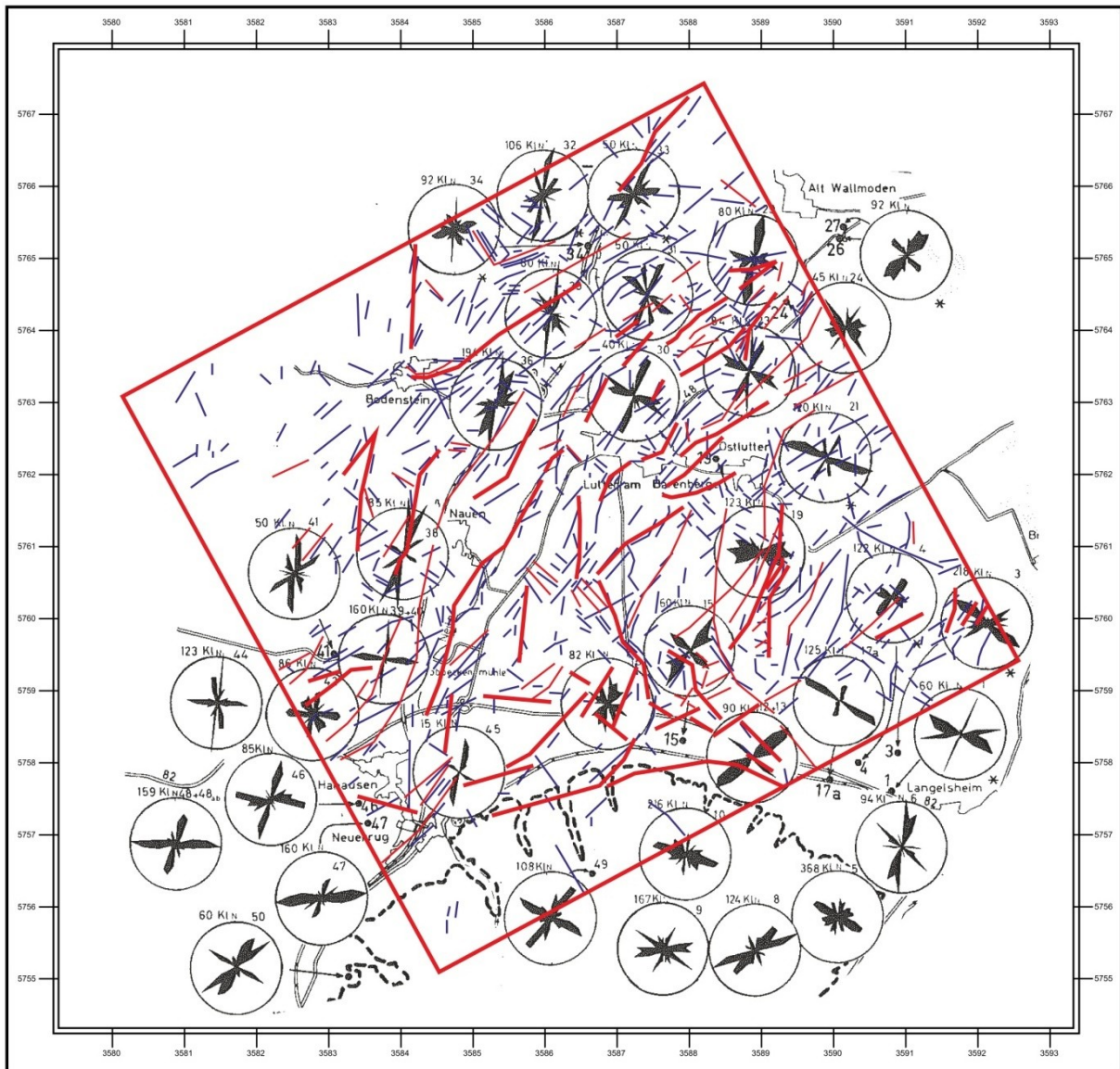


Figure 34: Interpreted major fracture zones shown in red and minor fracture zones in blue, as determined by maximum curvature amplitude compared to fracture orientations in the Lutter anticline taken from Hosseinidust (1980).

5. Discussion

The thesis results show that AEM data provide excellent opportunities to map the subsurface geology, as also demonstrated by, e.g. Newman et al. (1986), Jordan & Siemon (2002), Danielsen et al. (2003), Jørgensen et al. (2003b, 2013), Auken & Christiansen (2004), Auken et al. (2008), Viezzoli et al. (2008), Bosch et al. (2009), Christensen et al. (2009), Gunnink et al. (2012), Klimke et al. (2013) and Slapansky et al. (2017). A good relationship between resistivity values and lithology enables the three-dimensional imaging of the subsurface architecture. This allows a hitherto unseen amount of geological detail, using AEM data in areas with low geological knowledge. This approach provides advanced 3D geological models of the study areas with new geological insights. Although the presented approach, especially in the Cuxhaven case study, is more time consuming than an automated approach that relies on statistics-based methods (Bosch et al., 2009; Gunnink et al., 2012), the end result compensates for the limitations of the AEM method.

Geological and geophysical models and their interpretations contain limitations and uncertainties resulting from limitations in the input information (Ross et al., 2005). Several studies focussed on the analysis of such limitations and uncertainties in order to minimise risk, e.g. exploration risks (Bárdossy & Fodor, 2001; Pryet et al., 2011; Wellmann & Regenauer-Lieb, 2012; Jørgensen et al., 2013). Uncertainties and limitations in the integrated interpretation of AEM and ground-based data are mainly caused by the restricted availability and limited vertical and lateral resolution of data (e.g. boreholes, seismic sections, airborne surveys); modelling errors caused by a misinterpretation of geophysical, lithological and hydrogeological properties; anthropogenic noise effects; missing software interoperability (Mann, 1993; Bárdossy & Fodor, 2001; Ross et al., 2005; Pryet et al., 2011) and irreducible, input geology-related, uncertainty. In general, there are several limitations in the interpretation caused by the applied AEM systems and the chosen data analysis.

The penetration depth and resolution of AEM systems are controlled by lithology and its conductivity. The penetration depth is limited by the used airborne technique, and all airborne systems are subject to decreasing resolution capability with depth, and require an increasing thickness/depth ratio for the detection of varying depositional units (Jørgensen et al., 2003b, 2005; Høyer et al., 2011). Due to the wide range of lithologies, a significant uncertainty remains in the final interpretation of the resistivity pattern. Hence, thin-bedded sedimentary units are only resolved if their corresponding conductance, i.e. the ratio of thickness and

resistivity, is sufficiently high. Otherwise, they are merged into a single unit with an average resistivity (Jørgensen et al., 2003b, 2005), which results in a limited resistivity resolution. The limitations in the lateral and vertical resolution can lead to incorrect interpretations of thin-bedded sand/mud couplets, smaller-scale architectural elements and bounding surfaces, as has also been shown by, e.g. Jørgensen et al. (2003a, 2005), Viezzoli et al. (2008), Christensen et al. (2009) and Klimke et al. (2013). This problem is distinctly seen in the study areas in the Pleistocene tunnel-valley and Late Miocene incised valley, as also in the Mesozoic rocks of the Lutter anticline.

A geostatistical approach was used to analyse and interpolate the 1D AEM inversion results to create a continuous 3D resistivity subsurface grid. Ordinary kriging was used and in contrast to Pryet et al. (2011), the layered approach used in the 1D inversion of AEM data was discarded, leading to a smoothing effect between previously-defined layer boundaries. The advantage of this method is that the kriging algorithm indicates the most likely resistivity value at each grid cell. The result is an effectively smoothed resistivity grid, leading to a significantly improved geological interpretation of continuous lithofacies. However, the loss of heterogeneity that is probably observed in the subsurface by AEM has to be taken into account. If the aim is to generate fluid-flow models, it is important to preserve the porosity and permeability of varying lithologies, as these strongly determine fluid-flow behaviour through porous media (e.g. Koltermann & Gorelick, 1996; Janszen, 2012). Therefore, it is preferred to base fluid-flow simulations on grids that are interpolated using algorithms that are able to preserve the heterogeneity such as modified kriging methods, such as the sequential indicator simulation used by Venteris (2007), Bosch et al. (2009) and Janszen (2012).

For this thesis, only 1D AEM inversion datasets (from 2002 for Cuxhaven and from 2000 for Lutter anticline case study) were available, in which noise effects were not considerably minimized, as commonly applied for new datasets (e.g. Tølbøll, 2007; Siemon et al., 2011). In the case of the study areas, anthropogenic noise effects cause unrealistic low resistive oscillations, which conically increase downwards and thus can be easily identified in the 3D model. However, noise effects of anthropogenic structures and soundings in the airborne electromagnetic data can hinder a proper geological interpretation, e.g. the airport Cuxhaven/Nordholz located in the northwest of the Cuxhaven study area.

A common limitation of the presented thesis is the degree of subjectivity that causes uncertainties, which are difficult to evaluate. To test the reliability of the 3D geological subsurface model and to evaluate related uncertainties, a new approach was developed based

on synthetic AEM data, which was derived from the geological model of Cuxhaven. The comparison between the corresponding apparent resistivity images of the 3D geological subsurface model and AEM field measurements leads to the identification of uncertainties and limitations of 1D AEM inversion and vice versa. Results of such analyses will offer the advantage of using a-priori information to improve the inversion of AEM data, comparable to investigations made by, e.g. Zhdanov (2010) and Gunnink et al. (2012).

Study area of the Cuxhaven tunnel valley

For the Cuxhaven tunnel valley, the incorporation of the AEM resistivity model and the seismic reflection data for mapping the topography of the Pleistocene base allowed to define critical features of the geological system. The high resolution of the seismic reflection data allowed to compensate for variations in the electrical resistivity of the subsurface that resulted from both real changes in lithology, and/or resolution limitations of the AEM data and inversion. Nevertheless, in most areas, valley bottoms are identified as occurring below the AEM depth of investigation. Therefore borehole and seismic data provide depth control and the lateral variation in resistivity shows the path of the tunnel valley.

Despite the high AEM data density, the seismic sections are still localized and the accuracy of control lines and structural lithological mapping likely decreases with distance from the seismic sections. If the resistivity structure of the valley changes significantly between seismic sections, the AEM-based control line may not accurately represent a unique morphological feature along its entire path. The limited separability of electrical resistivity for the sediments (Oldenborger et al., 2014; Logan et al., 2015) complicates the identification of morphological features. To reduce this, cross validation between resistivity and lithological units was performed. But especially the Saalian till at 20 m depth, with a thickness between 5-10 m, and a wide resistivity range (cf. Figure 23) could not be differentiated from the surrounding lithology and is beyond the possible AEM resolution. Also the Pleistocene tunnel-valley margins and the Late Miocene incised-valley margin could not be detected clearly because of a low resistivity contrast between Pliocene and Miocene deposits below.

Nevertheless, the spatial resolution of tunnel valley morphology, as captured by the presented geological- and geophysical-based subsurface mapping provides information that could not have realistically been obtained from a drilling program. Even an extensive drilling program could not provide the spatial resolution, necessary to define the lateral extents, maximum

depths and boundaries of the deep incised tunnel valley. Given their dimensions, drill-hole spacing of approximately some tens to hundreds of meters would be necessary to define the tunnel valley architecture. Clearly the geophysical data, along with bedrock mapping of the tunnel valley network, has generated a more refined and complete picture and in-depth understanding of tunnel valley geometry and history (Pugin et al., 2014; Oldenborger et al., 2016).

Study area of the Lutter anticline

In the study area of the Lutter anticline, the results enable a much better construction of the subsurface structure by the resistivity classification of lithologies and the detection of fault and fracture systems in a three-dimensional environment. Due to the restricted resolution of AEM data, thin, bedded mud-, lime-, sand- or marlstones within the Mesozoic strata could not be differentiated. Nevertheless, the workflows developed in this study provide a new approach for predictive mapping of bedding and fracture orientation in unexplored terrain. The near-surface fractures are likely filled with water. Together with variations in lithology, this can result in local resistivity changes and serves as a possible explanation why the fractures and fracture orientations can be visualize with the AEM method.

The AEM surveys were acquired in a southwest-northeast direction, which could result in artefacts that can be misinterpreted as fracture patterns. Nevertheless, the distribution of the resistivity trends reflects the main orientations of fractures in the Lutter anticline. The accuracy of positioning is not high enough to locate all the individual fractures, but the main strength of this approach reveals the prevalent fracture orientations.

As curvature is closely related to the second derivative of the surface, its quality is very susceptible to the level of noise contamination (Roberts, 2001). There are often many sources for this noise on mapped surface, e. g. geological processing, acquisition and the horizon auto tracking process. Filtering the noise using iterative median filtering (Gallagher & Wise, 1981) and weighted average filtering, is often a compromise between trying to remove noise effects, without reducing the resolution and obscuring too much of the detail. Artefacts that result from the AEM data acquisition procedure (e.g., the flight direction), processing and the applied 3D interpolation algorithm (e.g. preferred angles of the geostatistical analysis) can be eliminated with knowledge of the local rock properties and by mapping the fractures in the field. Furthermore, many of the electromagnetic anomalies in the populated Harz foreland

5. Discussion

region are caused by noise effects of settlements (e.g. houses, roads, power lines, rivers, drainage systems etc.) that may slightly disturb the interpretation of the resistivity pattern and the automated method. These anthropogenic induced anomalies could be identified and eliminated by a comparison of the AEM images with topographic maps. This study demonstrates the potential of the AEM method in mapping near-surface structural elements. To minimise uncertainties and to calibrate the resulting models, a field campaign for mapping the fracture distribution and orientation based on outcrops is highly recommended.

6. Conclusions

Based on airborne electromagnetic data, this thesis provides a significant improvement in the geological interpretation of the Cuxhaven tunnel valley and its Neogene host sediments and the Lutter anticline by the predictive mapping of lithologies, and the detection of fault and fracture systems in a three-dimensional environment.

Resistivity data derived from AEM surveys can provide a fast and efficient overview mapping of the shallow subsurface geology. A methodology for the interpretation, analysis and imaging of resistivity data gained by AEM surveys, based on 3D modelling approaches, was developed. One-dimensional HFEM and HTEM inversion results were used and a 3D resistivity gridding procedure based on geostatistical analyses and interpolation techniques were applied to create continuous resistivity models of the subsurface. Subsequently, results of seismic facies and borehole lithology analysis were integrated to construct a combined 3D geological subsurface model and to reduce uncertainties. This approach allows for an improved interpretation of AEM data and imaging of the 3D subsurface architecture, if the relationship between lithology and resistivity is known and the site is only slightly influenced by noise (e.g. infrastructural networks, settlements).

The 3D resistivity grids in the Cuxhaven case study clearly allow to discriminate between different lithologies and enable the detection of Cenozoic sequence boundaries and larger-scale architectural elements, such as incised valleys and subglacial tunnel valleys. Variations in the resistivity pattern allowed the detection of individual delta lobes and smaller-scale channels as well as lateral and vertical grain-size variation. In the Neogene succession, the low resistive pattern can be correlated with Tortonian and Messinian marine clays. The lowest values probably correspond with the zone of maximum flooding. Seismic interpretation leads to the conclusion that, at the end of the Miocene, an incised valley formed as a response to a major sea-level fall. It subsequently became filled with Pliocene delta deposits, probably indicating the paleo-course of the River Weser or Elbe. The resistivity models clearly image the outline of the Pleistocene tunnel valleys. The unconsolidated fill of the Late Miocene to Pliocene incised valley probably formed a preferred pathway for the Pleistocene meltwater flows, favouring the incision of a subglacial tunnel valley. Based on the 3D HFEM resistivity grid, the fills of the tunnel valleys could be imaged in much more detail in comparison to previously-published descriptions, based on the 2D seismic sections and 2D AEM profiles

6. Conclusions

and maps. The applied approaches and results show a reliable methodology, especially for future investigation of similar geological settings.

The Lutter case study shows that 3D resistivity data based on AEM surveys also can provide valuable information about the distributions of different rock types in the near subsurface and allows the interpretation of faults and fracture systems. The acquisition of high-quality geophysical data and 3D modelling allowed to analyze structural elements developed in the Lutter anticline. The 3D resistivity grid clearly allows to distinguish between Palaeozoic and Mesozoic mudstones and siltstones, which are represented by low resistivity values and Mesozoic limestones and sandstones characterized by high resistivity values. Major fault and fracture zones were detected by disruptions and offsets in the resistivity pattern. Stereographic projections of tectonic fabrics from outcrop data show that the structure of the Lutter anticline is complex. The fracture development in the area of the Lutter anticline can be explained by two possible models. The model shown in Figure 30A relates the different structural elements to three individual tectonic phases that affected the CEBS in the Triassic, Early Cretaceous and Late Cretaceous. An alternative model (Figure 30B) assumes that all observed structural elements evolved in one tectonic phase (the Late Cretaceous inversion phase). The fractures show three main orientations: NNE-SSW to NE-SW, WNW-ESE to NW-SE and NNW-SSE.

This study shows that the predominant fault and fracture directions are clearly detectable with a simple curvature analysis of the interpolated 3D resistivity pattern based on AEM 1D inversion datasets.

The AEM data allows to detect and map the near-surface fractures developed in sedimentary rocks and can serve as a fast and reliable method for a first-order fracture analysis. Together with outcrop datasets, the AEM results can serve, e.g., as input parameters for regional studies on fractured reservoirs.

This thesis presents a simple methodology for the interpretation, analysis and visualization of airborne electromagnetics, based on 3D modelling approaches. I used 1D AEM inversion results and applied 3D resistivity gridding procedure based on geostatistical analyses and interpolation techniques to create continuous 3D resistivity grids. Subsequently, the 3D resistivity grids are correlated to lithology to construct an improved geological 3D subsurface model.

The results indicate that a 3D resistivity grid can serve as a basis for constructing the subsurface architecture, with the premise that AEM resistivity data can be correlated to

6. Conclusions

lithology and are only slightly influenced by noise effects (e.g. infrastructural networks, settlements). The model reliability is limited by data quantity, quality, and the efficiency of their interaction, and can be improved by the quantification of uncertainties related to processing and correlation of datasets.

The integrated workflow results in the detection of Palaeozoic, Mesozoic and Cenozoic lithologies and the detection of fault and fracture systems. The results show the structural configuration is complex. Nevertheless, the predominant fault and fracture directions are clearly detectable with simple application of curvature of interpolated 3D resistivity pattern based on AEM 1D inversion datasets. It is a methodology with the potential to predict the orientation of tectonic fabrics and hence to characterize fluid-flow behavior.

The 3D modelling approach, in connection with the geometry application, for detection of fault and fracture systems is a good tool also to improve visualisation of possible migration pathways. Some of the presented results in this thesis may constitute targets for further detailed investigation through data acquisition, handling, and methodologies for interpretation.

7. References

- Ahlers, S., Hergert, T., Henk, A., 2018. Numerical modelling of salt-related stress decoupling in sedimentary basins – Motivated by observational data from the North German Basin. *Geosciences* 9 (1).
- Allwardt P.F., Bellahsen N., Pollard D.D., 2007. Curvature and fracturing based on global positioning system data collected at the Sheep Mountain anticline, Wyoming. *Geosphere* 3: 408-421.
- Anell, I., Thybo, H., Rasmussen, E., 2012. A synthesis of Cenozoic sedimentation in the North Sea. *Basin Research* 24: 154-179.
- Archie, G.E., 1942. The electrical resistivity log as an aid in determining some reservoir characteristics. *Trans AIME* 146: 54-62.
- Auken, E., Christiansen, A.V., 2004. Layered and laterally constrained 2D inversion of resistivity data. *Geophysics* 69 (3): 752-761.
- Auken, E., Christiansen, A.V., Jacobsen, L.H., Sorensen, K.I., 2008. A resolution study of buried valleys using laterally constrained inversion of TEM data. *Journal of Applied Geophysics* 65 (1): 10-20.
- Bachmann, G., Hoffmann, N., 1997. Development of the Rotliegend basin in Northern Germany. *Geologisches Jahrbuch* 103: 9-31.
- Baldschuhn, R., Frisch, U., Kockel, F. (Eds.), 1996. *Geotektonischer Atlas von NW-Deutschland 1 : 300000*. Bundesanstalt für Geowissenschaften und Rohstoffe, Hannover.
- Baldschuhn, R., Binot, F., Fleig, S., Kockel, F., 2001. *Geotektonischer Atlas von Nordwestdeutschland und dem deutschen Nordsee-Sektor*. *Geologisches Jahrbuch* A153: 3-95.
- Bárdossy, G., Fodor, J., 2001. Traditional and new ways to handle uncertainty in geology. *Natural Resources Research* 10 (3): 179-187.

7. References

- Bayer, U., Scheck, M., Rabbel, W., Krawczyk, C.M., Gftze, H.-J., Stiller, M., Beilecke, Th., Marotta, A.M., Barrio-Alvers, L., Kuder, J., 1999. An integrated study of the NE German Basin. *Tectonophysics* 314: 285-307.
- Beaudoin, N., Bellahsen, N., Lacombe, O., Emmanuel, L., 2011. Fracture controlled paleohydrogeology in a basement-cored fault-related fold: Sheep Mountain Anticline, Wyoming, United States. *Geochemistry Geophysics Geosystems* 12 (6).
- Bedrosian, P.A., Schamper, C., Auken, E., 2016. A comparison of helicopter-borne electromagnetic systems for hydrogeologic studies. *Geophysical Prospecting* 64: 192-215.
- Benek, R., Kramer, W., McCann, T., Scheck, M., Negendank, J.F.W., Korich, D., Huebscher, H., Bayer, U., 1996. Permo-Carboniferous magmatism of the NE German basin. *Tectonophysics* 266: 379-404.
- Besenecker, H., 1976. Bohrdatenbank Niedersachsen, Bohr-ID: 3028HY0304, Landesamt für Bergbau, Energie und Geologie (LBEG), Hannover.
- Best, G., 1996. Floßtektonik in Nordwestdeutschland: Erste Ergebnisse reflexionsseismischer Untersuchungen an der Salzstruktur "Oberes Allertal". *Zeitschrift der deutschen Gesellschaft für Geowissenschaften* 147, 455-464.
- Best, G., Kockel, F., Schoeneich, H., 1983. Geological history of the southern Horngraben. *Geologie en Mijnbouw* 62: 25-33.
- Best, G., Zirngast, M., 2002. Die strukturelle Entwicklung der exhumierten Salzstruktur "Oberes Allertal". *Geologisches Jahrbuch, Sonderheft A1*, 142, 100.
- Betz, D., Führer, F., Greiner, G., Plein, E., 1987. Evolution of the Lower Saxony Basin. *Tectonophysics* 137: 127-170.
- Blindow, N., Balke, J., 2005. GPR-Messungen zur Bestimmung der Grundwasseroberfläche im Bereich des Geestrückens südlich von Cuxhaven. *Zeitschrift für Angewandte Geologie* 1: 39-44.
- Bosch, J.H.A., Bakker, M.A.J., Gunnink, J.L., Paap, B.F., 2009. Airborne electromagnetic measurements as basis for a 3D geological model of an Elsterian incision. *Zeitschrift der deutschen Gesellschaft für Geowissenschaften* 160 (3): 249-258.

7. References

- Böse, M., Lüthgens, C., Lee, J. R. & J. Rose, 2012: Quaternary glaciations of northern Europe. *Quaternary Science Reviews* 44: 1-25.
- Brandes, C., Pollok, L., Schmidt, C., Riegel, W., Wilde, V., Winsemann, J., 2012. Basin modelling of a lignite-bearing salt rim syncline: insights into rim syncline evolution and salt diapirism in NW Germany. *Basin Research* 24: 699-716.
- Brandes, C., Schmidt, C., Tanner, D.C., Winsemann, J., 2013. Paleostress pattern and salt tectonics within a developing foreland basin (northwestern Subhercynian Basin, northern Germany). *International Journal of Earth Sciences* 102: 2239-2254.
- Brandes, C., Steffen, H., Steffen R. and Wu, P., 2015. Intraplate seismicity in northern Central Europe is induced by the last glaciation. *Geology* 43: 611-614.
- Brink, H.J., Dürschner, H. & Trappe, H., 1992. Some aspects of the late and post-Variscan development of the Northwestern German Basin. *Tectonophysics* 207: 65-95.
- Burschil, T., Wiederhold, H., Auken, E., 2012a. Seismic results as a-priori knowledge for airborne TEM data inversion - A case study. *Journal of Applied Geophysics* 80: 121-128.
- Burschil, T., Scheer, W., Kirsch, R., Wiederhold, H., 2012b. Compiling geophysical and geological information into a 3-D model of the glacially-affected island of Föhr. *Hydrology and Earth System Sciences* 16: 3485-3498.
- BurVal Working Group, 2009. Buried Quaternary valleys - a geophysical approach. *Zeitschrift der deutschen Gesellschaft für Geowissenschaften* 160 (3): 237-247.
- Cameron, T.D.J., Buat, J., Mesdag, C.S., 1993. High resolution seismic profile through a Late Cenozoic delta complex in the southern North Sea. *Marine and Petroleum Geology* 10: 591-599.
- Carlé, W., 1938. Die saxonische Tektonik westlich und nordwestlich des Harzes (Gittelder Graben und Lutterer Sattel). *Geotektonische Forschungen* 3: 33-72.
- Caspers, G., Jordan, H., Merkt, J., Meyer, K.-D., Müller, H., Streif, H., 1995. III. Niedersachsen. In: Benda, L. (ed.): *Das Quartär Deutschlands*. Gebrüder Bornträger (Berlin): 23-58.

7. References

- Catuneanu, O., 2002. Sequence stratigraphy of clastic systems: concepts, merits, and pitfalls. *Journal of African Earth Sciences* 35: 1-43.
- Catuneanu, O., Galloway, W.E., Kendall, C.G.St.C., Miall, A.D., Posamentier, H.W., Strasser, A., Tucker, M.E., 2011. Sequence Stratigraphy: Methodology and Nomenclature. *Newsletters on Stratigraphy* 44 (3): 173-245.
- Caumon, G., Collon-Drouaillet, P., Le Carlier de Veslud, C., Viseur, S., Sausse, J., 2009. Surface-Based 3D Modeling of Geological Structure. *Mathematical Geosciences* 41 (8), 927-945.
- Christensen, N.K., Reid, J.E., Halkjær, M., 2009. Fast, laterally smooth inversion of airborne time-domain electromagnetic data. *Near Surface Geophysics* 7: 599-612.
- Christensen, N.K., Minsley, B.J., Christensen, S., 2017. Generation of 3-D hydrostratigraphic zones from dense airborne electromagnetic data to assess groundwater model prediction error. *Water Resources Research* 53 (2): 1019-1038.
- Dalrymple, R.W., Zaitlin, B.A., Boyd, R., 1992. Estuarine facies models: conceptual basis and stratigraphic implications. *Journal of Sedimentary Petrology* 62: 1130-1146.
- Daniels, C.H. von, Gramann, F., 1988. The Federal Republic of Germany (Lower Rhine Embayment, Lower Saxony, Schleswig-Holstein). *Geologisches Jahrbuch A100*: 201-208.
- Danielsen, J.E., Auken, E., Jørgensen, F., Søndergård, V., Sørensen, K.I., 2003. The application of the transient electromagnetic method in hydrogeological surveys. *Journal of Applied Geophysics* 53: 181-198.
- de Louw, P.G.B., Eeman, S., Siemon, B., Voortman, B.R., Gunnink, J., van Baaren, E.S., Oude Essink, G.H.P., 2011. Shallow rainwater lenses in deltaic areas with saline seepage. *Hydrology Earth System Sciences* 15: 3659-3678.
- DEKORP-BASIN RESEARCH-GROUP: Bachmann, G.H., Bayer, U., Dürbaum, H.-J., Hoffmann, N., Krawczyk, C.M., Lück, E., McCann, T., Meissner, R., Meyer, H., Oncken, O., Polom, U., Prochnow, U., Rabbel, W., Scheck, M. & Stiller, M., 1999. Deep crustal structure of the Northeast German Basin: new DEKORP-BASIN '96 deep-profiling results. *Geology* 27: 55-58.

7. References

- Delvaux, D., Moeys, R., Stapel, G., Petit, C., Levi, K., Miroshnichenko, A., Ruzhich, V., San'kov, V., 1997. Paleostress reconstructions and geodynamics of the Baikal region Central Asia, Part 2. Cenozoic rifting. *Tectonophysics* 282: 1-38.
- Delsman, J.R., van Baaren, E.S., Siemon, B., Dabekaussen, W., Karaoulis, M.C., Pauw, P.S., Vermaas, T., Bootsma, H., de Louw, P.G.B., Gunnink, J.L., Dubelaar, C.W., Menkovic, A., Steuer, A., Meyer, U., Revil, A., Oude Essink, G.H.P., 2018. Large-scale, probabilistic salinity mapping using airborne electromagnetics for groundwater management in Zeeland, the Netherlands. *Environmental Research Letters* 13.
- Ehlers, J., 2011. Geologische Karte von Hamburg 1: 25 000: Erläuterungen zu Blatt Nr. 2326 Fuhsbüttel. Behörde für Stadtentwicklung und Umwelt, Geologisches Landesamt Hamburg (Hamburg).
- Ehlers, J., Linke, G., 1989. The origin of deep buried channels of Elsterian age in northwest Germany. *Journal of Quaternary Science* 4: 255-265.
- Ehlers, J., Grube, A., Stephan, H.-J., Wansa, S., 2011. Pleistocene Glaciations of North Germany - New Results. In: Ehlers, J., Gibbard, P.L., Hughes, P.D. (eds.): *Quaternary Glaciations - Extent and Chronology - A Closer Look. Developments in Quaternary Science* 15. Elsevier (Amsterdam): 149-162.
- Eidvin, T., Rundberg, Y., 2007. Post-Eocene strata of the southern Viking Graben, northern North Sea; integrated biostratigraphic, strontium isotopic and lithostratigraphic study. *Norwegian Journal of Geology* 87: 391-450.
- Embry, A.F., 2009. *Practical Sequence Stratigraphy*. Canadian Society of Petroleum Geologists, 81 pp.
- Engelder, T., Geiser, P., 1980. On the use of regional joint sets as trajectories of paleostress fields during the development of the Appalachian Plateau, New York. *Journal of Geophysical Research* 85 B11: 6319-6341.
- Fischer, M.P., Wilkerson, M.S., 2000. Predicting the orientation of joints from fold shape: Results of pseudo-three-dimensional modeling and curvature analysis. *Geology* 28 (1): 15-18.
- Fraser, D.C., 1978. Resistivity mapping with an airborne multicoil electromagnetic system. *Geophysics* 43: 144-172.

7. References

- Fugro Consult GmbH, 2012. GeODin 7: <http://www.geodin.com>, Berlin, Germany.
- Gabriel, G., 2006. Gravity investigation of buried Pleistocene subglacial valleys. *Near Surface Geophysics* 4: 321-332.
- Gabriel, G., Kirsch, R., Siemon, B., Wiederhold, H., 2003. Geophysical investigations of buried Pleistocene subglacial valleys in Northern Germany. *Journal of Applied Geophysics* 53: 159-180.
- Gallagher, N.C., Wise, G.L., 1981. A theoretical analysis of the properties of median filters. *IEEE Transactions on Acoustics, Speech and Signal Processing, ASSP-29* (6), 1135-1141.
- Gast, R., 1988. Rifting im Rotliegenden Niedersachsens. *Die Geowissenschaften* 4: 115-122.
- Gast, R., Gundlach, T., 2006. Permian strike slip and extensional tectonics in Lower Saxony, Germany. *Zeitschrift der Deutschen Gesellschaft für Geowissenschaften* 157 (1): 41-55.
- Gohram, F.D., Woodward, L.A., Callender, J.F., Greer, A.R., 1979. Fractures in Cretaceous rocks from selected areas of the San Juan basin, New Mexico: exploration implications. *AAPG Bulletin* 64: 598-607.
- Gramann, F., 1988. Major palaeontological events and biostratigraphical correlations. *Geologisches Jahrbuch A100*: 410-423.
- Gramann, F., 1989. Forschungsbohrung Wursterheide. Benthonische Foraminiferen und verwandte Mikrofossilien. *Biostratigraphie, Faziesanalyse. Geologisches Jahrbuch A111*: 287-319.
- Gramann, F., Daniels, C.H. von, 1988. Benthic foraminifera: the description of the interregional zonation (B zones). *Geologisches Jahrbuch A100*: 145-151.
- Gramann, F., Kockel, F., 1988. Palaeogeographical, lithological, palaeoecological and palaeoclimatic development of the Northwest European Tertiary Basin. *Geologisches Jahrbuch A100*: 428-441.
- Grassmann, S., Cramer, B., Delisle, G., Messner, J., Winsemann, J., 2005. Geological history and petroleum system of the Mittelplate oil field, Northern Germany. *International Journal of Earth Sciences* 94: 979-989.

7. References

- Gunnink, J.L., Bosch, J.H.A., Siemon, B., Roth, B., Auken, E., 2012. Combining ground-based and airborne EM through artificial neural networks for modelling hydrogeological units under saline groundwater conditions. *Hydrology and Earth System Sciences* 16: 3061-3074.
- Hancock, P.L., 1985. Brittle microtectonics: principles and practice. *Journal of Structural Geology* 7: 437-457.
- Haq, B.U., Hardenbol, J., Vail, P.R., 1987. Chronology of fluctuating sea levels since the Triassic (250 million years ago to present). *Science* 235: 1156-1167.
- Hark, H.U., 1956. Eine klufftektonische Studie an der NW-Ecke des Harzes. Veröffentlicht in: *Abhandlungen der Braunschweigischen Wissenschaftlichen Gesellschaft*, Band 8: 23-35.
- Hayashi, K., Willis-Richards, J., Hopkirk, R.J., Niibori, Y., 1999. Numerical models of HDR geothermal reservoirs - a review of current thinking and progress. *Geothermics* 28: 507-518.
- Hennings, P.H., Olson, J.E., Thompson, L.B., 2000. Combining outcrop data and three-dimensional structural models to characterize fractured reservoirs: an example from Wyoming. *AAPG Bulletin* 84: 830-849.
- Hese, F., 2012. 3D Modellierungen und Visualisierung von Untergrundstrukturen für die Nutzung des unterirdischen Raumes in Schleswig-Holstein. PhD thesis, Christian-Albrechts-Universität zu Kiel, Germany.
- HGG, 2011. Guide to processing and inversion of SkyTEM data in the Aarhus Workbench. Technical report, Hydro-Geophysical Group, Department of Earth Sciences, University of Aarhus, Denmark.
- Hosseini, S.D., 1980. Klüfte und Styololithen am nordwestlichen Harzrand und im Lutterer Sattel in ihrer Bedeutung für die tektonische Auflösung dieses Gebietes. *Clausthaler Geologische Abhandlungen* 36.
- Höfle, H.C., Merkt, J., Müller, H., 1985. Die Ausbreitung des Eem-Meeres in Nordwestdeutschland. *Eiszeitalter und Gegenwart* 35: 49-59.

7. References

- Høyer, A.-S., Lykke-Andersen, H., Jørgensen, F., Auken, E., 2011. Combined interpretation of SkyTEM and high-resolution seismic data. *Journal of Physics and Chemistry of the Earth* 36 (16): 1386-1397.
- Hughes, A.L. C., Gyllencreutz, R., Lohne, Ø.S., Mangerud, J., Svendsen, J.I., 2016. The last Eurasian ice sheets – a chronological database and time-slice reconstruction, DATED-1. *Boreas* 45: 1-45.
- Huuse, M., 2002. Late Cenozoic palaeogeography of the eastern North Sea Basin climatic vs. tectonic forcing of basin margin uplift and deltaic progradation. *Bulletin of the Geological Society of Denmark* 49: 145-170.
- Huuse, M., Clausen, O.R., 2001. Morphology and origin of major Cenozoic sequence boundaries in the eastern North Sea Basin: top Eocene, near-top Oligocene and the mid-Miocene unconformity. *Basin Research* 13: 17-41.
- Huuse, M., Lykke-Andersen, H., 2000. Overdeepened Quaternary valleys in the eastern Danish North Sea: morphology and origin. *Quaternary Science Reviews* 19: 1233-1253.
- Huuse, M., Lykke-Andersen, H., Michelsen, O., 2001. Cenozoic evolution of the eastern North Sea Basin - new evidence from high-resolution and conventional seismic data. *Marine Geology* 177: 243-269.
- Huuse, M., Piotrowski, J.A., Lykke-Andersen, H., 2003. Geophysical investigations of buried Quaternary valleys in the formerly glaciated NW European lowland: significance for groundwater exploration. *Journal of Applied Geophysics* 53: 153-157.
- Janszen, A., 2012. Tunnel valleys: genetic models, sedimentary infill and 3D architecture. PhD thesis, Delft University of Technology.
- Janszen, A., Spaak, M., Moscariello, A., 2012. Effects of the substratum on the formation of glacial tunnel valleys: an example from the Middle Pleistocene of the southern North Sea Basin. *Boreas* 41: 629-643.
- Janszen, A., Moreau, J., Moscariello, A., Ehlers, J., Kröger, J., 2013. Time-transgressive tunnel-valley infill revealed by a three-dimensional sedimentary model, Hamburg, north-west Germany. *Sedimentology* 60 (3): 693-719.

7. References

- Jaritz, W., 1980. Einige Aspekte der Entwicklungsgeschichte der nordwestdeutschen Salzstöcke. *Zeitschrift der deutschen Geologischen Gesellschaft* 131, 387-408.
- Jaritz, W., 1987. The origin and development of salt structures in Northwest Germany. In: Lerche, I., O'Brian, J.J. (eds.): *Dynamical Geology of Salt and Related Structures*. Academic Press (Orlando, FL): 479-493.
- Jordan, H., Siemon, B., 2002. Die Tektonik des nordwestlichen Harzrandes - Ergebnisse der Hubschrauber-Elektromagnetik. *Zeitschrift der Deutschen Geologischen Gesellschaft* 153 (1): 31-50.
- Jørgensen, F., Sandersen, P.B.E., 2006. Buried and open tunnel valleys in Denmark - erosion beneath multiple ice sheets. *Quaternary Science Reviews* 25: 1339-1363.
- Jørgensen, F., Sandersen, P.B.E., 2009. Buried valley mapping in Denmark: evaluating mapping method constraints and the importance of data density. *Zeitschrift der deutschen Gesellschaft für Geowissenschaften* 160 (3): 211-229.
- Jørgensen, F., Lykke-Andersen, H., Sandersen, P.B.E., Auken, E., Nørmark, E., 2003a. Geophysical investigations of buried Quaternary valleys in Denmark: an integrated application of transient electromagnetic soundings, reflection seismic surveys and exploratory drillings. *Journal of Applied Geophysics* 53: 215-228.
- Jørgensen, F., Sandersen, P.B.P., Auken, E., 2003b. Imaging buried valleys using the transient electromagnetic method. *Journal of Applied Geophysics* 53: 215-228.
- Jørgensen, F., Sandersen, P.B.P., Auken, E., Lykke-Andersen, H., Sørensen, K., 2005. Contributions to the geological mapping of Mors, Denmark - A study based on large-scale TEM survey. *Bulletin of the Geological Society of Denmark* 52: 53-75.
- Jørgensen, F., Rønde Møller, R., Nebel, L., Jensen, N.-P., Christiansen, A.V., Sandersen, P.B.E., 2013. A method for cognitive 3D geological voxel modelling of AEM data. *Bulletin of Engineering Geology and the Environment* 72 (3-4): 421-432.
- Jürgens, U., 1996. Mittelmiozäne bis pliozäne Randmeer-Sequenzen aus dem deutschen Sektor der Nordsee. *Geologisches Jahrbuch* A146: 217-232.
- Kehew, A.E., Piotrowski, J.A., Jørgensen, F., 2012. Tunnel valleys: Concepts and controversies - A review. *Earth-Science Reviews* 113: 33-58.

7. References

- Keller, G.V., 1966. Electrical properties of rocks and minerals. In: Clark, S.P., Jr. (Ed.) Handbook of Physical Constants: Geological Society of America Memoir 97: 553-578.
- King, J., Oude Essink, G., Karaolis, M., Siemon, B., Bierkens, M. F. P., 2018. Quantifying geophysical inversion uncertainty using airborne frequency domain electromagnetic data – Applied at the province of Zeeland, the Netherlands. *Water Resources Research* 54: 8420–8441.
- Kleinspehn, K.L., Pershing, J., Teyssier, C. 1989. Paleostress stratigraphy: a new technique for analyzing tectonic control on sedimentary-basin subsidence. *Geology* 17: 53-246.
- Kley, J., Voigt, T., 2008. Late Cretaceous intraplate thrusting in central Europe: Effect of Africa-Iberia-Europe convergence, not Alpine collision. *Geology* 36 (11), 839-842.
- Kley, J., Franzke, H.J., Jähne, F., Krawczyk, C., Lohr, T., Reicherter, K., Scheck-Wenderoth, M., Sippel, J., Tanner, D., van Gent, H., 2008. Strain and stress. In: Littke, R., Bayer, U., Gajewski, D., Nelskamp, S. (eds) *Dynamics of complex intracontinental basins. The Central European Basin System*, Springer, pp 97-124.
- Klimke, J., Wiederhold, H., Winsemann, J., Ertl, G., Elbracht, J., 2013. Three-dimensional mapping of Quaternary sediments improved by airborne electromagnetics in the case of the Quakenbrück Basin, Northern Germany. *Zeitschrift der deutschen Gesellschaft für Geowissenschaften* 164 (2): 369-384.
- Kluiving, S.J., Bosch, J.H.A., Ebbing, J.H.J., Mesdag, C.S., Westerhoff, R.S., 2003. Onshore and offshore seismic and lithostratigraphic analysis of a deeply incised Quaternary buried valley-system in the Northern Netherlands. *Journal of Applied Geophysics* 53: 249-271.
- Knox, R.W.O.B., Bosch, J.H.A., Rasmussen, E.S., Heilmann-Clausen, C., Hiss, M., De Lugt, I.R., Kasiński, J., King, C., Köthe, A., Słodkowska, B., Standke, G., Vandenberghe, N., 2010. Cenozoic. In: Doornenbal, J.C., Stevenson, A.G. (eds.): *Petroleum Geological Atlas of the Southern Permian Basin Area*. EAGE Publications b.v. (Houten): 211-223.

7. References

- Knudsen, K.L., 1988. Marine Interglacial Deposits in the Cuxhaven Area, NW Germany: A Comparison of Holsteinian, Eemian and Holocene Foraminiferal Faunas. *Eiszeitalter und Gegenwart* 38: 69-77.
- Knudsen, K.L., 1993a. Foraminiferal Faunas in Holsteinian Deposits of the Neuwerk Area, Germany. *Geologisches Jahrbuch A138*: 77-95.
- Knudsen, K.L., 1993b. Late Elsterian-Holsteinian Foraminiferal Stratigraphy in Boreholes in the Lower Elbe Area, NW Germany. *Geologisches Jahrbuch A138*: 97-119.
- Kockel, F., 2002. Rifting processes in NW-Germany and the German North Sea Sector. *Netherlands Journal of Geosciences/Geologie en Mijnbouw* 81: 149-158.
- Kockel, F., 2003. Inversion structures in Central Europe - Expressions and reasons, an open discussion. *Netherlands Journal of Geosciences/Geologie en Mijnbouw* 82: 367-382.
- Koltermann, C.E., Gorelick, S.M., 1996. Heterogeneity in sedimentary deposits: a review of structure-imitating, process-imitating, and descriptive approaches. *Water Resources Research* 32: 2617-2658.
- Konradi, P., 2005. Cenozoic stratigraphy in the Danish North Sea Basin. *Geologie en Mijnbouw* 84: 109-111.
- Köthe, A., 2007. Cenozoic biostratigraphy from the German North Sea sector (G-11-1 borehole, dinoflagellate cysts, calcareous nannoplankton). *Zeitschrift der deutschen Gesellschaft für Geowissenschaften* 158 (2): 287-327.
- Köthe, A., Gaedicke, C., Rüdiger, L., 2008. Erratum: The age of the Mid-Miocene Unconformity (MMU) in the G-11-1 borehole, German North Sea sector. *Zeitschrift der deutschen Gesellschaft für Geowissenschaften* 159 (4): 687-689.
- Krawczyk, C.M., Stiller, M. & Dekorp-Basin Research Group, 1999. Reflection seismic constraints on Paleozoic crustal structure and Moho beneath the NE German Basin. *Tectonophysics* 314: 241-253.
- Krige, D.G., 1951. A statistical approach to some basic mine valuation problems on the Witwatersrand. *Journal of the Chemical, Metallurgical and Mining Society of South Africa* 52 (6): 119-139.

7. References

- Kuhlmann, G., de Boer, P., Pedersen, R.B., Wong, T.E., 2004. Provenance of Pliocene sediments and paleoenvironmental changes in the southern North Sea region using Samarium-Neodymium (Sm/Nd) provenance ages and clay mineralogy. *Sedimentary Geology* 171: 205-226.
- Kuhlmann, G., Wong, T.E., 2008. Pliocene paleoenvironment evolution as interpreted from 3D-seismic data in the southern North Sea, Dutch offshore sector. *Marine and Petroleum Geology* 25: 173-189.
- Kuster, H., 2005. Das jüngere Tertiär in Nord- und Nordostniedersachsen. *Geologisches Jahrbuch A158*: 0-194.
- Kuster, H., Meyer, K.-D., 1979. Glaziäre Rinnen im mittleren und nordöstlichen Niedersachsen. *Eiszeitalter und Gegenwart* 29: 135-156.
- Kuster, H., Meyer, K.-D., 1995. Quartärgeologische Übersichtskarte von Niedersachsen und Bremen, 1 : 500 000. Niedersächsisches Landesamt für Bodenforschung, Hannover.
- Lane, R., Green, A., Golding, C., Owers, M., Pik, P., Plunkett, C., Sattel, D., Thorn, B., 2000. An example of 3D conductivity mapping using the TEMPEST airborne electromagnetic system. *Exploration Geophysics* 31: 162-172.
- Lang, J., Winsemann, J., Steinmetz, D., Polom, U., Pollok, L., Böhner, U., Serangeli, J., Brandes, C., Hampel, A., Winghart, S., 2012. The Pleistocene of Schöningen, Germany: a complex tunnel valley fill revealed from 3D subsurface modelling and shear wave seismics. *Quaternary Science Reviews* 39: 86-105.
- Lang, J., Lauer, T., Winsemann, J., 2018. New age constraints for the Saalian glaciation in northern central Europe: Implications for the extent of ice sheets and related proglacial lake systems. *Quaternary Science Reviews* 180: 240-259.
- Lewicki, J.L., Birkholzer, J., Tsang, C-F., 2006. Natural and industrial analogues for leakage of CO₂ from storage reservoirs: identification of features, events, and processes and lessons learned. *Environmental Geology* 52: 457-467.
- Linke, G., 1993. Zur Geologie und Petrographie der Forschungsbohrungen qho 1-5, der Bohrung Hamburg-Billbrook und des Vorkommens von marinem Holstein im Gebiet Neuwerk-Scharhörn. *Geologisches Jahrbuch A138*: 35-76.

7. References

- Litt, T., Behre, K.-E., Meyer, K.-D., Stephan, H.-J., Wansa, S., 2007. Stratigraphische Begriffe für das Quartär des norddeutschen Vereisungsgebietes. *Eiszeitalter und Gegenwart* 56: 7-65.
- Litt, T., Schmincke, H.-U., Frechen, M., Schlüchter, C., 2008. Quaternary. In: McCann, T. (Ed.), *The Geology of Central Europe. Mesozoic and Cenozoic 2*, pp 1287-1340.
- Logan, C.E., Hinton, M.J., Sharpe, D.R., Oldenborger, G.A., Russell, H.A.J., Pugin, A.J-M., 2015. Spiritwood Buried Valley 3D geological modelling: Part of a multidisciplinary aquifer characterization workflow: Geological Survey of Canada, Open file 7866.
- Lohr, T., Krawczyk, C.M., Oncken, O., Tanner, D.C., 2008. Evolution of a fault surface from 3D attribute analysis and displacement measurements. *Journal of Structural Geology*, 30: 690-700.
- Lutz, R., Kalka, S., Gaedicke, C., Reinhardt, L., Winsemann, J., 2009. Pleistocene tunnel valleys in the German North Sea: spatial distribution and morphology. *Zeitschrift der deutschen Gesellschaft für Geowissenschaften* 160 (3): 225-235.
- Lucier, A., Zoback, M., Gupta, N., Ramakrishnan, T.S., 2006. Geomechanical aspects of CO₂ sequestration in a deep saline reservoir in the Ohio River Valley region. *AAPG Bulletin* 13: 85-103.
- Mallet, J.-L., 2002. *Geomodeling*. Oxford University Press (New York): 624 pp.
- Mangerud, J., Jansen, E., Landvik, J.Y., 1996. Late Cenozoic history of the Scandinavian and Barents Sea ice sheets. *Global and Planetary Change* 12: 11-26.
- Mann, C.J., 1993. Uncertainty in geology. In: Davis, J.C., Herzfeld, U.C. (eds.): *Computers in geology - 25 years of progress*. Oxford University Press (Oxford): 241-254.
- Marker, P.A., Bauer-Gottwein, P., Mosegaard, K. (2016). Informing groundwater model hydrostratigraphy with airborne time-domain electromagnetic data and borehole logs. Kgs. Lyngby: Technical University of Denmark, DTU Environment.
- Marks, L., 2011. Quaternary glaciations in Poland. *Developments in Quaternary Sciences* 15: 299-303.

7. References

- Maystrenko, Y., Bayer, U., Scheck-Wenderoth, M., 2005a. The Glückstadt Graben, a sedimentary record between the North- and Baltic Sea in North Central Europe. *Tectonophysics* 397: 113-126.
- Maystrenko, Y., Bayer, U., Scheck-Wenderoth, M., 2005b. Structure and evolution of the Glückstadt Graben due to salt movements. *International Journal of Earth Science* 94: 799-814.
- Maystrenko, Y., Bayer, U., Scheck-Wenderoth, M., 2013. Salt as a 3D element in structural modeling - Example from the Central European Basin System. *Tectonophysics* 591: 62-82.
- Michelsen, O., Danielsen, M., Heilmann-Clausen, C., Jordt, H., Laursen, G.V., Thomsen, E., 1995. Occurrence of major sequence stratigraphic boundaries in relation to basin development in Cenozoic deposits of the southeastern North Sea. In: Steel, R.J., Felt, V.L., Johannesen, E.P., Mathieu, C. (eds.): *Sequence Stratigraphy of the Northwest European Margin*. Special Publications 5, Norwegian Petroleum Society (Stavanger, Norway): 415-427.
- Michelsen, O., Thomsen, E., Danielsen, M., Heilmann-Clausen, C., Jordt, H., Laursen, G.V., 1998. Cenozoic sequence stratigraphy in the eastern North Sea. In: Graciansky, P.-C. de, Hardenbol, J. Jacquin, T., Vail, P.R. (eds.): *Mesozoic and Cenozoic Sequence Stratigraphy of European Basins*. Special Publication 60, Society for Sedimentary Geology (Oklahoma, USA): 91-118.
- Miller, K.G., Kominz, M.A., Browning, J.V., Wright, J.D., Mountain, G.S., Katz, M.E., Sugarman, P.J., Cramer, B.S., Christie-Blick, N., Pekar, S.F., 2005. The Phanerozoic record of global sea-level change. *Science* 310: 1293-1298.
- Mitchum, R.M., Vail, P.R., Sangree, J.B., 1977. Seismic stratigraphy and global changes of sea-level, Part 6: stratigraphic interpretation of seismic reflection patterns in depositional sequences. In: Payton, C.E. (ed.): *Seismic Stratigraphy - Applications to Hydrocarbon Exploration*. AAPG Memoir 26 (Houston, Texas): 117-133.
- Mohr, K., 1982. Harzvorland. Westlicher Teil. Sammlung geologischer Führer. Gebrüder Borntraeger, Berlin, Stuttgart, 142 pp.

7. References

- Mohr, M., Kukla, P.A., Urai, J.L., Bresser, G., 2005. Multiphase salt tectonic evolution in NW Germany: seismic interpretation and retro-deformation. *International Journal of Earth Sciences* 94: 917-940.
- Møller, L.K., Rasmussen, E.S., Clausen, O. R., 2009. Clinoform migration patterns of a Late Miocene delta complex in the Danish Central Graben; implications for relative sea-level changes. *Basin Research* 21: 704-720.
- Moreau, J., Huuse, M., 2014. Infill of tunnel valleys associated with landward-flowing ice sheets: The missing Middle Pleistocene record of the NW European rivers? *Geochemistry, Geophysics, Geosystems* 15 (1): 1-9.
- Moreau, J., Huuse, M., Janszen, A., van der Vegt, P., Gibbard, P.L., Moscariello, A., 2012. The glaciogenic unconformity of the southern North Sea. In: Huuse, M., Redfern, J., Le Heron, D.P., Dixon, R.J., Moscariello, A., Craig, J. (eds.): *Glaciogenic Reservoirs and Hydrocarbon Systems*. Special Publications 368, Geological Society (London): 99-110.
- Müller, H., Höfle, H.-C., 1994. Die Holstein-Interglazialvorkommen bei Bossel westlich von Stade und Wanhöden nördlich Bremerhaven. *Geologisches Jahrbuch A134*: 71-116.
- Narr, W., 1991. Fracture density in the deep subsurface: techniques with application to Point Arguello oil field. *AAPG Bulletin* 75: 1300-1323.
- Newman, G.A., Hohmann, G.W., Anderson, W.L., 1986. Transient electromagnetic response of a 3-dimensional body in layered earth. *Geophysics* 51 (8): 1608-1627.
- Odin, G.S., Kreuzer, H., 1988. Geochronology: some geochronological calibration points for lithostratigraphic units. *Geologisches Jahrbuch A100*: 403-410.
- Oldenborger, G.A., Logan, C.E., Hinton, M.J., Pugin, A.J.-M., Sapia, V., Sharpe, D.R., Russell, H.A.J., 2016. Bedrock mapping of buried valley networks using seismic reflection and airborne electromagnetic data. *Journal of Applied Geophysics* 128: 191-201.
- Ortlam, D., 2001. Geowissenschaftliche Erkenntnisse über den Untergrund Bremerhavens. *Bremisches Jahrbuch* 80: 181-197.

7. References

- Overeem, I., Weltje, G.J., Bishop-Kay, C., Kroonenberg, S.B., 2001. The late Cenozoic Eridanos delta system in the southern North Sea Basin: a climate signal in sediment supply? *Basin Research* 13: 293-312.
- Paine, J.G., Minty, B.R.S., 2005. Airborne hydrogeophysics. In: Rubin, Y., Hubbard, S.S. (eds.): *Hydrogeophysics*. Springer (Dordrecht): 333-357.
- Paine, J.G., Collins, E.W., 2017. Identifying ground-water resources and intrabasinal faults in the Hueco Bolson, West Texas using airborne electromagnetic induction and magnetic-field data. *Journal of Environmental and Engineering Geophysics* 22/1: 63-81.
- Palacky, G.V., 1987. Resistivity characteristics of geologic targets. *Electromagnetic Methods in Applied Geophysics*, SEG 1351.
- Palamara, D.R., Rodriguez, V.B., Kellett, J., Macaulay, S., 2010. Salt mapping in the Lower Macquarie area, Australia, using airborne electromagnetic data. *Environmental Earth Sciences* 61: 613-623.
- Paradigm®, 2011. GOCAD®. Version 2009.3, Patch 2.
- Persson, L., Erlström M., 2015. Geophysical imaging of Silurian carbonates by use of ground and airborne electromagnetic and radiometric methods on the island of Gotland, Sweden. *Interpretation* 3: 1-11.
- Pharaoh, T.C., Dusaar, M., Geluk, M.C., Kockel, F., Krawczyk, C.M., Krzywiec, P., Scheck-Wenderoth, M., Thybo, H., Vejbæk, O.V., Wees, J.D. van, 2010. Tectonic evolution. In: Doornenbal, J.C., Stevenson, A.G., (eds.): *Petroleum Geological Atlas of the Southern Permian Basin Area*. EAGE Publications b.v. (Houten): 25-57.
- Plink-Björklund, P., 2008. Wave-to-tide facies change in a Campanian shoreline complex, Chimney Rock Tongue, Wyoming-Utah, U.S.A. In: Hampson, G.J., Steel, R.J., Burgess, P.M., Dalrymple, R.W. (eds.): *Recent Advances in Models of Siliciclastic Shallow-Marine Stratigraphy*. Special Publications 90, Society for Sedimentary Geology (Oklahoma, USA): 265-292.
- Posamentier, H.W., Allen, G.P., 1999. Siliciclastic Sequence Stratigraphy: concepts and applications. *SEPM, Concepts in Sedimentology and Paleontology* 7, 210 pp.

7. References

- Praeg, D., 2003. Seismic imaging of mid-Pleistocene tunnel-valleys in the North Sea Basin - high resolution from low frequencies. *Journal of Applied Geophysics* 53: 273-298.
- Pryet, A., Ramm, J., Chilès, J.-P., Auken, E., Deffontaines, B., Violette, S., 2011. 3D resistivity gridding of large AEM datasets: A step toward enhanced geological interpretation. *Journal of Applied Geophysics* 75: 277-283.
- Pugin, A.J.M., Oldenborger, G.A., Cummings, D.I., Russell, H.A., Sharpe, D.R., 2014. Architecture of buried valleys in glaciated Canadian Prairie regions based on high resolution geophysical data: *Quaternary Science Reviews* 86: 13-23.
- Rasmussen, E.S., 2004. The interplay between true eustatic sea-level changes, tectonics, and climatic changes: what is the dominating factor in sequence formation of the Upper Oligocene-Miocene succession in the eastern North Sea Basin, Denmark? *Global and Planetary Change* 41: 15-30.
- Rasmussen, E.S., Dybkjær, K., 2013. Patterns of Cenozoic sediment flux from western Scandinavia: discussion. *Basin Research* 25: 1-9.
- Rasmussen, E.S., Heilmann-Clausen, C., Waagstein, R., Eidvin, T., 2008. The Tertiary of Norden. *Episodes* 31: 66-72.
- Rasmussen, E.S., Dybkjær, K., Piasecki, S., 2010. Lithostratigraphy of the Upper Oligocene - Miocene succession of Denmark. *Geological Survey of Denmark and Greenland Bulletin* 22, 92 pp.
- Reinson, G.E., 1992. Transgressive barrier island and estuarine systems. In: Walker, R.G., James, N.P. (Eds.), *Facies Models: Response to Sea Level Change*. Geological Association of Canada 1: 179-194.
- Roberts, A., 2001. Curvature attributes and their application to 3D interpreted horizons. *First break*, Volume 19 (2).
- Roden, R., Smith, T., Sacrey, D., 2015. Geologic pattern recognition from seismic attributes: Principal component analysis and self-organizing maps. *Interpretation* 3(4), SAE59-SAE83.

7. References

- Roskosch, J., Winsemann, J., Polom, U., Brandes, C., Tsukamoto, S., Weitkamp, A., Bartholomäus, W.A., Henningsen, D., Frechen, M., 2015. Luminescence dating of ice-marginal deposits in northern Germany: evidence for repeated glaciations during the Middle Pleistocene (MIS 12 to MIS 6). *Boreas*.
- Ross, M., Parent, M., Lefebvre, R., 2005. 3D geologic framework models for regional hydrogeology and land-use management: a case study from a Quaternary basin of southwestern Quebec, Canada. *Hydrogeology Journal* 13: 690-707.
- Rumpel, H.-M., Grelle, T., Grüneberg, S., Großmann, E., Rode, W., 2006a. Reflexionsseismische Untersuchungen der Cuxhavener Rinne bei Midlum 2005. Technischer Bericht, GGA-Institut, Archiv-Nr. 126 015 (Hannover).
- Rumpel, H.-M., Binot, F., Gabriel, G., Hinsby, K., Siemon, B., Steuer, A., Wiederhold, H., 2006b. Cuxhavener Rinne. In: Kirsch, R., Rumpel, H.-M., Scheer, W., Wiederhold, H. (eds.): *BurVal Working Group: Groundwater resources in buried valleys - a challenge for geosciences*. Bonifatius GmbH (Hannover): 227-240.
- Rumpel, H.-M., Binot, F., Gabriel, G., Siemon, B., Steuer, A., Wiederhold, H., 2009. The benefit of geophysical data for hydrogeological 3D modelling - an example using the Cuxhaven buried valley. *Zeitschrift der deutschen Gesellschaft für Geowissenschaften* 160 (3): 259-269.
- Rundberg, Y., Smalley, P.C., 1989. High-resolution dating of Cenozoic sediments from the northern North Sea using $^{87}\text{Sr}/^{86}\text{Sr}$ stratigraphy. *AAPG Bulletin* 73: 298-308.
- Saintot, A., Angelier, J., 2002. Tectonic paleostress fields and structural evolution of the NW-Caucasus fold-and-thrust belt from Late Cretaceous to Quaternary. *Tectonophysics*, 357: 1-31.
- Sandersen, P.B.E., Jørgensen, F., 2003. Buried Quaternary valleys in western Denmark - occurrence and inferred implications for groundwater resources and vulnerability. *Journal of Applied Geophysics* 53: 229-248.
- Scheck-Wenderoth, M., Lamarche, J., 2005. Crustal memory and basin evolution in the Central European Basin System-new insights from a 3D structural model. *Tectonophysics* 397: 143-165.

7. References

- Sengpiel, K.-P., Siemon, B., 2000. Advanced inversion methods for airborne electromagnetics. *Geophysics* 65: 1983-1992.
- Siemon, B., 2001. Improved and new resistivity-depth profiles for helicopter electromagnetic data. *Journal of Applied Geophysics* 46: 65-76.
- Siemon, B., 2005. Ergebnisse der Aeroelektromagnetik zur Grundwassererkundung im Raum Cuxhaven-Bremerhaven. *Zeitschrift für Angewandte Geologie* 1: 7-13.
- Siemon, B., Stuntebeck, C., Sengpiel, K.-P., Röttger, B., Rehli, H.-J., Eberle, D., 2002. Characterisation of hazardous waste sites using the BGR helicopter-borne geophysical system. *Journal of Environmental and Engineering Geophysics* 7: 169-181.
- Siemon, B., Eberle, D.G., Binot, F., 2004. Helicopter-borne electromagnetic investigation of coastal aquifers in North-West Germany. *Zeitschrift für geologische Wissenschaften* 32: 385-395.
- Siemon, B., Christiansen, A.V., Auken, E., 2009a. A review of helicopter-borne electromagnetic methods for groundwater exploration. *Near Surface Geophysics* 7: 629-646.
- Siemon, B., Auken, E., Christiansen, A.V., 2009b. Laterally constrained inversion of helicopter-borne frequency-domain electromagnetic data. *Journal of Applied Geophysics* 67: 259-268.
- Siemon, B., Steuer, A., Ullmann, A., Vasterling, M., Voß, M., 2011. Application of frequency-domain helicopter-borne electromagnetics for groundwater exploration in urban areas. *Physics and Chemistry of the Earth* 36: 1373-1385.
- Siemon, B., Costabel, S., Voß, W., Meyer, U., Deus, N., Elbracht, J., Günther, T., Wiederhold, H., 2015. Airborne and ground geophysical mapping of coastal clays in Eastern Friesland, Germany. *Geophysics* (3), WB21-WB34.
- Sippel, J., 2009. The Paleostress History of the Central European Basin System. Scientific Technical Report, Deutsches Geoforschungszentrum Potsdam GFZ 2009 (6).
- Slapansky, P., Motschka, K., Bieber, G., Ahl, A., Winkler, E., Schattauer, I., Papp, E., 2017. Aero-geophysikalische Vermessung im Bereich Wörgl (T), Endbericht ÜLG-20/12c & 13c, ÜLG-28/14b & 15b, 221 S., Wien.

7. References

- Sørensen, K., Auken, E., 2004. SkyTEM - a new high-resolution helicopter transient electromagnetic system. *Exploration Geophysics* 35: 191-199.
- Sørensen, J.C., Gregersen, U., Breiner, M., Michelsen, O., 1997. Highfrequency sequence stratigraphy of Upper Cenozoic deposits in the central and southeastern North Sea areas. *Marine and Petroleum Geology* 14 (2): 99-123.
- Stackebrandt, W., 2009. Subglacial channels of Northern Germany - a brief review. *Zeitschrift der deutschen Gesellschaft für Geowissenschaften* 160 (3): 203-210.
- Steinmetz, D., Winsemann, J., Brandes, C., Siemon, B., Ullmann, A., Wiederhold, H., Meyer, U., 2015. Towards an improved geological interpretation of airborne electromagnetic data: a case study from the Cuxhaven tunnel valley and its Neogene host sediments (northwest Germany). *Netherlands Journal of Geosciences* 94: 201-227.
- Steuer, A., 2008. Joint application of ground based transient electromagnetics and airborne electromagnetics. PhD thesis, University of Cologne, Germany.
- Steuer, A., Siemon, B., Auken, E., 2009. A comparison of helicopter-borne electromagnetics in frequency- and time-domain at the Cuxhaven valley in Northern Germany. *Journal of Applied Geophysics* 67: 194-205.
- Stewart, S., 2006. Implications of passive salt diapir kinematics for reservoir segmentation by radial and concentric faults. *Marine and Petroleum Geology* 23: 843-853.
- Stewart, M.A., Lonergan, L., 2011. Seven glacial cycles in the middle-late Pleistocene of northwest Europe: Geomorphic evidence from buried tunnel valleys. *Geology* 39: 283-286.
- Stewart, M.A., Lonergan, L., Hampson, G., 2013. 3D seismic analysis of buried tunnel valleys in the central North Sea: morphology, cross-cutting generations and glacial history. *Quaternary Science Reviews* 72: 1-17.
- Stoker, M.S., Hout, R.J., Nielsen, T., Hjelstuen, B.O., Laberg, J.S., Shannon, P.M., Praeg, D., Mathiesen, A., Weering, T.C.E. van, McDonnell, A., 2005a. Sedimentary and oceanographic responses to early Neogene compression on the NW European margin. *Marine Petroleum Geology* 22: 1031-1044.

7. References

- Stoker, M.S., Praeg, D., Hjelstuen, B.O., Laberg, J.S., Nielsen, T., Shannon, P.M., 2005b. Neogene stratigraphy and the sedimentary and oceanographic development of the NW European Atlantic margin. *Marine Petroleum Geology* 22: 977-1005.
- Stollhofen, H., Bachmann, G., Barnasch, J., Bayer, U., Beutler, G., Franz, M., Kästner, M., Legler, B., Mutterlose, J., Radies, D., 2008. Upper Rotliegend to Early Cretaceous basin development. In: Littke, R., Bayer, U., Gajewski, D., Nelskamp, S. (eds) *Dynamics of complex intracontinental basins. The Central European Basin System*, Springer, pp 181-210.
- Streif, H., 2004. Sedimentary record of Pleistocene and Holocene marine inundations along the North Sea coast of Lower Saxony, Germany. *Quaternary International* 112 (1): 3-28.
- Strong, N., Paola, C., 2008. Valleys that never were: time versus stratigraphic surfaces. *Journal of Sedimentary Research* 78, 579-593.
- Tanner, D. C., Krawczyk, C., 2017 online: Restoration of the Cretaceous uplift of the Harz Mountains, North Germany: evidence for the geometry of a thick-skinned thrust. *International Journal of Earth Sciences*.
- Thöle, H., Gaedicke, C., Kuhlmann, G., Reinhardt, L., 2014. Late Cenozoic sedimentary evolution of the German North Sea – A seismic stratigraphic approach. *Newsletters on Stratigraphy* 47 (3): 299-329.
- Tølbøll, R.J., 2007. The application of frequency-domain helicopter-borne electromagnetic methods to hydrogeological investigations in Denmark. PhD thesis, Department of Earth Sciences, University of Aarhus, Denmark.
- Ullmann, A., Scheunert, M., Afanasjew, M., Börner, R.-U., Siemon, B., Spitzer, K., 2016. A cut-&-paste strategy for the 3-D inversion of helicopter-borne electromagnetic data - II. Combining regional 1-D and local 3-D inversion. *Journal of Applied Geophysics* 130: 131-144.
- van der Vegt, P., Janszen, A., Moscariello, A., 2012. Glacial tunnel valleys - current knowledge and future perspectives. In: Huuse, M., Redfern, J., Le Heron, D.P., Dixon, R.J., Moscariello, A., Craig, J. (eds.): *Glaciogenic Reservoirs and Hydrocarbon Systems*, Special Publications 368, Geological Society (London): 75-97.

7. References

- van Wees, J.-D., Stephenson, R.A., Ziegler, P.A., Bayer, U., McCann, T., Dadlez, R., Gaupp, R., Narkiewicz, M., Bitzer, F., Scheck, M., 2000. On the origin of the Southern Permian Basin, Central Europe. *Marine and Petroleum Geology* 17: 43-59.
- Veeken, P.C.H., Moerkerken, B. van, 2013. *Seismic Stratigraphy and Depositional Facies Models*. EAGE Publications b.v., Houton, 494 pp.
- Venteris, E.R., 2007. Three-dimensional modeling of glacial sediments using public water-well data records: an integration of interpretive and geostatistical approaches. *Geospheres* 3: 456-468.
- Viezzoli, A., Christiansen, A.V., Auken, E., Sørensen, K., 2008. Quasi-3D modeling of airborne TEM data by spatially constrained inversion. *Geophysics* 73 (3): F105-F113.
- Vignoli, G., Sapia, V., Menghini, A., Viezzoli, A., 2017. Examples of Improved Inversion of Different Airborne Electromagnetic Datasets Via Sharp Regularization. *Journal of Environmental and Engineering Geophysics* 22 (1): 51-61.
- Voigt, T., Wiese, F., Eynatten, H. von, Franzke, H.-J., Gaupp, R., 2006. Facies evolution of syntectonic upper cretaceous deposits in the Subhercynian Cretaceous basin and adjoining areas (Germany). *Zeitschrift der Deutschen Gesellschaft für Geowissenschaften* 157, 203-244.
- von Eynatten, H., Voigt, T., Meier, A., Franzke, H.-J., Gaupp, R., 2008. Provenance of the clastic Cretaceous Subhercynian basin fill: constraints to exhumation of the Harz mountains and the timing of inversion tectonics in the Central European Basin. *International Journal of Earth Science* 97: 1315-1330.
- Walker, R.G., Plint, A.G., 1992. Wave and storm-dominated shallow marine systems. In: Walker, R.G., James, N.P. (eds.): *Facies Models: Response to Sea Level Change*. Geological Association of Canada (St. John's, Newfoundland): 219-238.
- Wellmann, J.F., Regenauer-Lieb, K., 2012. Effect of geological data quality on uncertainties in geological model and subsurface flow fields. *PROCEEDINGS, Thirty-Seventh Workshop on Geothermal Reservoir Engineering Stanford University, Stanford, California, January 30 - February 1, 2012 SGP-TR-194*.

7. References

- West, G.F., Macnae, J.C., 1991. Physics of the electromagnetic induction exploration method. In: Nabighian, M.N., Corbett, J.D. (eds.): Electromagnetic methods in applied geophysics. Investigations in geophysics, Society of Exploration Geophysicists 2: 5-45.
- Wiederhold, H., Binot, F., Kessels, W., 2005a. Die Forschungsbohrung Cuxhaven und das „Coastal Aquifer Testfield (CATField)“ - ein Testfeld für angewandte geowissenschaftliche Forschung. Zeitschrift für Angewandte Geologie 1: 3-5.
- Wiederhold, H., Gabriel, G., Grinat, M., 2005b. Geophysikalische Erkundung der Bremerhaven-Cuxhavener Rinne im Umfeld der Forschungsbohrung Cuxhaven. Zeitschrift für Angewandte Geologie 1: 28-38.
- Wingfield, R., 1990. The origin of major incisions within the Pleistocene deposits of the North Sea. Marine Geology 91: 31-52.
- Winsemann, J., Brandes, C., Polom, U., Weber, C., 2011. Depositional architecture and palaeogeographic significance of Middle Pleistocene glaciolacustrine ice marginal deposits in northwestern Germany: a synoptic overview. E & G International Quaternary Journal 60: 212-235.
- Winsemann, J., Lang, J., Roskosch, J., Polom, U., Böhner, U., Brandes, C., Glotzbach, C., Frechen, M., 2015. Terrace styles and timing of terrace formation in the Weser and Leine valleys, northern Germany: response of a fluvial system to climate change and glaciation. Quaternary Science Reviews 123: 31-57.
- Winsemann, J., Alho, P., Laamanen, L., Goseberg, N., Lang, J., Klostermann, J., 2016. Flow dynamics, sedimentation and erosion of glacial lake outburst floods along the Middle Pleistocene Scandinavian ice sheet (northern Central Europe). Boreas 45: 260-283.
- Yilmaz, Ö., 2001. Seismic data analysis: processing, inversion and interpretation of seismic data. Society of Exploration Geophysicists, Tulsa, 2027 pp.
- Zachos, J., Pagani, M., Sloan, L., Thomas, E., Billups, K., 2001. Trends, rhythms, and aberrations in global climate 65 Ma to present. Science 292: 686-693.
- Zahm, C.Z., Hennings, P.H., 2009. Complex fracture development related to stratigraphic architecture: challenges for structural deformation prediction, Tensleep Sandstone at the Alcova anticline, Wyoming. AAPG Bulletin 93: 1427-1446.

7. References

- Zellmer, H., Holländer, R., 1996. Stratigraphisches Profil der Umgebung von Braunschweig. Institut für Geowissenschaften der TU Braunschweig, 1 Blatt; Braunschweig.
- Zhao, J., Brown, E.T., 1992. Hydro-thermo-mechanical properties of joints in the Carnmenellis granite. *Quarterly Journal of Engineering Geology* 25: 279-290.
- Zhdanov, M.S., 2010. Electromagnetic geophysics: notes from the past and the road ahead. *Geophysics* 75 (5): 75A49-75A66.
- Ziegler, P., 1990. Geological atlas of Western and Central Europe, 2nd ed., Geol. Soc. Publ. House, Bath, Shell International Petroleum Mij, B.v., 239 pp.

Acknowledgements

I gratefully acknowledge Prof. Dr. Jutta Winsemann for supervision and support during all stages of this thesis. Bernhard Siemon did a great job with the preparation and first interpretation of airborne electromagnetics. Dr. Christian Brandes is thanked for support in fieldwork, discussion, and contributing to the publication. Angelika Ullmann, Peter Menzel, Dr. Helga Wiederhold, Dr. Uwe Meyer are thanked for their contributions to the publications.

Financial support by the German Federal Ministry of Education and Research (BMBF) is gratefully acknowledged (grant 03G0735). The members of the joint research program of GEOTECHNOLOGIEN, and especially the project partners of AIDA are gratefully thanked for the constructive cooperation. I am grateful to the AIDA project partners, the University of Kiel, the State Authority for Mining, Energy and Geology (LBEG) for providing borehole data, to Fugro for providing the GeODin software and Paradigm for GOCAD software support. Janine Meinsen, Dr. Julia Roskosch, Dr. Jörg Lang, Dr. Mauritz Horikx, Ariana Osman, Axel Weitkamp, Dr. Georgios Maniatis, Dr. Heidi Turpeinen, Dr. Tao Li are thanked for discussions. Special thanks go to the CONSULAQUA, especially to Hilger Schmedding, for supporting the final phase of writing.

Zum Schluß gilt der Dank meinen Liebsten, all denen die mich in den letzten Jahren immer wieder neu motiviert haben, insbesondere Claudia, Jan und Niklas, sowie meinen Eltern und meinem Bruder.

Curriculum vitae

Personal information

Date of birth July 26th, 1984
Nationality German
Place of birth Osterburg
Status unmarried, 2 children

Professional experience

since 10/2017 **Projektleiter**
 CONSULAQUA Hildesheim,
 Niederlassung der CONSULAQUA Hamburg Beratungsgesellschaft mbH
 Water resources management.

12/2014 - 09/2017 **Projektleiter**
 AWIA Umwelt GmbH, Göttingen
 Environmental protection, restoration and rehabilitation.

11/2010 - 11/2014 **Scientific employee and PhD student**
 Institut für Geologie, Gottfried Wilhelm Leibniz Universität Hannover
 Research, analysis and interpretation of geophysical and geological data
 (e.g., airborne electromagnetic, seismic, borehole and gravity data),
 geomodelling (GOCAD/SKUA), publication and presentation, lectures
 (GOCAD student course) and excursions

Education and academic studies

10/2004 - 10/2010 **Geosciences**

Gottfried Wilhelm Leibniz Universität Hannover

Major topics: economic geology, sedimentation systems, Quaternary geology, hydrogeology, geochemical analysis methods and experimental geochemistry

Minor topic: material science

Diploma in Geosciences (grade 1.6)

Diploma thesis: 3D-subsurface modelling (GOCAD) of Pleistocene strata in the southern salt rim syncline of Schöningen

1997 - 2004 Winckelmann-Gymnasium Stendal, **A level (grade 1.9)**

1995 - 1997 Johann-Friedrich-Danneil-Gymnasium Kalbe/Milde

List of publications

Publications in peer-reviewed journals

- Steinmetz, D.**, Winsemann, J., Ullmann, A., Siemon, B., Brandes, C., Menzel, P., Götze, H.-J., Meyer, U. & Wiederhold, H. (2015): Towards an improved geological interpretation of airborne electromagnetic data: a case study from the Pleistocene Cuxhaven tunnel valley and its Neogene host sediments (northern Germany). *Netherlands Journal of Geosciences*.
- Götze, H.-J., Afanasjew, M., Alvers, M., Barrio-Alvers, L., Börner, R.-U., Brandes, C., Eröss, R., Menzel, P., Meyer, U., Scheunert, M., Siemon, B., Spitzer, K., **Steinmetz, D.**, Stoll, J., Sudha, Tezkan, B., Ullmann, A. & Winsemann, J. (2014): Towards an integrative inversion and interpretation of airborne and terrestrial data. In: M. Weber & U. Münch (Eds.): Tomography of the Earth's Crust: From Geophysical Sounding to Real-Time Monitoring. *GEOTECHNOLOGIEN Science Report No. 21: p. 21-42. Springer*.
- Lang, J., Winsemann, J., **Steinmetz, D.**, Pollok, L., Polom, U., Böhner, U., Serangeli, J., Brandes, C., Hampel, A., Winghart, S. (2012): The Pleistocene of Schöningen (Germany): a complex tunnel valley-fill revealed from 3D subsurface modelling (GOCAD) and shear-wave seismics. *Quaternary Science Reviews 39: 86-105. doi: 10.1016/j.quascirev.2012.02.009*.

Conference contributions (Abstracts)

- Steinmetz, D.**, Winsemann, J., Ullmann, A., Siemon, B., Brandes, C., Menzel, P., Götze, H.-J., Meyer, U. & Wiederhold, H. (2013): The integration of HEM, SkyTEM, borehole and seismic data: an efficient tool for sedimentary basin analysis. *Oral Presentation, Sedimentary Basins Jena 2013, "Research Modelling Exploration", Jena, Germany*.
- Lang, J., Winsemann, J., **Steinmetz, D.**, Polom, U., Pollok, L., Böhner, U., Serangeli, J., Brandes, C., Hampel, A. & Winghart, S. (2013): Depositional architecture of a complex Middle Pleistocene tunnel valley fill, Schöningen, Germany. *30th IAS Meeting of Sedimentology, Manchester, Uk*.
- Steinmetz, D.**, Winsemann, J., Ullmann, A., Siemon, B., Brandes, C., Meyer, U. & Wiederhold, H. (2012): Realistic 3D subsurface models - A new approach by integrating HEM, borehole and seismic datasets. *Poster Presentation, DGG Leipzig, Leipzig, Germany*.
- Steinmetz, D.**, Winsemann, J., Menzel, P., Ullmann, A., Siemon, B., Brandes, C., Götze, H.-J., Meyer, U. & Wiederhold, H. (2012): Enhancing the quality of 3D subsurface models by integrating geophysical datasets. *Oral Presentation, GeoHannover, Hannover, Germany*.

List of publications

- Lang, J., Winsemann, J., **Steinmetz, D.**, Polom, U., Pollok, L., Böhner, U., Serangeli, J., Brandes, C., Hampel, A. & Winghart, S. (2012): Anatomy of a complex tunnel valley fill revealed from 3D subsurface modelling and shear wave seismics: the Pleistocene of Schöningen, Germany. *GeoHannover, Hannover, Germany.*
- Lang, J., Winsemann, J., **Steinmetz, D.**, Polom, U., Pollok, L., Böhner, U., Serangeli, J., Brandes, C., Hampel, A. & Winghart, S. (2012): Insights into a complex Middle Pleistocene tunnel valley fill, Schöningen, Germany. *GV & Sediment Meeting, Hamburg, Germany.*
- Lang, J., Winsemann, J., **Steinmetz, D.**, Polom, U., Pollok, L., Böhner, U., Serangeli, J., Brandes, C., Hampel, A. & Winghart, S. (2012): Sequence stratigraphic correlation of the Paleolithic sites of Schöningen (Germany). *Umwelt-Mensch- Georisiken im Quartär: 35. Hauptversammlung der deutschen Quartärvereinigung (DEUQUA), Bayreuth.*
- Lang, J., Winsemann, J., **Steinmetz, D.**, Polom, U., Pollok, L., Böhner, U., Serangeli, J., Brandes, C., Hampel, A., Conard, N. & Winghart, S. (2012): The famous findings of Schöningen, Germany: a new geological model for the embedding and preservation of paleolithic artefacts. *Hugo Obermeier-Gesellschaft, 54th Annual Meeting, Toulouse, France.*
- Lang, J., **Steinmetz, D.**, Pollok, L., Brandes, C., Hampel, A., Polom, U., Winghart, S. & Winsemann, J. (2011): The Middle Pleistocene succession of Schöningen, Germany: A complex tunnel valley fill inferred from 3D subsurface modeling. *XVIII. INQUA, Bern, Switzerland.*
- Lang, J., **Steinmetz, D.**, Pollok, L., Böhner, U., Brandes, C., Hampel, A., Polom, U., Winghart, S., & Winsemann, J. (2011): Integrating modern geological tools and archaeology: a case study from the famous Middle Pleistocene succession of Schöningen, Germany. *XVIII. INQUA, Bern, Switzerland.*
- Lang, J., **Steinmetz, D.**, Brandes, C., Polom, U. & Winsemann, J. (2010): A depositional model for the Middle Pleistocene succession of Schöningen. NW Germany: facies analysis, seismic stratigraphy and 3D subsurface modeling (GOCAD). *Ice, Water, Humans: 35. Hauptversammlung der deutschen Quartärvereinigung (DEUQUA), Greifswald, Germany.*